

**MODELING AND SIMULATION OF X-RAYS
RADIOTHERAPY**

**X-IŞINLARI RADYOTERAPİSİNİN MODELLENMESİ VE
BENZEŞİMİ**

GÜRDAL GÖKERİ

Submitted to
HACETTEPE UNIVERSITY
THE INSTITUTE FOR GRADUATE STUDIES
IN SCIENCE AND ENGINEERING
in partial fulfillment of the requirements for the degree of
DOCTORATE OF PHILOSOPHY
in
NUCLEAR ENGINEERING

2012

**MODELING AND SIMULATION OF X-RAYS
RADIOTHERAPY**

**X-IŞINLARI RADYOTERAPİSİNİN MODELLENMESİ VE
BENZEŞİMİ**

GÜRDAL GÖKERİ

Submitted to
HACETTEPE UNIVERSITY
THE INSTITUTE FOR GRADUATE STUDIES
IN SCIENCE AND ENGINEERING
in partial fulfillment of the requirements for the degree of
DOCTORATE OF PHILOSOPHY
in
NUCLEAR ENGINEERING

2012

To the Directory of the Institute for Graduate Studies in Science and Engineering,
This study has been accepted as a thesis for the degree of DOCTORATE OF
PHILOSOPHY in NUCLEAR ENGINEERING by our Examining Committee.

Head :.....
Prof. Dr. Okan Zabunođlu

Advisor :.....
Prof. Dr. Mehmet Tombakođlu

Co-advisor :.....
Dođ. Dr. Cemil Kocar

Member :.....
Prof. Dr. Őlfet Atav

Member :.....
Dođ. Dr. Ayhan Yilmazer

This is to certify that the Board of Directors of the Institute for Graduate Studies in
Science and Engineering has approved this thesis on ... /... /2012

Prof. Dr. Fatma SEVIN DŐZ
Director of the Institute for Graduate
Studies in Science and Engineering

To my beloved daughter, AĐLA

MODELING AND SIMULATION OF X-RAYS RADIOTHERAPY

Gürdal Gökeri

ABSTRACT

In this thesis, various concepts for Microbeam Radiation Therapy (MRT) technique were simulated and dosimetric calculations were performed with the Monte Carlo technique. In the first part, the dosimetric Monte Carlo calculations in the literature, performed with other codes were done with MCNPX to evaluate the suitability of the code for micrometric dosimetry at low X-ray energies. The calculated dose distributions were consistent with the ones that are given in the literature. In the second part, dose distribution calculations for bidirectional interlaced microbeam radiation therapy (BIMRT) were performed with realistic and homogenized head phantom models. The effect of the realistic phantom's structure on dose distribution was evaluated. The parallel pattern of the microbeam arrays was preserved through the head phantom. As the dimensions of the target volume were increased, the valley doses increased with the number of microbeams. Simulations were performed for cases with and without Au contrast agent deposited in the target region and the surrounding tissue. The usage of the contrast agent provided a substantial increase in target dose. Short dose falloff widths at the edges of the targets were preserved for all cases. In the third part, the usage of a linear accelerator (linac) as the radiation source for the stereotactic MRT technique was evaluated. Unidirectional single beams and beam arrays were modeled in a cylindrical water phantom to observe the effects of X-ray energies, beam heights, beam thicknesses and beam intervals on dose distributions. Two orthogonally interlaced beam arrays were modeled in a detailed head phantom. Calculated dose distributions were compared with the ones calculated for the BIMRT. Five orthogonally interlaced beam array pairs were modeled in a mathematical head phantom. It was concluded that the advantages of the MRT technique would not be preserved with the usage of linac as the X-ray source.

Keywords: Microbeam therapy, Monte Carlo, MCNP, Au Contrast Agent, Zubal

Advisor: Prof.Dr. Mehmet TOMBAKOĞLU, Hacettepe University, Department of Nuclear Engineering

Co-advisor: Assoc. Prof. Dr. Cemil KOCAR, Hacettepe University, Department of Nuclear Engineering

X-IŞINLARI RADYOTERAPİSİNİN MODELLENMESİ VE BENZEŞİMİ

Gürdal Gökeri

ÖZ

Bu tezde Mikrodemet Radyasyon Terapisi (MRT) tekniğindeki farklı konseptlerin benzeşimleri yapılmış ve dozimetrik hesaplamalar Monte Carlo tekniği ile yapılmıştır. İlk bölümde düşük X-ışını enerjilerinde mikrometrik dozimetri için MCNPX kodunun uygunluğunu değerlendirmek üzere literatürde geçen diğer dozimetrik Monte Carlo hesaplamaları MCNPX koduyla yapılmıştır. Hesaplanan doz dağılımlarının literatürde verilenlerle uyum içinde olduğu görülmüştür. İkinci bölümde iç içe geçmiş iki yönlü mikrodemet terapisi (BIMRT) için doz dağılımı hesapları gerçekçi ve homojenize edilmiş kafa fantomlarıyla gerçekleştirilmiştir. Mikrodemet dizilerinin paralel şekli kafa fantomu boyunca korunmuştur. Hedef hacminin boyutları arttıkça vadi dozları mikrodemetlerin sayısı ile beraber artmıştır. Altın kontrast ajanının hedef bölge ve etrafındaki dokularda birikim gösterdiği durumlar için benzeşimler gerçekleştirilmiştir. Kontrast ajanının kullanımı hedef dozunda önemli miktarda artış sağlamıştır. Hedeflerin yanındaki kısa doz düşüşü mesafeleri bütün durumlarda korunmuştur. Üçüncü bölümde bir lineer hızlandırıcının stereotaktik MRT için kaynak olarak kullanımı değerlendirilmiştir. X-ışını enerjilerinin, demet yüksekliklerinin, demet genişliklerinin ve demet aralıklarının doz dağılımları üzerindeki etkisinin gözlenmesi açısından tek yönlü tek demetler ve demet dizileri silindirik su fantomu içinde modellenmiştir. İki dik olarak iç içe geçirilmiş demet dizisi detaylı kafa fantomu içinde modellenmiştir. Hesaplanan doz dağılımları BIMRT için hesaplanmış olanlarla karşılaştırılmıştır. Beş adet dik olarak iç içe geçirilmiş demet dizisi çifti bir matematiksel fantom içinde modellenmiştir. Linac'ın X-ışını kaynağı olarak kullanımıyla MRT tekniğinin avantajlarının korunamayacağı sonucuna varılmıştır.

Anahtar Kelimeler: Microdemet terapisi, Monte Carlo, MCNP, Au Kontrast Ajanı, Zubal

Danışman: Prof.Dr. Mehmet TOMBAKOĞLU, Hacettepe Üniversitesi, Nükleer Enerji Mühendisliği Bölümü

Eş danışman: Doç. Dr. Cemil KOCAR, Hacettepe Üniversitesi, Nükleer Enerji Mühendisliği Bölümü

ACKNOWLEDGEMENTS

I would like to thank my advisor Prof. Dr. Mehmet Tombakođlu and my co-advisor Assoc. Prof. Dr. Cemil KOCAR for their guidance and trust. I would like to thank the committee members for their valuable comments. I would also like to thank Osman řahin řelikten for providing computational capacity that is necessary for the calculations.

Finally, I would like to thank my wife Gökçe, my parents and my friends for their support.

Gürdal Gökeri
Hacettepe University
Department of Nuclear Engineering
October 2012

TABLE OF CONTENTS

	<u>Page</u>
1. INTRODUCTION	1
1.1. X-ray Sources.....	4
1.1.1. Synchrotrons	4
1.1.2. X-ray tubes.....	6
1.1.3. Linear accelerators.....	7
1.2. Photon Interaction Mechanisms.....	10
1.3. Electron Interaction Mechanisms.....	16
1.4. Thesis Objectives	23
1.5. Outline of the Thesis	23
2. EVALUATION OF THE SUITABILITY OF THE MONTE CARLO CODE MCNPX FOR MICROMETRIC DOSE DISTRIBUTION CALCULATIONS AT LOW X- RAY ENERGIES.....	25
2.1. Depth – Dose Distributions	26
2.2. Lateral Dose Distribution around a Cylindrical Pencil Microbeam.....	26
2.3. Angular Distributions and Spectrums of the Secondary Particles	27
2.4. Effect of Microbeam Thickness on Dose Distributions	30
2.5. Depth Dose Distributions for Microbeam Arrays.....	30
2.6. Conclusion	32
3. MONTE CARLO SIMULATION OF MICROBEAM RADIATION THERAPY WITH AN INTERLACED IRRADIATION GEOMETRY AND AN AU CONTRAST AGENT IN A REALISTIC HEAD PHANTOM	33
3.1. Modified Zubal Head Phantom and Homogenized Phantom	33
3.1. The Irradiation Geometry and Sampled X-Ray Energies.....	36
3.3. Au Contrast Agent Deposited in Target and Surrounding Tissue	36
3.4. The Monte Carlo Simulations	37
3.5. Results	39
3.5.1. Two-dimensional qualitative dose distribution inside the realistic phantom.....	39
3.5.2. Lateral dose distributions inside and around the target regions.....	40
3.5.3. Comparison of homogenized and realistic head phantoms	40
3.5.4. Effect of the number of microbeams: Comparison of 15- and 5-beam arrays...	43
3.5.5. Effect of Au contrast agent	46
3.6. Discussion.....	49
4. EVALUATION OF THE USAGE OF A LINEAR ACCELERATOR AS THE X- RAY SOURCE FOR MICROBEAM RADIATION THERAPY	52
4.1. The radiation Source and The Sampled X-ray Energies	52
4.2. Dose Calculations for Single Unidirectional Beams in Cylindrical Water Phantom	54
4.3. Dose Calculations for Unidirectional Beam Arrays inside Cylindrical Water Phantom.....	55
4.4. Dose Calculations for Interlaced Orthogonal Beam Arrays inside Detailed Human Head Phantom.....	56
4.5. Dose Calculations for Five Orthogonally Interlaced Beam Array Pairs in a Mathematical Head Phantom.....	57
4.6. Results	60
4.6.1. Dependence of dose distributions on beam energies.....	60
4.6.2. Dependence of dose distributions on beam heights	61
4.6.3. Dependence of dose distributions on beam thicknesses	63

4.6.4. Dependence of dose distributions on center-to-center distances for planar and square pencil beam arrays.....	64
4.6.5. Two-dimensional dose distributions through the realistic head phantom and in the target region for orthogonally interlaced beam arrays.....	65
4.6.6. Depth – dose and depth – PVDR distributions through the realistic head phantom for orthogonally interlaced beam arrays	67
4.6.7. Two-dimensional dose distribution in and around the target region for five orthogonally interlaced beam array pairs	69
4.6.8. Depth – dose and depth – PVDR distributions through the mathematical head phantom for five orthogonally interlaced beam array pairs	69
5. CONCLUSION.....	73

LIST OF FIGURES

	<u>Page</u>
Figure 1.1. An illustration of the linac, the booster synchrotron and the storage ring of ESRF (www.esrf.eu, 2012).....	4
Figure 1.2. An illustration of an insertion device (www.esrf.eu, 2012).....	5
Figure 1.3. A schematic diagram of an X-ray tube (Mayles et al., 2007).....	6
Figure 1.4. Schematic diagram of a linear accelerator used in X-ray mode (Mayles et al., 2007).....	8
Figure 1.5. Diagram of the dual energy treatment head of an Elekta SL series accelerator (Mayles et al., 2007).....	9
Figure 1.6. The effect of flattening filter (beam without (a) and with (b) flattening filter (Mayles et al., 2007).....	10
Figure 1.7. Cross-sectional views of multi-leaf collimators (Mayles et al., 2007) ..	10
Figure 1.8. Scattering angles and solid angle for photon scattering (Mayles et al., 2007).....	11
Figure 1.9. Photoelectric absorption (Mayles et al., 2007).....	12
Figure 1.10. The constant n in Equation 1.5 as a function of photon energy (Evans, 1955).....	13
Figure 1.11. Compton scattering (Mayles et al., 2007).....	14
Figure 1.12. Representation of the track of a charged particle in matter (ICRU, 1970).....	17
Figure 1.13. Interaction between a fast primary charged particle and a bound electron (Nahum, 1985).....	18
Figure 1.14. Energy broadening because of energy-loss straggling after the passage of a monoenergetic electron beam (energy E_0) through a thin absorber. (Nahum, 1985.).....	21
Figure 1.15. Calculated tracks (projected into the X–Y plane of the figure) of ten 740-keV electrons entering a water slab normally from the left at the origin (Turner, 2007).....	22
Figure 2.1. ID17 beamline spectrum that is used for MRT.....	25
Figure 2.2. Normalized depth – dose distributions obtained for different tally bin geometries.....	26
Figure 2.3. Lateral dose distribution beside a 25 μm -diameter cylindrical pencil beam between 7 – 8 cm depths.....	27
Figure 2.4. Secondary electron spectrums calculated at the planar beam boundaries.....	28
Figure 2.5. Angular distributions of secondary electrons calculated at the planar beam boundaries.....	29
Figure 2.6. Secondary photon spectrums calculated at the planar beam boundaries.....	29
Figure 2.7. Angular distributions of secondary photons calculated at the planar beam boundaries.....	30
Figure 2.8. Lateral dose distributions for beam thicknesses of 25 μm , 50 μm and 75 μm	31
Figure 2.9. Depth – peak dose and depth – valley dose distributions for 100- and 200- μm -ctc distances.....	32
Figure 2.10. Depth – PVDR distributions for 100- and 200- μm -ctc distances.....	32

Figure 3.1 3-D view of the modified Zubal head Phantom (lower jaw is not given)	35
Figure 3.2 2-D slice view of modified Zubal head Phantom (densities in g / cm ³).	35
Figure 3.3. Irradiation geometry	36
Figure 3.4. Two-dimensional qualitative dose distribution for interlaced irradiation geometry	39
Figure 3.5. Lateral dose distributions averaged through the target region for all cases	40
Figure 3.6. Depth–in-beam dose distributions for cases I and II	41
Figure 3.7. Depth – valley dose distributions for cases I and II	42
Figure 3.8. Depth – PVDR distributions for cases I and II	43
Figure 3.9. Depth – in-beam dose distributions for cases II and III	44
Figure 3.10. Depth – valley-dose distributions for cases II and III	45
Figure 3.11. Depth – PVDR distributions for cases II and III	45
Figure 3.12. Lateral dose distribution at the edges of the targets for cases II and III	46
Figure 3.13. Depth–in-beam dose distributions for cases II, IV and V	47
Figure 3.14. Depth–valley dose distributions for cases II, IV and V	48
Figure 3.15. Depth–PVDR distributions for cases II, IV and V	48
Figure 3.16. Lateral dose distribution at the edges of the targets for cases II, IV and V	49
Figure 4.1. Spectrum of linac-generated X-rays	53
Figure 4.2. Angular distribution of linac-generated X-rays	54
Figure 4.3. Irradiation geometry for two orthogonally interlaced beam array pairs	57
Figure 4.4. Irradiation geometry for five orthogonally interlaced beam array pairs	58
Figure 4.5. Patterns of A- and B-type beam arrays	59
Figure 4.6. Depth – in-beam dose distributions for different beam energies (beam thickness = 0.5 mm, square pencil beam)	60
Figure 4.7. Dose distributions lateral to single beams for different beam energies (beam thickness = 0.5 mm, square pencil beam)	61
Figure 4.8. Depth – in-beam dose distributions for different beam heights (beam thickness = 0.5 mm, linac spectrum)	62
Figure 4.9. Dose distributions lateral to single beams between 3.5 – 5.5 cm depths for different beam heights (beam thickness = 0.5 mm, linac spectrum)	62
Figure 4.10. Depth – in-beam dose distributions for different beam thicknesses (beam height = 20 mm, linac spectrum)	63
Figure 4.11. Dose distributions lateral to single beams between 3.5 – 5.5 cm depths for different beam thicknesses (beam height = 20 mm, linac spectrum)	64
Figure 4.12. Dose distributions lateral to center beams between 3.5 – 5.5 cm depths for different beam ctc distances, planar and square beams (linac spectrum)	65
Figure 4.13. Two-dimensional dose distribution through the detailed head phantom for irradiation with two orthogonally interlaced beam arrays	66
Figure 4.14. Two-dimensional dose distribution in the target area for irradiation with two orthogonally interlaced beam arrays	66
Figure 4.15. Depth – in-beam and valley dose distributions for two orthogonally interlaced linac and synchrotron-generated beam arrays	67
Figure 4.16. Depth – PVDR distributions for two orthogonally interlaced linac and synchrotron-generated beam arrays	68

Figure 4.17. Two-dimensional dose distribution in and around the target region for irradiation with five orthogonally interlaced beam array pairs70
Figure 4.18. Depth – in-beam and depth – valley dose distributions in the arrays 21A and 22A for irradiation with five orthogonally interlaced beam array pairs70
Figure 4.19. Depth – PVDR distributions in the arrays 21A and 22A for irradiation with five orthogonally interlaced beam array pairs.....71

LIST OF TABLES

	<u>Page</u>
Table 3.1 The simulated cases.....	38
Table 3.2. The ratios of skin entrance, maximum skull bone and maximum brain in-beam doses to target exit in-beam doses for case I and II	42
Table 3.3. The ratios of skin entrance, maximum skull bone and maximum brain in-beam doses to target exit in-beam doses for cases II and III	44
Table 3.4. The ratios of skin entrance, maximum skull bone and maximum brain in-beam doses to target exit in-beam doses for cases II, IV and V.....	47
Table 4.1. The cases for which depth – in-beam dose distributions and dose fall-offs are calculated	55
Table 4.2. Dimensions of the tallies used for calculating depth – in-beam dose distributions and dose fall-offs around the unidirectional beams for cases I – VIII	55
Table 4.3. The cases for which dose distributions lateral to the center beams in the arrays are analyzed.....	56
Table 4.4. Positioning of linac for irradiation with five orthogonally beam array pairs	59
Table 4.5. The ratios of skin entrance, maximum skull bone and maximum brain in-beam doses to target exit in-beam doses for interlaced linac-generated and synchrotron-generated beam arrays	69

LIST OF ACRONYMS

AuNP:	Gold nanoparticle
BIMRT:	Bidirectional Interlaced Microbeam Radiation Therapy
csda:	Continuous-Slowing-Down-Approximation
ctc:	Center to Center
ESRF:	European Synchrotron Radiation Facility
HVL:	Half Value Layer
Linac:	Linear Accelerator
MC:	Monte Carlo
MRT:	Microbeam Radiation Therapy
SSD:	Source-to-Skin Distance

1. INTRODUCTION

Microbeam Radiation Therapy (MRT) (Slatkin et al., 1992; Laissue et al., 1998) is a technique which uses the principle that the normal tissue can tolerate high radiation doses in small volumes (Curtis, 1967). MRT is carried out using arrays of highly intense synchrotron-wiggler-generated X-rays with 107 – 120 keV mean energy. The typical beam widths are 25 – 50 μm and beam intervals are 100, 200 or 400 μm (Laissue et al., 1998; Spiga et al., 2006; 2007; Prezado et al., 2009a). During the last two decades, potential applications of MRT have been studied experimentally at National Synchrotron Light Source at Upton, New York, USA and at the European Synchrotron Radiation Facility (ESRF) in Grenoble, France.

The main attribute of the method is its remarkable sparing effect in healthy tissue, including the central nervous system (Slatkin et al., 1995; Laissue et al., 1999; 2001; Dilmanian et al., 2001; 2002; 2007; Regnard et al., 2008a; Serduc et al., 2008a). The resistance of healthy tissue to radiation damage from beams of ionizing radiation with thicknesses in the order of micrometers was first observed by Straile and Chase (1963). MRT has the potential to be used for treating infantile brain tumours when other kinds of radiotherapy would be highly toxic to the developing normal brain (Laissue et al., 2007).

The reason for the tolerance of healthy tissue to high radiation doses in MRT has not been fully understood. It is assumed that the microvasculature in the paths of the beams is regenerated from the angiogenic cells surviving in the regions between the paths of the beams (Slatkin et al., 1995; Serduc et al., 2006; 2008a; 2008b). This is said to be not observed in tumour tissue and microvessels of the tumour are damaged which can lead to the loss of blood perfusion and tissue necrosis (Dilmanian, 2005). However Crosbie et al. (2010) found no qualitative evidence of microvascular effect in MRT-irradiated tumours. They claim that normal tissue, unlike the tumour, was able to mount an effective repair response to remove the damaged cells. The reduction in tumour cell proliferation was explained with cell communication responses which are promoted by rapid intratumoural migration of maximally and minimally irradiated cells.

The dose administered in the beams' paths is named as "peak dose" and the dose deposited between two adjacent beams is named as "valley dose". The normal

tissue tolerance to MRT is believed to depend mostly on the valley dose (Dilmanian et al., 2002; Martinez-Rovira et al., 2010). Peak-to-valley dose ratio (PVDR) is a relative quantity which is necessary to have the information on both peak and valley doses.

In recent studies it was observed that the rat central nervous system tolerated microbeams as thick as 0.68 mm. An unsegmented radiation field could be produced by interlacing two orthogonal 'thick' microbeam arrays, which are also named as minibeam arrays (Prezado et al., 2009b; 2009c), aimed at the target (Dilmanian et al., 2006; 2008; Anschel et al., 2007; Dilmanian, 2007; Gokeri et al., 2010). In Dilmanian et al.'s experimental study (2006) spinal cords of four rats were exposed transaxially to four 400 Gy, 0.68-mm-thick microbeams spaced 4 mm apart. Brains of four rats were irradiated with large, 170 Gy arrays of such beams spaced 1.36 mm apart. Three of the rats in the first group and all four rats in the second group showed no paralysis or behavioural changes.

For 'thick' interlaced microbeam arrays, Monte Carlo (MC) calculations indicated 80–20% dose falloff width of 30 μm at the edge of the target, which is much less than the 2–5 mm value typical for conventional radiotherapy (Dilmanian et al., 2006; 2008; Gokeri et al., 2010).

In the interlaced MRT technique, a radiation contrast agent with high atomic number (Z), such as iodine, platinum, gadolinium or gold may be administered to the target tissue for preferential x-ray absorption (Dilmanian et al., 2006; Dilmanian 2007). The contrast agent enhances the in-beam dose (dose administered in the beams' paths, peak dose) of the microbeams substantially within the target tissue. The dose enhancement is derived from the enhanced photoelectric and Compton scattering cross-sections. The Compton scattering cross-section varies linearly with Z ; however, the photoelectric cross-section scales as Z^4 in the considered energy interval (Evans 1955).

Dilmanian (2007) stated that the administration of heavy elements to the tumour tissue for large gain in therapeutic efficacy could be best implemented with the use of gold nanoparticles (AuNP) (Hainfeld et al., 2004; 2006; 2010). Radiation doses to cells near AuNPs preferentially increase from photoelectrons and secondary

electron cascades produced by gold atoms interacting with x-rays (Cho, 2005; Roeske et al., 2007; McMahon et al., 2008). Gold is known to be chemically inert, and AuNPs have been found to be safe in previous animal studies (Hainfeld et al., 2004; James et al., 2007).

In the Hainfeld et al.'s (2004; 2010) studies on mice with AuNPs, the nanoparticle size was chosen as 1.9 nm to take advantage of the 'leaky' vasculature of tumours (Dvorak, 1990). Leaky vasculature is due to the smaller dimensions of nanoparticles (e.g., 1–100 nm) than the typical cutoff size of the pores (e.g., up to 400 nm) in the tumour vasculature (Unezaki et al., 1996).

In a study performed for unidirectional thin microbeams (Regnard et al., 2008b), Gd-DTPA was tested as a contrast agent. 9L tumour-bearing rats were laterally irradiated with 51 microbeams (25 µm beam width, 200 µm beam interval and 625 Gy skin dose). It was stated that the combination between an intracranial injection of gadolinium and MRT led to an increase of the median survival time by a factor of 1.5 if compared to the MRT irradiation alone.

A MC study was performed by Prezado et al. (2009a) again for unidirectional 'thin' microbeam arrays in a mathematical anthropomorphic phantom. In that study, dose enhancement factors (the ratio of the average radiation dose absorbed by the tumour when it is loaded with contrast media to the dose absorbed without contrast media) were assessed for different iodine, gadolinium and gold concentrations. It was further stated that Gd and Au showed a clear superiority with respect to I for dose enhancement.

It is claimed that thicker microbeams may allow the use of higher-energy photons (Dilmanian, 2007; 2009; 2010; Dilmanian et al., 2006; 2008), possibly from a special X-ray tube (orthovoltage X-ray tube). An unsegmented dose region is claimed to be formed in the target when it is irradiated with five orthogonally interlaced beam array pairs and the technique is named as stereotactic micro beam therapy (Dilmanian, 2009; 2010). The usage of orthovoltage X-ray tube as a radiation source has been evaluated at Brookhaven National Laboratory, New York, USA (F. A. Dilmanian, 2010, written communication).

1.1. X-ray Sources

1.1.1. Synchrotrons

Synchrotron light is produced when high-energy electrons, circulating in a storage ring, are deviated by magnetic fields. In this study photon energies for synchrotron-generated X-rays were sampled from the spectrum calculated (Siegbahn et al., 2005) at the ID17 beamline of European Synchrotron Light Source Facility (ESRF) at Grenoble, France (www.esrf.eu, 2012).

Electrons emitted by an electron gun, packed in bunches, are accelerated by a pulsed electric field in a linear accelerator (linac). Then they pass to a 300-meter-long circular accelerator (booster synchrotron) where they are accelerated to energy of 6 GeV. The booster synchrotron contains radiofrequency cavities and bending magnets which hold the electrons in a circular orbit. The strength of the magnetic field must be increased and synchronized to the increasing energy of the electrons and that is why the accelerator is called as synchrotron.

The accelerated electrons are then transferred to a vacuum chamber, the storage ring which has a circumference of 844 meters. The electrons travel in the storage ring for many hours with a current of 200 mA. An illustration of the linac, the booster synchrotron and the storage ring of ESRF is given in Figure 1.1.

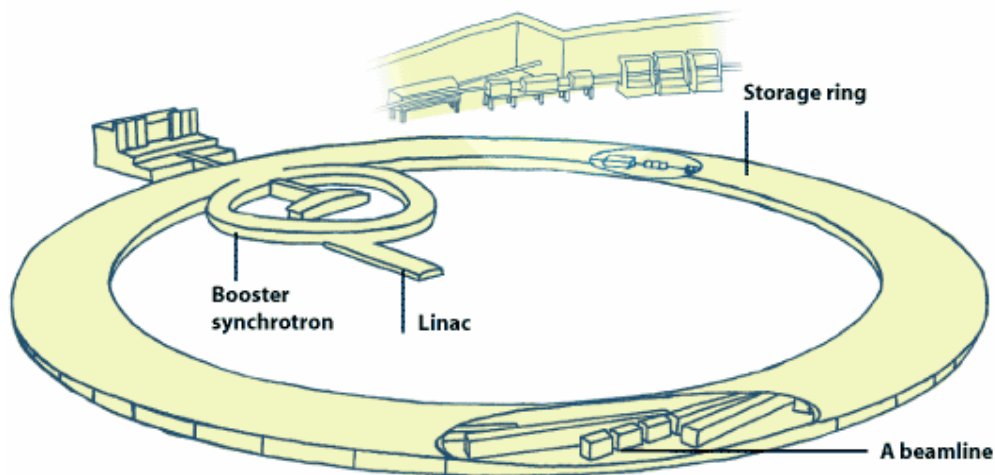


Figure 1.1. An illustration of the linac, the booster synchrotron and the storage ring of ESRF (www.esrf.eu, 2012)

The storage ring is not a perfect circle but consists of 32 nodes where the bending magnets are and 32 straight regions where the insertion devices are located. There are 64 bending magnets in the storage ring. There are 42 experimental stations (beamlines) around the storage ring where X-rays are extracted for experimental purposes. The beamlines start at the bending magnets and insertion devices. ID17 beam line is dedicated to biomedical imaging, radiation biology and therapy.

The bending magnets force the electrons into a curved trajectory. As the electrons are deviated, X-rays which covers a wide and continuous spectrum are emitted due to acceleration. The insertion devices, located at the straight section of the storage ring, are structures with alternating magnetic poles which force the electrons to follow an undulating or wavy trajectory, and this results in emission of X-rays. The insertion devices, depicted in Figure 1.2, can produce much larger X-ray flux than the bending magnets do. The main difference between the two types of insertion devices, wigglers and undulators, is electron oscillations in a wiggler are relatively large which results in incoherently addition of photons. However, in an undulator photons generated with the same phase are added coherently so that the highest brilliance at a desired energy may be obtained. The spectrums of X-rays that are produced by a wiggler and a bending magnet are the same, but the intensities of wiggler-generated X-rays are much higher. The ID17 beamline uses a wiggler insertion device.

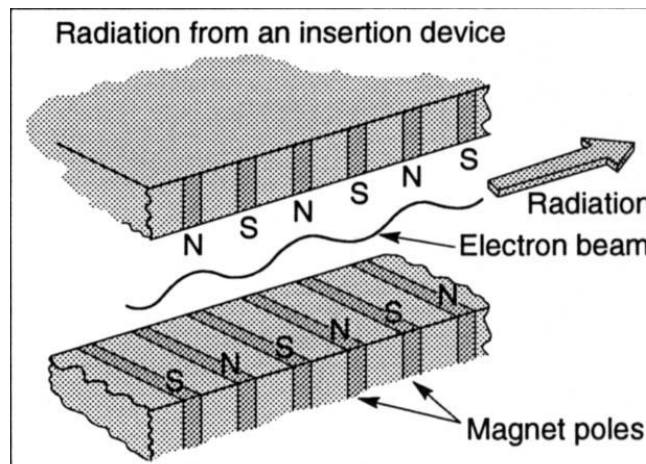


Figure 1.2. An illustration of an insertion device (www.esrf.eu, 2012)

1.1.2. X-ray tubes

The usage of kilovoltage X-rays in radiotherapy has gradually diminished over the years because of the introduction of high energy photon sources. However they still provide an option in the range of treatments available.

The X-ray tube consists of a cathode, an anode and an evacuated tube. The cathode is a tungsten filament and emits electrons via the process of thermionic emission when heated by passing a current through it. The emitted electrons are accelerated through a potential difference and strike onto the anode which consists of a tungsten target embedded within a block of copper. Most of the electrons' energy is deposited as heat in the target, however a small percentage (ranging from 0.5% at 60 kVp to 1% at 200 kVp) is converted to x-rays (Meredith et al., 1977). A schematic diagram of an X-ray tube is given in Figure 1.3.

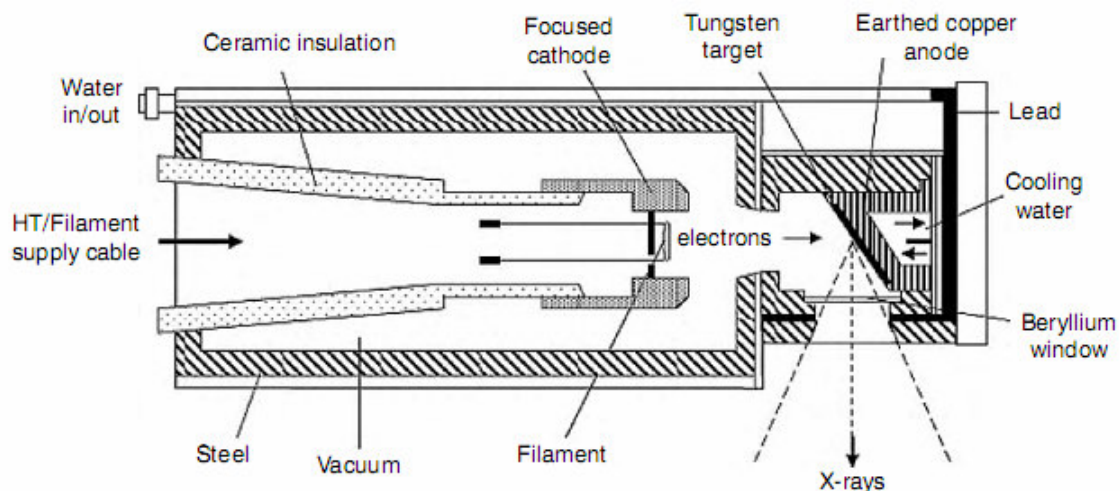


Figure 1.3. A schematic diagram of an X-ray tube (Mayles et al., 2007)

The energy (or quality) of the X-ray beam is dependent on the potential difference applied. However the spectrum can be adjusted by placing metallic filters in the beam's path. Thus beams of different penetrative qualities can be produced with the same potential difference. For this reason, the beam quality is defined in terms of the thickness of a material (usually aluminum or copper) that will reduce the beam intensity to half of its initial value. This thickness is called the half value layer (HVL).

Metal filters are used for preferential absorption of the low-energy photons in the X-ray spectrum depending on the intended depth of treatment. The mean energy of the spectrum increases or hardens in the filter, since the lower-energy photons are attenuated more than those at higher energies. Thus the dose incurred in superficial tissue, to administer the desired dose in deeper regions, is decreased.

Kilovoltage range covering X-ray beams generated between 10 kV 400 kV is subdivided into categories according to increasing beam penetration and this reflects the types of treatment that each range is suitable for. The ranges are given as (Mayles et al., 2007):

- Grenz rays (10 kV to 20 kV, 0.02 mm to 0.15 mm Al HVL) lie between the hardest ultraviolet rays and X-rays. This range is rarely used in radiotherapy.
- Short distance or contact therapy (10 kV to 60 kV, 0.02 mm to 3.3 mm Al HVL) provides a useful treatment depth up to several millimeters.
- Superficial therapy (50 kV to 150 kV, 1 mm to 8 mm Al HVL) which has probably been least affected by the introduction of high energy linear accelerators since the range is used in the treatment of superficial lesions and in many other cases. The range provides a useful treatment depth of around 5 mm by 90 % of the surface dose.
- Orthovoltage therapy or deep therapy (150 kV to 400 kV) is generally applied with generating potentials from 160 kVp to 300 kVp corresponding to 0.5 mm to 4 mm Cu HVL for typical filtrations. The range provides treatment depths of 1 cm to 2 cm by 90 % of the surface dose. The usual source-to-skin distance (SSD) is 50 cm.

1.1.3. Linear accelerators

Megavoltage X-ray beams which are generated by linear accelerators (linac) are more penetrating than kilovoltage X-rays. Thus less skin dose is incurred to administer desired target dose. The skull bone dose is not enhanced since the principal photon interaction with tissue is through the Compton effect. Thus total interaction cross-section is less depended on the atomic number of the tissue (Mayles et al., 2007).

X-rays are produced in the linacs with bremsstrahlung radiation due to collision of accelerated electrons with a high-atomic-number target as in X-ray tubes. However transformer-based high voltage X-ray generators are not suitable for energies above 300 kV. The linac-generated megavoltage electron beams can be directly used or converted to X-rays for patient treatment.

In linacs, electrons are accelerated with a synchronised radio-frequency electromagnetic field rather than with direct potential. The speed of propagation of the electromagnetic waves is reduced in the accelerating waveguide which consists of a cylindrical tube and contains series of circular baffles. The propagation speed of the microwaves increases and reaches close to the speed of light as the waves propagate inside the tube. Bunches of electrons, which are generated by an electron gun and injected into the waveguide in synchronism with the pulsed microwaves, are accelerated through the tube.

The principal direction of the photon emitted from bremsstrahlung emission due to megavoltage electron beams is in the forward direction. The emerging X-ray beam is coaxial with the accelerating structure in the simplest design. However for energies above 6 MeV, this is impracticable for irradiating the patient due to length of the waveguide. Thus the electron beam is deflected in a magnetic field and bent before collision with the high-atomic-number target. Schematic diagram of a linear accelerator used in X-ray mode for radiotherapy is given in Figure 1.4.

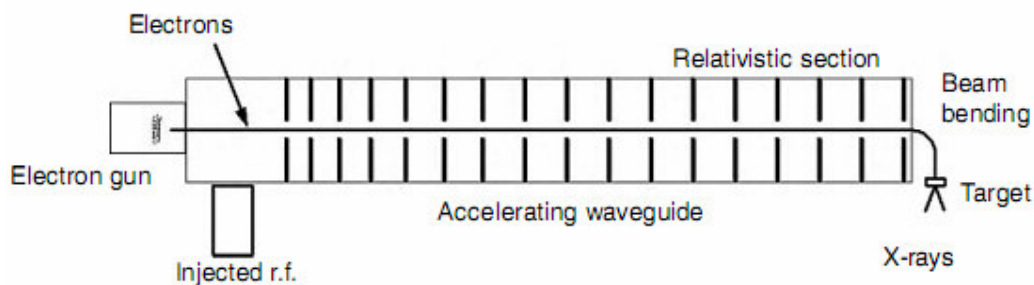


Figure 1.4. Schematic diagram of a linear accelerator used in X-ray mode (Mayles et al., 2007)

The head assembly

An example of the components of the treatment head is given as a diagram in Figure 1.5. A narrow beam of electrons delivered by the accelerating and bending

structure is focused on the X-ray target. The target is made of tungsten or copper-tungsten laminate. The bremsstrahlung emission becomes increasingly directed forward as the electron beam energy is increased. The water cooled target can be moved out of the beam for treatment with the electron beam.

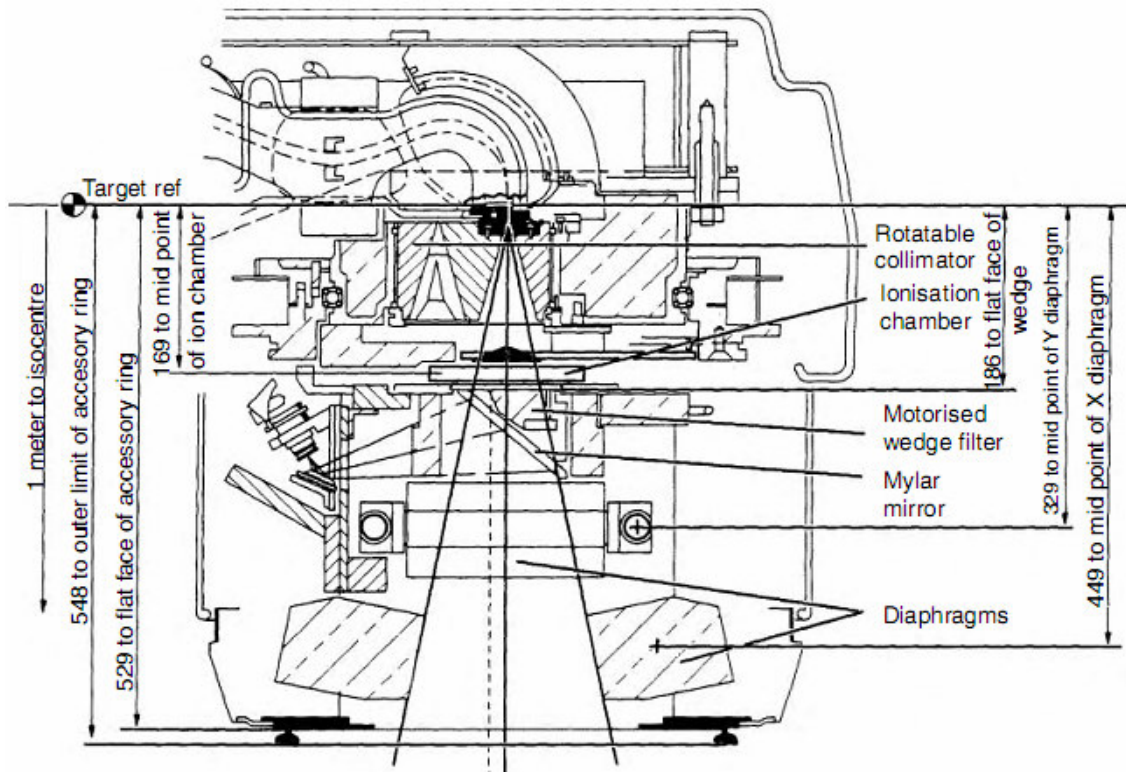


Figure 1.5. Diagram of the dual energy treatment head of an Elekta SL series accelerator (Mayles et al., 2007)

Flattening filter is used for homogenizing photon flux distribution in the beam. The effect of the flattening filter is shown in Figure 1.6.

Accelerators have a circular primary collimator to constrain the beam so that only the required parts of the patients are irradiated. Secondary collimators (also called diaphragms) which are usually made of flat-faced blocks of lead move in arc so that the blocks are aligned with the divergent edge of the radiation field.

The mentioned collimators can only constrain the radiation field to a rectangular shape. Multileaf collimators may be used in order to provide more flexibility and confine the field to the target's shape. These collimators have up to 80 pairs of

leaves that can move independently. Cross-sectional views of some examples are given in Figure 1.7. The leaves in the figure are stepped to avoid leakage.

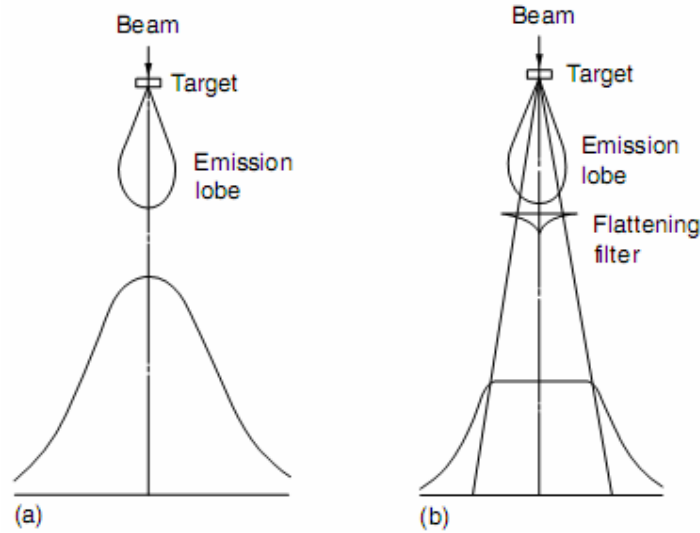


Figure 1.6. The effect of flattening filter (beam without (a) and with (b) flattening filter (Mayles et al., 2007)

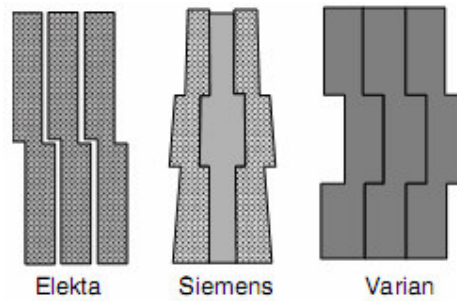


Figure 1.7. Cross-sectional views of multi-leaf collimators (Mayles et al., 2007)

Wedge filters are used when a wedge-shaped intensity profile is required instead of uniform beam intensity. Wedge filters are made of brass, aluminum or lead. The commonly used wedge angles are 15°, 30°, 45° and 60°. The wedge filters are mounted below the collimator assembly.

1.2. Photon Interaction Mechanisms

Photons, unlike charged particles, may undergo a few or no interactions as they pass through matter. In each interaction secondary ionizing particles which may be charged (usually electrons) or uncharged (usually photons) are created. Secondary charged particles deposit their energy in close vicinity, however secondary photons may travel long distances before making an interaction.

The main photon interactions in matter are photoelectric absorption (Sauter, 1931), coherent and incoherent (Compton) scattering (Klein and Nishina, 1929; Compton and Allison, 1935), pair and triplet production (Davies et al., 1954; Motz et al., 1969; Tsai, 1974) and nuclear photo-effect. The total interaction cross-section is given as:

$$\sigma = \sigma_{pe} + \sigma_{coh} + \sigma_{incoh} + \sigma_{pair} + \sigma_{trip} + \sigma_{phn} \quad (1.1)$$

In a scattering process, the photons may scatter isotropically or anisotropically related to the direction of the incoming photon and its polarization. The differential cross-section which is related to the probability that particles (radiation) scatters into solid angle $d\Omega$ is defined as (Bransden and Joachain, 1983):

$$\frac{d\sigma(\theta, \phi)}{d\Omega} = \frac{I(\theta, \phi)}{I_0} \quad (1.2)$$

I_0 is the flux of particles of a specified energy, incident on an atom. $I(\theta, \phi)$ is the flux of scattered radiation passing through the solid angle $d\Omega$. θ is the polar (scattering) angle and ϕ is the azimuthal angle. Photon scattering is depicted in Figure 1.8.

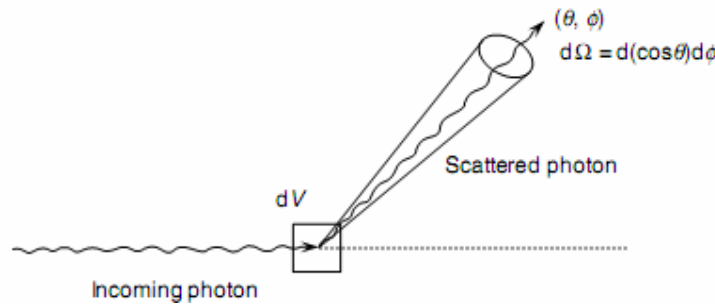


Figure 1.8. Scattering angles and solid angle for photon scattering (Mayles et al., 2007)

The total scattering cross-section per atom is calculated as:

$$\sigma = \int_{4\pi} \frac{d\sigma(\theta, \phi)}{d\Omega} d\Omega \quad (1.3)$$

Photoelectric absorption

In this process, the photon interacts with an atom and absorbed. An atomic electron is ejected from one of the atomic shells with kinetic energy T which is given by:

$$T = h\nu - E_B \quad (1.4)$$

where $h\nu$ is the kinetic energy of the incoming photon and E_B is the binding energy of the ejected electron. The energy transferred to the atom is negligible because of the heavy mass of the nucleus. The process illustrated in Figure 1.9 can only occur with atomic electrons, otherwise momentum cannot be conserved.

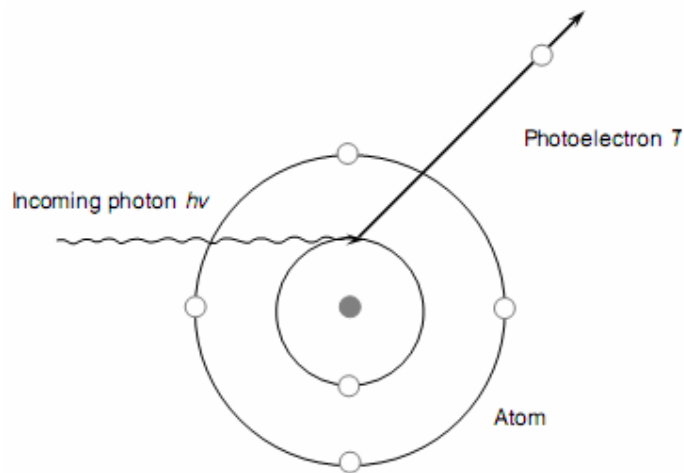


Figure 1.9. Photoelectric absorption (Mayles et al., 2007)

In general, the photoelectric absorption cross-section decreases with increasing energy. Photoelectric absorption is the dominating interaction type for low photon energies (Attix, 1986). However, the cross-section has a series of discontinuities, named absorption edges corresponding to binding energies of the atomic shells, below which the photon doesn't have enough energy to eject certain electrons. Thus the photoelectric absorption cross-section increases suddenly above the edges.

The photo electric cross-section for energies above K-edge decreases approximately as $h\nu^{-3}$ and depends strongly on the atomic number, scaling as (Evans, 1955):

$$\sigma_{pe} \sim Z^n \quad (1.5)$$

The constant n as a function of energy is given in Figure 1.10.

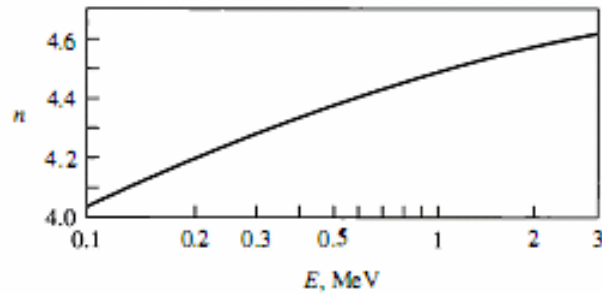


Figure 1.10. The constant n in Equation 1.5 as a function of photon energy (Evans, 1955)

The vacancy left by the ejected electron is filled with electrons in the outer shells. The energy which is equal to the difference in the binding energies of an electron in the two shells is released either as emission of a photon or an electron from an outer shell. The emitted photon is named as a characteristic X-ray since the binding energies of electrons are fixed for an atom. The characteristic X-rays are emitted isotropically. The emitted electron is known as Auger electron whose kinetic energy is equal to the energy released in the transition minus its binding energy. The probability of a characteristic X-ray emission is termed as the fluorescence yield, ω and the Auger electron is emitted with the probability of $1 - \omega$.

Compton (Incoherent) scattering

In Compton scattering, the photon transfers a part of its energy to an atomic electron which is ejected from the atomic shell. In this process the electron can be considered as free. This is an adequate assumption for photon energies that exceed the binding energies of the atomic electrons. The process in which an incoming photon of energy $h\nu$ is scattered with the energy of $h\nu'$, is shown in Figure 1.11.

The energy $h\nu'$ of the scattered photon is calculated as:

$$h\nu' = \frac{h\nu}{1 + \alpha(1 - \cos \theta)} \quad (1.6)$$

where $\alpha = h\nu / (m_0 c^2)$ and m_0 is the rest mass of the electron. The transferred energy which is the kinetic energy of the struck electron is given as:

$$T_e = h\nu - h\nu' \quad (1.7)$$

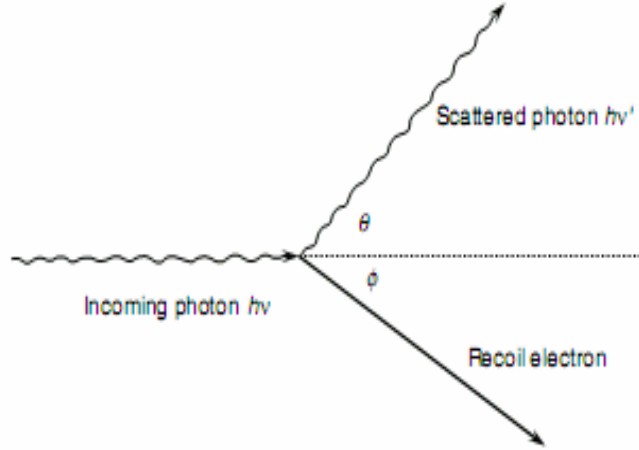


Figure 1.11. Compton scattering (Mayles et al., 2007)

The highest energy transfer occurs for $\theta = 180^\circ$ (backward scattering of the photon).

The differential Klein–Nishina cross-section per electron for Compton scattering is given by (Klein and Nishina, 1929):

$$\frac{d_e \sigma_{KN}}{d\Omega} = \frac{r_e^2}{2} \left(\frac{h\nu'}{h\nu} \right)^2 \left[\frac{h\nu'}{h\nu} + \frac{h\nu}{h\nu'} - \sin^2 \theta \right] \quad (1.8)$$

where r_e is the classical electron radius. At low energies, the differential Klein–Nishina cross-section per electron reduces to classical Thomson differential cross-section which is given by:

$$\frac{d_e \sigma_{Th}}{d\Omega} = \frac{r_e^2}{2} (1 + \cos^2 \theta) \quad (1.9)$$

The effect of electron binding on the incoherent cross-section is quantified by the incoherent scattering function $S(x,Z)$ (Mayles et al., 2007).

$$\frac{d\sigma_{incoh}}{d\Omega} = \frac{d_e \sigma_{KN}}{d\Omega} S(x,Z) \quad (1.10)$$

The incoherent scattering function is assumed to be a function of momentum transfer and the atomic number. The momentum transfer related parameter, x is given by:

$$x = \frac{\sin(\theta/2)}{\lambda} \quad (1.11)$$

where λ is the wavelength of the primary photon. The incoherent scattering function is related to the probability that the electron will be ejected from the shell as a result of momentum transfer. $S(x,Z)$ has its lowest value for $\theta = 0$ and is monotonically increasing function of the momentum transfer (x).

Coherent (Rayleigh) scattering

In Rayleigh scattering, the photons are collectively scattered by the atomic electrons and lose no energy. The atomic electrons behave like a dipole radiation source due to oscillations caused by the electric field of the incident photon and emit a new photon in a different direction. The differential cross-section for coherent scattering is given as:

$$\frac{d_e \sigma_{coh}}{d\Omega} = \frac{d_e \sigma_{Th}}{d\Omega} F^2(x,Z) \quad (1.12)$$

$F(x,Z)$ is the atomic form factor which is a decreasing function of x . At low photon energies and small momentum transfers, the coherent total scattering cross-section is approximately given by (Salvat, 2003):

$$\sigma_{Ra} \cong \frac{8}{3} \pi r_e^2 Z^2 \quad (1.13)$$

At higher energies the cross-section scales as $(h\nu)^{-2}$.

Pair and triplet production

In this process, the photon disappears in the vicinity of a Coulomb field of an atomic nucleus and an electron pair – a positron and a negatron – is created. This effect occurs at photon energies higher than $2 m_0 c^2$ (the sum of rest mass energies of two electrons). The two electrons tend to be emitted in forward direction thus presence of the nucleus is essential for conservation of momentum. The total kinetic energy of the electron pair is the energy of the incoming photon minus $2 m_0 c^2$.

The pair production process may also occur in the electric field of an atomic electron. The atomic electron will be ejected from the atomic shell and three

electrons appear. Thus the process is called triplet production. The energy threshold for the process is $4 m_0 c^2$.

The pair and triplet production cross-sections scale as Z^2 and Z respectively and increase steadily with increasing photon energy.

Nuclear Photoeffect

Photon can be absorbed in a nuclear reaction if the photon energy exceeds the binding energy of a nucleon. As a result, one or more nucleons are ejected from the nucleus. The cross-section for the nuclear photoeffect depends on both the atomic number and the atomic mass and has an energy threshold. A giant resonance peak of cross-section occurs between energies of 5 and 40 MeV depending on the element (Mayles et al., 2007). The cross-section can contribute between 2% (high-Z element) and 6% (low-Z element) to the total cross-section.

1.3. Electron Interaction Mechanisms

The three primary interaction mechanisms of electrons, in matter in the energy range between a few hundred eV and 50 MeV (Mayles et al., 2007), are collisions with bound electron (Møller scattering) (Møller, 1932), bremsstrahlung (Koch and Motz, 1959; Tsai, 1974) and elastic scattering largely due to the heavy (positively charged) nucleus (Mayol and Salvat, 1997). The inelastic interactions are termed as “collisions” whereas bremsstrahlung losses are termed as “radiative losses”.

Unlike photons, electrons interact with matter very frequently with small energy losses along their paths. This leads to the concept of stopping power which is defined as the average energy loss (dE) per unit distance (ds). The stopping powers are usually expressed as mass stopping power which is given as $(1/\rho)(dE/ds)$.

The total stopping power is the sum of collision and radiative stopping powers and given as:

$$\left(\frac{dE}{ds}\right)_{tot} = \left(\frac{dE}{ds}\right)_{col} + \left(\frac{dE}{ds}\right)_{rad} \quad (1.14)$$

Collisions

Electrons lose their energy in the materials and energies of interest in radiotherapy primarily due to Coulomb interactions with the bound electrons. A trail of ionizations and excitations are created along the particle's path. Occasionally delta rays which are secondary electrons with considerable ranges of their own are created with sufficient energy transfer. In quantum mechanics, the incident and struck electron after a collision cannot be distinguished experimentally. The electron of lower energy after collision is treated as the struck particle.

The track of a charged particle is illustrated in Figure 1.12.

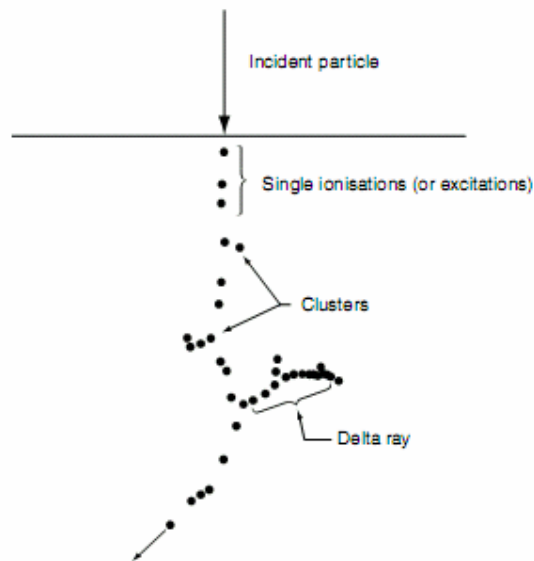


Figure 1.12. Representation of the track of a charged particle in matter (ICRU, 1970)

The Coulomb interaction between a fast electron and a bound electron in the medium is shown in Figure 1.13. The incoming electron is moving at a speed v in a direction opposite to axis x . The bound electron can be assumed to be free, since its binding energy is negligible compared to the energy it receives. The energy transfer to the bound electron is given by (Mayles et al., 2007):

$$Q = \frac{2k^2 z^2 e^4}{mb^2 v^2} \quad (1.15)$$

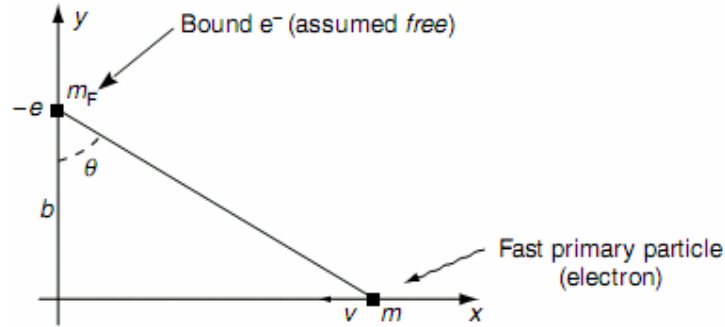


Figure 1.13. Interaction between a fast primary charged particle and a bound electron (Nahum, 1985)

The full relativistic quantum-mechanical cross-section for Coulomb interaction between free electrons is given as (Møller, 1932):

$$\frac{d\sigma}{d\varepsilon} = \frac{2\pi e^4 k^2}{T m_e v^2} \left[\frac{1}{\varepsilon^2} + \frac{1}{(1-\varepsilon)^2} + \left(\frac{\tau}{\tau+1} \right)^2 - \frac{2\tau+1}{(\tau+1)^2} \frac{1}{\varepsilon(1-\varepsilon)} \right] \quad (1.16)$$

where

T is electron kinetic energy

$\varepsilon = Q/T$ is the ratio of energy transfer to electron kinetic energy

$\tau = T / m_e c^2$ is the ratio of kinetic energy to electron's rest mass

v is the electron velocity

$k = 8.9875 \times 10^9 \text{ Nm}^2\text{C}^{-2}$

If the fast electron passes an atom at a relatively large distance, the Coulomb force affects the atom as a whole with the possibility of excitation or ionization of a valence-shell. The reaction in which only a small amount of energy is transferred is termed as soft collision. When the electron passes relatively close to the atom, then it may interact with a single bound electron and the struck electron may be ejected with appreciable kinetic energy. The ejected electrons are known as knock-on electrons or delta rays and interaction is named as hard collision. Although hard collisions are rarer than soft ones, the contributions of both types of collisions to the total energy loss are comparable in magnitude.

If an electron is ejected from an inner shell, then characteristic X-rays or Auger electrons may be released.

Collision stopping power

The collision stopping power is calculated from:

$$\frac{1}{\rho} \left(\frac{dE}{ds} \right)_{col} = N_A \left(\frac{Z}{A} \right) \int_{Q_{min}}^{Q_{max}} \frac{d\sigma}{dQ} dQ \quad (1.17)$$

where N_A is the Avogadro's number

Z and A are atomic and mass number respectively

Q_{max} and Q_{min} are maximum and minimum energy transfer respectively

The quantum-mechanical expression for the electron mass collision power is given in the units of MeV cm² g⁻¹ as (ICRU, 1984a):

$$\frac{1}{\rho} \left(\frac{dE}{ds} \right)_{col} = 0.1535 \frac{1}{\beta^2} \left(\frac{Z}{A} \right) \left\{ \ln \left[\frac{\tau^2 (\tau + 2)}{2(I / m_e c^2)^2} \right] + F(\tau) - \delta \right\} \quad (1.18)$$

$$F(\tau) = 1 - \beta^2 + \left[\tau^2 / 8 - (2\tau + 1) \ln 2 \right] / (\tau + 1)^2 \quad (1.19)$$

where

$$\beta = v / c$$

r_e is the electron radius

I is the mean excitation energy

δ is the density-effect correction

I can be calculated theoretically for only monoatomic gases. It must be calculated from measurements of stopping power or range. Values of I , based largely on experimental data, are provided in ICRU (1984b).

If the stopping medium has high density, the electric field of the atoms distant from the electron track is reduced due to the polarization of the intervening atoms. Thus the contribution of the distant collisions to the stopping power is reduced. This is named as density or polarization effect (Fermi, 1940; Sternheimer, 1961; ICRU 1984a) and represented in equation 1.18 via the term δ .

Radiative losses

Bremsstrahlung radiation is produced in the result of acceleration of the electrons in the strong electric field of a nucleus. The acceleration is proportional to the ratio of the atomic number of the nucleus to the mass of the moving particle (Z/m) and the intensity of the radiation produced is proportional to $(Z/m)^2$. The radiation is emitted mostly in forward direction

This is relatively an unimportant energy loss mechanism in low-Z medium below about 10 MeV. The cross-section for this non-classical process is extremely complicated. However it may be given approximately as (Mayles et al., 2007):

$$\frac{d\sigma_{rad}}{dh\nu} \propto \frac{1}{h\nu} \quad (1.20)$$

Radiation stopping power

Numerical procedures are used to calculate the radiative stopping powers, since, unlike collisional losses, no single analytical formula can be used to calculate them.

The efficiency of bremsstrahlung varies linearly as Z^2 . Therefore, bremsstrahlung losses are considerably greater in materials with high Z. As seen from equation 1.17 the collision energy loss rate is proportional to Z. Furthermore, the radiative and collision energy loss rate increase with energy linearly and logarithmically respectively. Thus, bremsstrahlung is the predominant energy loss mechanism for electrons at high energies.

The ratio of radiative and collision stopping powers for an electron of total energy E (in MeV) is given by the following approximate formula (Turner, 2007):

$$\frac{(dE/ds)_{rad}}{(dE/ds)_{col}} \cong \frac{ZE}{800} \quad (1.21)$$

Radiation Yield

The fraction of the initial electron energy (E_0) that is lost to bremsstrahlung in slowing down to rest, is known as the radiation yield and given by (Mayles et al., 2007):

$$Y(E_0) = \frac{1}{E_0} \int_0^{E_0} \frac{(dE/ds)_{rad}}{(dE/ds)_{col} + (dE/ds)_{rad}} dE \quad (1.22)$$

$Y(E_0)$ varies with Z and E_0 approximately linearly.

Energy-loss straggling

The stopping power is an average value for the energy loss per unit distance and fluctuations occur about the mean. This is known as energy-loss straggling and illustrated in Figure 1.14. The energy of the electrons incident on a thin target and the mean energy loss of the electrons emerging from the target are E_0 and ΔE_{tot} respectively. ΔE_{tot} can be calculated by multiplying the thickness of the absorber and the total stopping power. The distribution of the individual energy losses is denoted with the width Γ . If the individual energy losses are much smaller than the energy of the incident photons, then the width will be narrow.

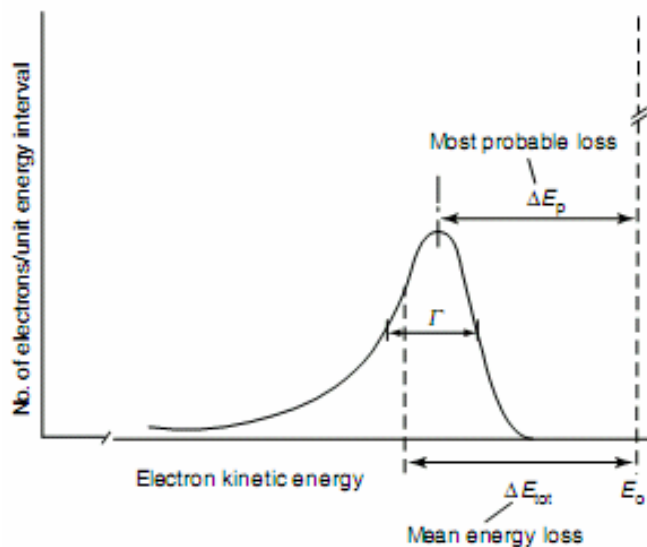


Figure 1.14. Energy broadening because of energy-loss straggling after the passage of a monoenergetic electron beam (energy E_0) through a thin absorber. (Nahum, 1985.)

Continuous-slowing-down-approximation and range

Electrons interact with matter in a quasi-continuous fashion along their tracks. The Continuous-Slowing-Down-Approximation (csda) range is defined as below:

$$r_o = \int_0^{E_0} \left(\frac{ds}{dE} \right)_{tot} dE \quad (1.23)$$

This distance is the average path length traveled by an electron with the initial kinetic energy of E_0 and expressed in g cm^{-2} . The range is always greater than the average penetration depth. As a rule of thumb, the average penetration depth is roughly half of the range. Electrons, unlike photons or heavy charged particles, can scatter in large angles in single collisions. Furthermore the wandering of the tracks is augmented at low energies by the increased and almost isotropic elastic scatterings. The electron tracks in matter are illustrated in Figure 1.15.

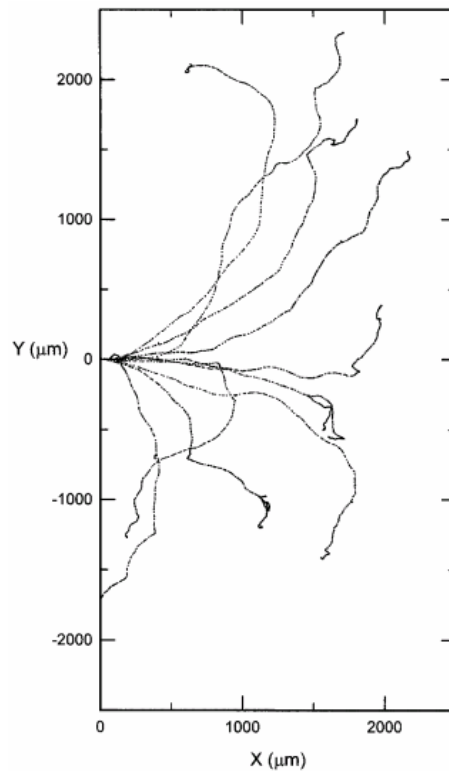


Figure 1.15. Calculated tracks (projected into the X–Y plane of the figure) of ten 740-keV electrons entering a water slab normally from the left at the origin (Turner, 2007)

Tabulated data

Total mass stopping powers, mass collision stopping powers, mass radiative stopping powers, csda ranges, radiation yields and density-effect corrections are provided by ICRU (1984a)

1.4. Thesis Objectives

The aims of this study are:

- To perform Monte Carlo calculations for the BIMRT technique (for which only dose distribution results in mathematical phantoms are available) with a detailed head phantom to show the usability of voxel-geometry phantoms for microdosimetric calculations by comparing the results with the semi-quantitative experimental ones (Dilmanian et al., 2008);
- To analyse the effect of Au contrast agent on dose distribution inside the target region and the surrounding tissue;
- To evaluate the suitability of another radiation source as the X-ray source for the MRT technique.

1.5. Outline of the Thesis

In the second chapter, the suitability of the Monte Carlo code MCNPX was evaluated for micrometric dosimetry at low X-ray energies. In the third chapter, Bidirectional Interlaced Microbeam Radiation Therapy (BIMRT) technique was simulated with orthogonally interlaced thick microbeam (minibeam) arrays and dose distribution calculations were performed in detailed human head phantom. Furthermore, the dose enhancement due to deposition of gold contrast agent in the target volume is determined. In the fourth chapter, linear accelerator was evaluated as the X-ray source for the stereotactic MRT technique. The optimum beam shape, size and interval were determined with calculations performed in a cylindrical water phantom. Depth-dose distributions calculated in a detailed human head phantom were compared with the ones for the BIMRT technique. The stereotactic MRT was simulated in a spherical mathematical head phantom. The general conclusion for the whole study is given in the fifth chapter.

1.6 The Monte Carlo Simulations

Since the micrometric dosimetry is still a challenge, MC calculations are important for the development of the MRT technique. MCNPX version 2.5.0, a general purpose MC radiation transport code that tracks nearly all particles at nearly all energies (Pelowitz 2005), was selected for the MC calculations.

The MCNPLIB04 photon cross-section library was used for the calculations (Pelowitz 2005). It was derived from the ENDF/B-VI.8 data library that was derived from EPDL97. It includes incoherent, coherent, photoelectric and pair production cross sections, form factor and fluorescence data for incident energies from 1 keV to 100 GeV and Z equal to 1 to 100. The EL03 electron-transport library was used (Pelowitz 2005). Photon–electron coupled simulations were performed with 1keV energy cutoff. The relative errors given in the paper correspond to one standard deviation.

2. EVALUATION OF THE SUITABILITY OF THE MONTE CARLO CODE MCNPX FOR MICROMETRIC DOSE DISTRIBUTION CALCULATIONS AT LOW X-RAY ENERGIES

The dose distribution calculation studies in the literature (Siegbahn et al., 2005; Siegbahn, 2007; Spiga et al., 2007), performed with other Monte Carlo codes were done with MCNPX to evaluate the suitability of the code for micrometric dosimetry at low X-ray energies.

A cylindrical water phantom of 16 x 16 cm dimensions was used in the simulations. X-rays with 50, 100 and 150 keV energies and experimental ESRF spectrum were simulated. The ESRF spectrum contains photons in the interval from 30 keV up to 600 keV with a mean energy of 107 keV (Siegbahn et al., 2005). However, the fraction of photons with energies above 300 keV is small. The spectrum given in Figure 2.1 corresponds to the filter combination used in the MRT preclinical trials.

The beam divergence of approximately 1 mrad was neglected for simplicity and consistency with the former studies. The numbers of histories were selected so as to have relative errors under 5% for the regions taken into consideration.

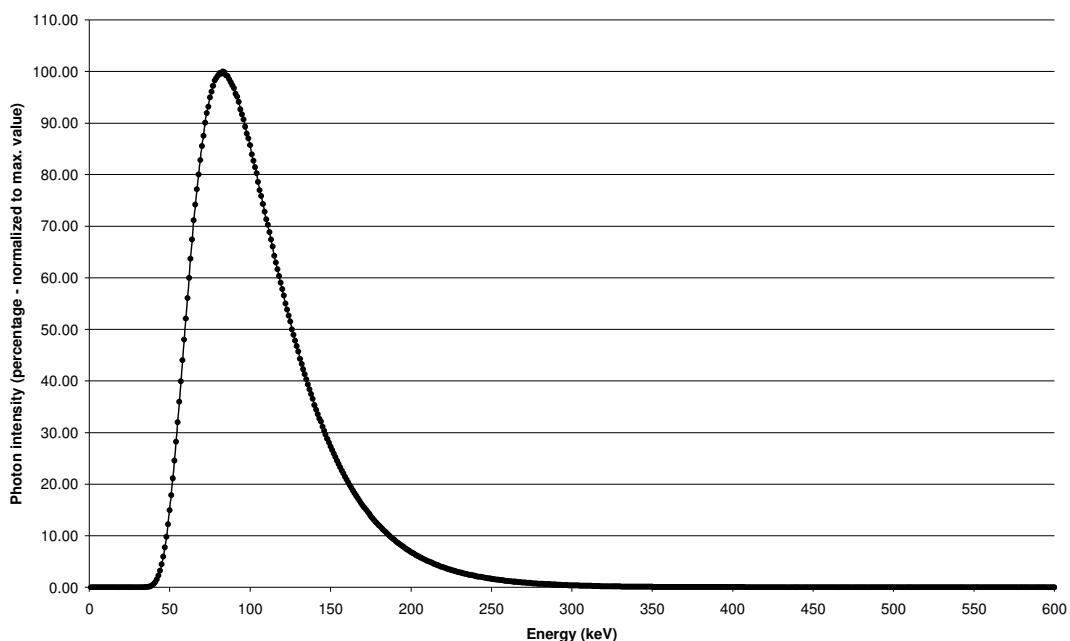


Figure 2.1. ID17 beamline spectrum that is used for MRT

2.1. Depth – Dose Distributions

Two depth – dose distributions for a single planar microbeam, calculated in water with different tally bin geometries, are given in Figure 2.2. The dimensions of the beam are 1 cm x 25 μm (height x width). The selected number of histories is $1\text{e}7$. Both dose distribution curves were obtained with tally bins of 1 cm height and 1 mm length (in beam's path). The curves were normalized to their respective maximum values.

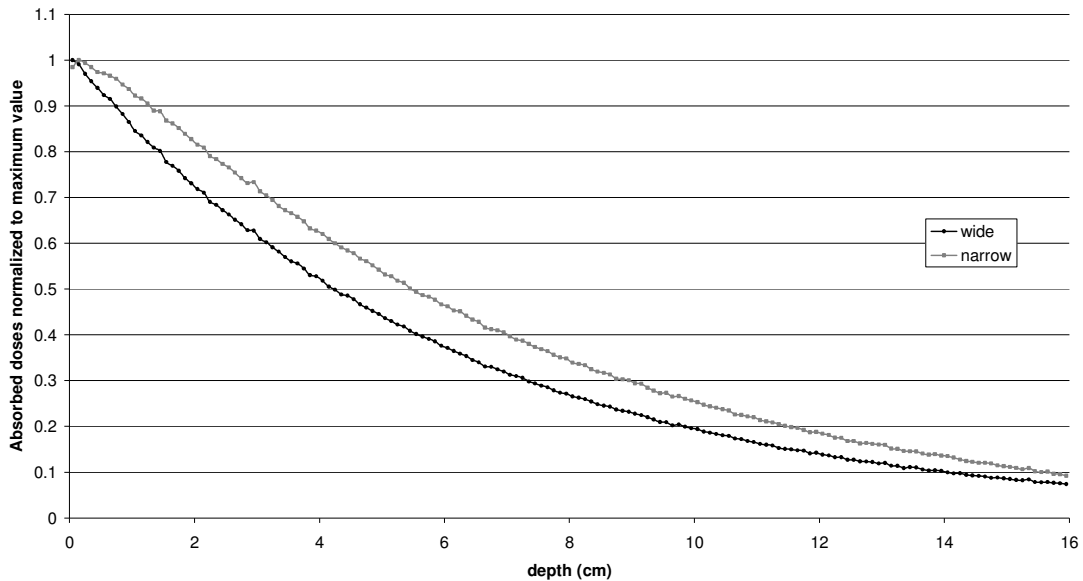


Figure 2.2. Normalized depth – dose distributions obtained for different tally bin geometries

On the upper curve doses were scored with wide tally bins of 15 cm width. The important characteristic of this tally geometry is that the energy deposition due to the radiation scattered from the beams paths is scored. Dose buildup in the depth of 1 cm is observed because of this. On the lower curve, doses were scored with the tally bins that are just as thick as the planar microbeam. An immediate fall is observed in the lower curve since scattered radiation is not taken into account in this scoring geometry. From the curves, the relative energy deposition outside the beam's path, due to scattered radiation, is observed to increase.

2.2. Lateral Dose Distribution around a Cylindrical Pencil Microbeam

Lateral dose distribution perpendicular to a cylindrical pencil microbeam is given in Figure 2.3. Calculations were performed for a 25 μm -diameter-pencil beam with

100 keV energy. The doses were scored in the water phantom, between 7 – 8 cm depths and in annular bin geometries of 2 μm thickness around the microbeam. 1×10^7 was used as the number of histories. Splitting and Russian Roulette variance reduction techniques were used since the standard deviations increase with the distance from the microbeam. The steep fall in the curve, beside the beam boundary is discernible.

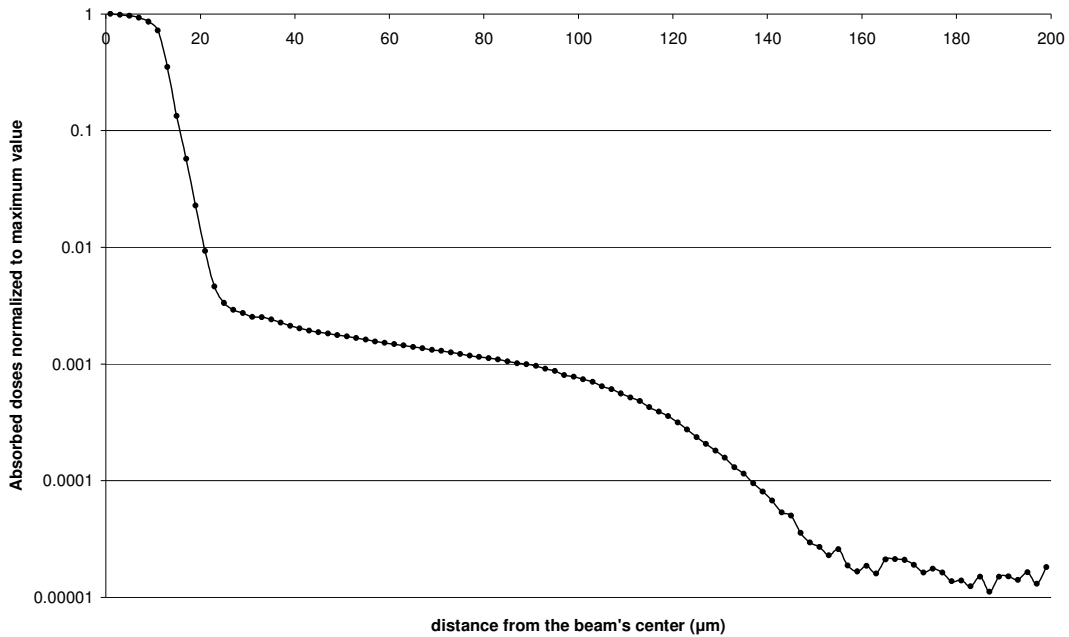


Figure 2.3. Lateral dose distribution beside a 25 μm -diameter cylindrical pencil beam between 7 – 8 cm depths

2.3. Angular Distributions and Spectrums of the Secondary Particles

Simulations were performed for planar microbeams of 1 cm height and 25 μm width and of different energies (50, 100, 150 keV and ESRF spectrum). Spectrums and angular distribution of scattered secondary photons and electrons were calculated at the plane that is 12.5 μm distant from the beam center and between 7 – 8 cm depths. Since scattering around the beam central axis is simulated symmetrically in MCNP, the angular distributions of the secondary particles are given in polar angles. The angular distributions of secondary particles are given between 0° (forward scattered) and 180° (backward scattered).

Number of histories was selected as 1×10^8 . The spectrum plots were generated by MCNPX and the angular distributions were normalized to maximum flux values.

The secondary electron spectrums calculated at the boundary of planar beams are given in Figure 2.4.

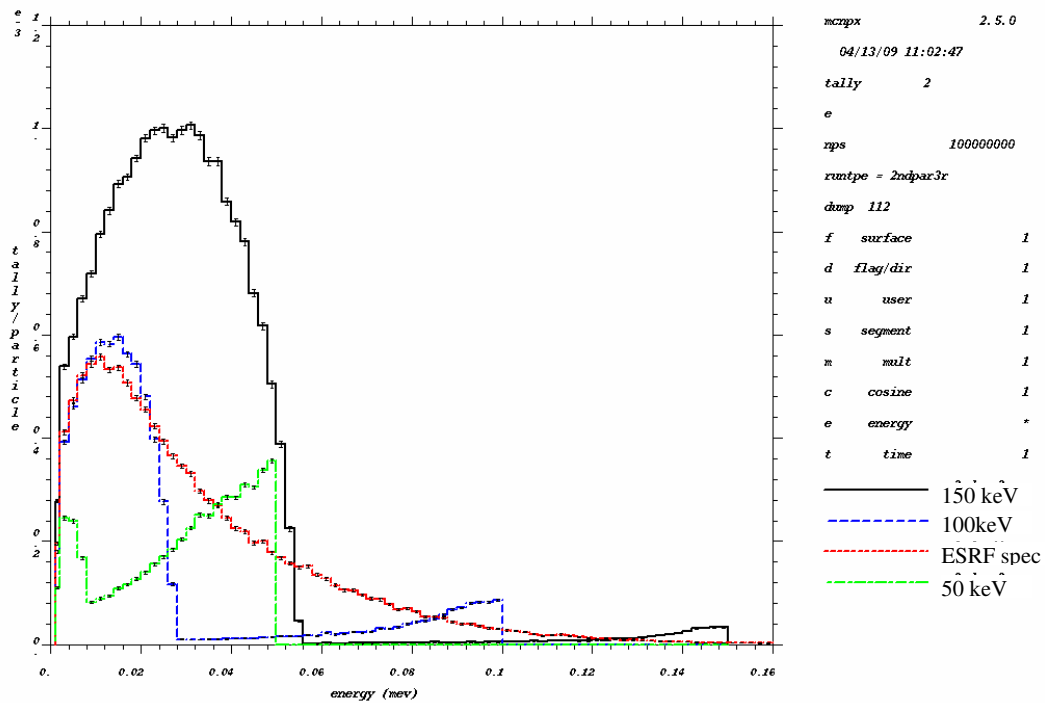


Figure 2.4. Secondary electron spectrums calculated at the planar beam boundaries

There aren't any discernible peaks observed for the X-rays with ESRF spectrum. Photo-electron peaks are observed at energies close to incoming beam energies for mono-energetic microbeams. The 50-keV-Xrays have the highest probability for photo-electric effect among the mono-energetic X-rays. The peaks observed at the low energy regions are due to Compton scattering.

The angular distributions of the secondary electrons are given in Figure 2.5. The peaks are observed at approximately 50° except for 50-keV X-rays (peak is at 75°).

The secondary photon spectrums are given in Figure 2.6. There isn't any discernible feature observed for the X-rays with ESRF spectrum. The effect of Compton scattering is clearly seen for mono-energetic microbeams. The peaks on the curves at low energy regions are due to back scatterings and the peaks at higher energies are due to scattering in the forward direction.

Angular distributions of secondary photons, calculated at the beam boundaries, are given in Figure 2.7. There aren't substantial differences between the curves for different energies.

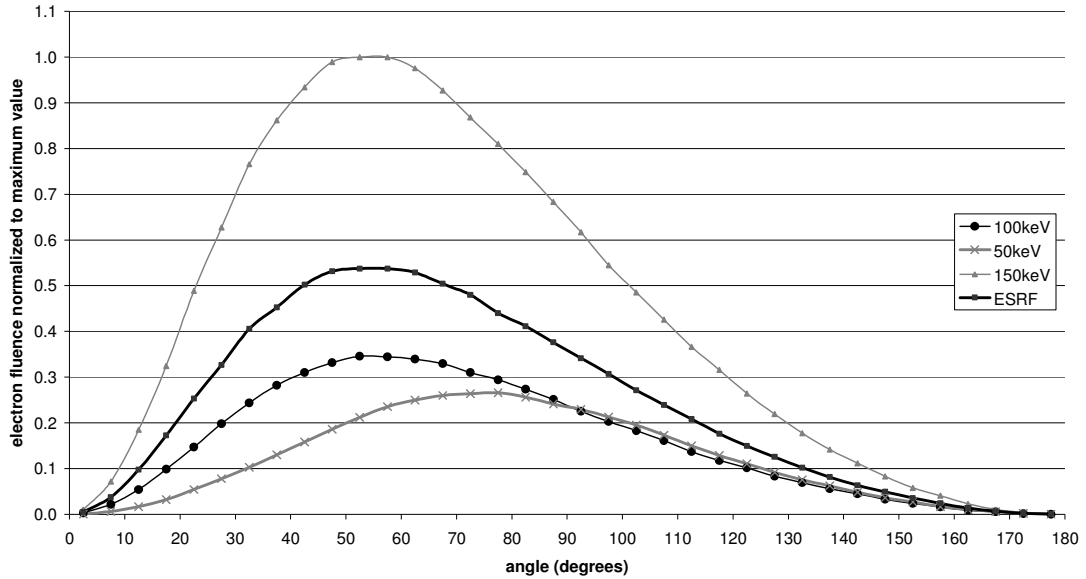


Figure 2.5. Angular distributions of secondary electrons calculated at the planar beam boundaries

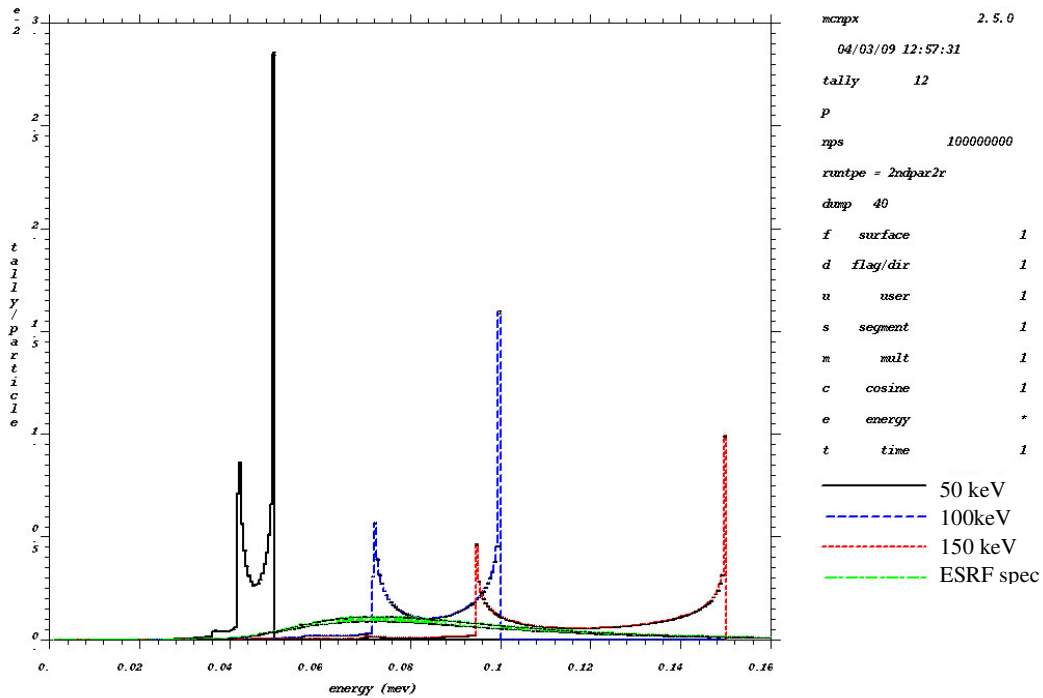


Figure 2.6. Secondary photon spectrums calculated at the planar beam boundaries

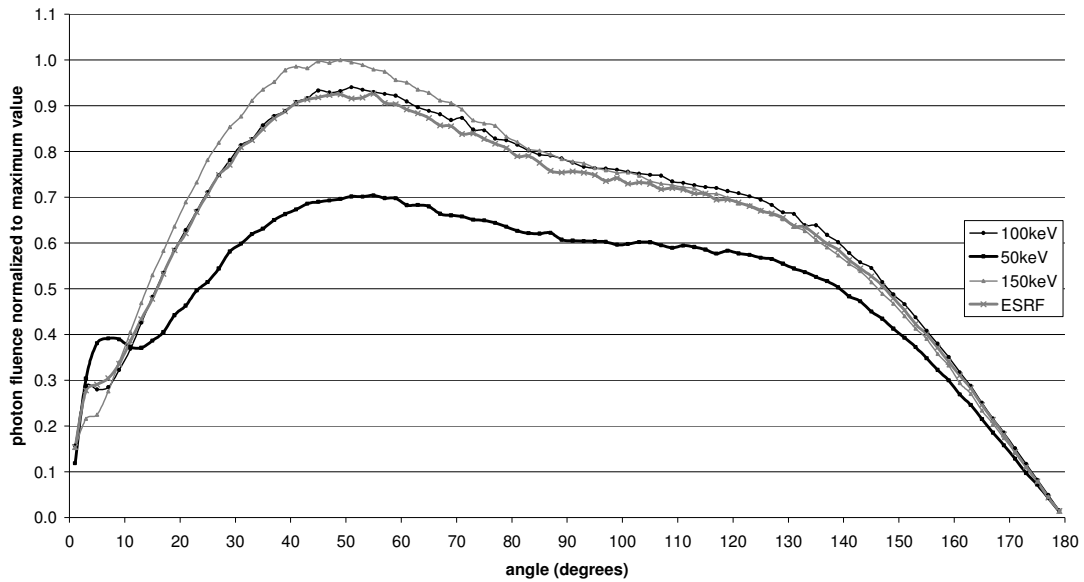


Figure 2.7. Angular distributions of secondary photons calculated at the planar beam boundaries

2.4. Effect of Microbeam Thickness on Dose Distributions

Lateral dose distributions were calculated for beam thicknesses of 25 μm , 50 μm and 75 μm and the effect of beam thickness on in-beam doses (peak dose) was investigated. Dose calculations were performed in water phantom, between 7 – 8 cm depths, for beam height of 1 cm and X-rays of ESRF spectrum. The photon fluences in the simulations were adjusted to be the same. The results were normalized to the maximum values which were calculated for the beam of 75 μm thickness. Number of histories was selected as 1×10^7 . Lateral dose distributions calculated for different beam thicknesses are given in Figure 2.8. Peak doses are observed to increase with beam thickness.

2.5. Depth Dose Distributions for Microbeam Arrays

Beam arrays of 3 cm height and 3 cm width are formed with parallel planar beam arrays of dimensions 3 cm x 25 μm , and 100 μm and 200 μm center-to-center (ctc) distances. The distributions of the doses absorbed in the path of the central beam (peak dose), the doses absorbed between the beam's paths (valley doses) and peak-to-valley dose ratios (PVDR) with respect to depth were calculated.

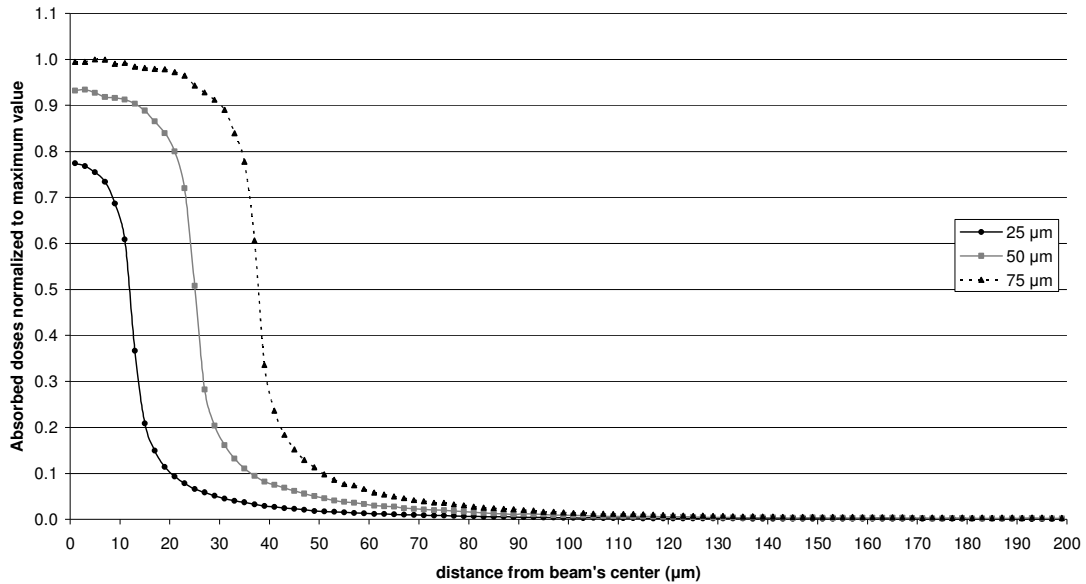


Figure 2.8. Lateral dose distributions for beam thicknesses of 25µm, 50µm and 75µm

Lateral dose distributions were calculated in the former studies (Siegbahn et al., 2005; Siegbahn, 2007; Spiga et al., 2007) for single microbeams and the results were superimposed to have the dose distributions for the beam arrays. In this study, every microbeam in the beam arrays (301 and 151 beams for ctc distances of 100 µm and 200 µm respectively) was simulated one by one. Number of histories was selected as 1×10^8 . The peak and valley dose distributions are given in Figure 2.9. The values were normalized to the maximum peak dose. The peak-to-valley dose ratios are given in Figure 2.10.

Peak and valley doses are observed to be higher for the ctc distance of 100 µm. However, peak-to-valley dose ratios are higher for 200-µm-ctc distance. The dose buildup is observed in the valley doses in the first centimeters. PVDR's increase as approaching to 16-cm-depth, since the valley doses decrease due to decrease in back scattered radiation as the opposite surface of the cylindrical phantom is reached.

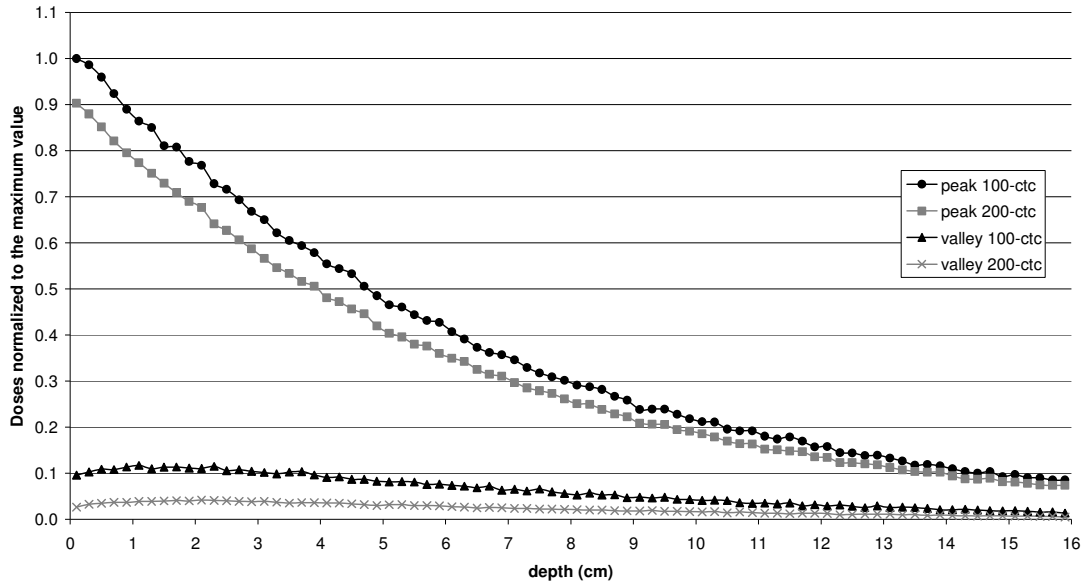


Figure 2.9. Depth – peak dose and depth – valley dose distributions for 100- and 200- $\mu\text{m-ctc}$ distances

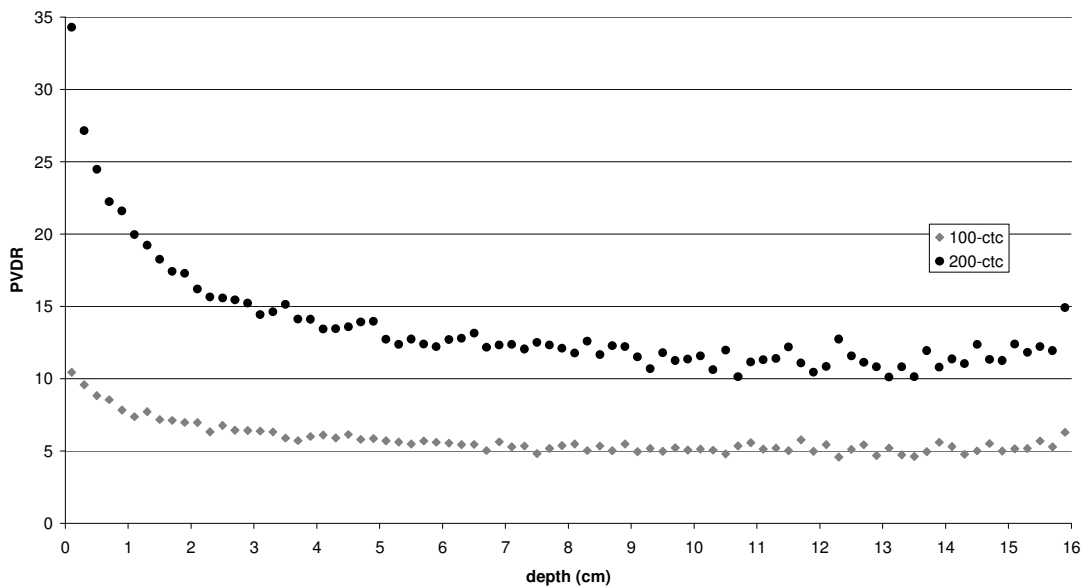


Figure 2.10. Depth – PVDR distributions for 100- and 200- $\mu\text{m-ctc}$ distances

2.6. Conclusion

The results are consistent with the ones obtained with different Monte Carlo codes in the literature. This shows that the code MCNPX and the cross-section libraries used are suitable for calculation of absorbed doses in micrometric geometries and low X-ray energies.

3. MONTE CARLO SIMULATION OF MICROBEAM RADIATION THERAPY WITH AN INTERLACED IRRADIATION GEOMETRY AND AN AU CONTRAST AGENT IN A REALISTIC HEAD PHANTOM

Dose distribution calculations for bidirectional interlaced irradiation geometry were performed with the MC code MCNPX. Simulations were performed with a realistic Zubal head phantom model (Zubal et al., 1994a; 1994b; 1995; Evans et al.; 2001) and a homogenized model derived from the Zubal phantom. The effects of the structure of the realistic phantom on dose distribution were analyzed.

In most of the previous MC studies water phantoms were used (Slatkin et al., 1992; Stepanek et al., 2000; De Felici et al., 2005; Siegbahn et al., 2005; Spiga et al., 2006; 2007; Dilmanian et al., 2006). To our knowledge the only MC dosimetric studies performed in MRT using mathematical head phantoms are those of Orion et al. (2000), Prezado et al. (2009a) and Martinez-Rovira et al. (2010). In Martinez-Rovira et al.'s (2010) study, it was pointed out that the use of realistic phantoms is essential for correct dose assessment. The head phantom used in this study was created from transverse MRI images of a human male head and it is far more realistic than the ones used in previous studies, since it contains the critical structures and important materials of the head.

Dose distributions were determined in the targets of dimensions $20 \times 6.8 \times 20 \text{ mm}^3$ and $20 \times 20 \times 20 \text{ mm}^3$ and in surrounding tissue. The locations of the targets are similar to that of the target selected by Dilmanian et al. (2008). Depth – dose profiles and dose falloffs at the edges of the targets were evaluated for cases with and without an Au contrast agent deposited in the target region and surrounding tissue.

3.1. Modified Zubal Head Phantom and Homogenized Phantom

A modified voxel-geometry Zubal head phantom (Evans et al., 2001) was used in this study. This phantom is based on the Zubal phantom (Zubal et al., 1994a; 1994b; 1995) which was created from 124 transverse MRI images of a healthy human male head. The head and outer air space in the close vicinity were formed with $85 \times 109 \times 120$ lattice of voxels of dimensions $2.2 \times 2.2 \times 1.4 \text{ mm}^3$ (at x, y and z dimensions, the coordinates are given in Figure 3.3). 29 critical structures of the head were identified by their individual universes with 15 materials. The voxel-

geometry part was attached to a simplistic mathematical model of the neck and torso, under the upper jaw.

Since low energy photons and electrons were transported, the secondary photons and electrons scattered from the beams are absorbed in the close vicinity. Thus, there was no need for other parts of the phantom than the head part. So the part under the lower jaw was excluded and the air space around the head was made smaller.

The lattice elements of the voxel-geomerty Zubal phantom in the MCNP input were read by a computer program developed and the locations and densities of the voxels were determined. A three-dimensional plot of the Zubal phantom (the lower jaw is a mathematical model and is not given in the figure) and two-dimensional slice view, which were obtained by plotting the densities of voxels with respect to the locations, are given in Figures 3.1 and 3.2 respectively.

Simulations were performed with homogenized and realistic (Zubal) head phantoms to study the effect of the structure of the realistic head phantom on the obtained dose distribution. The homogenized phantom was formed with assigning the same material (grey matter) to all voxels pertaining to the head part of the Zubal phantom. The outer dimensions and shape of the homogenized phantom are the same as those of the Zubal phantom. Thus, the target position is same in both cases.

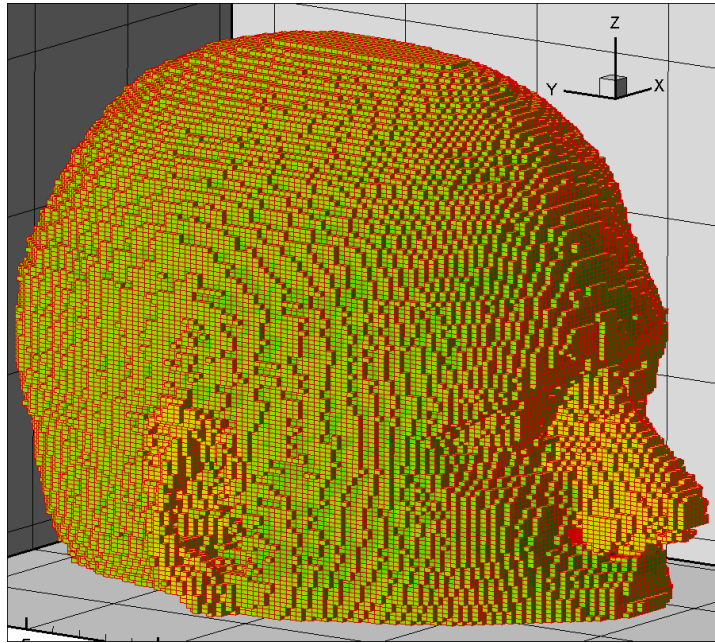


Figure 3.1 3-D view of the modified Zubal head Phantom (lower jaw is not given)

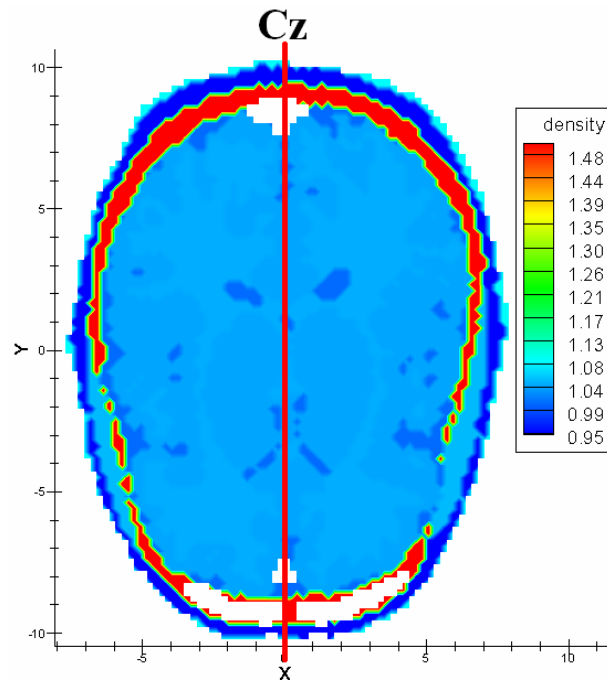


Figure 3.2 2-D slice view of modified Zubal head Phantom (densities in g / cm³)

3.1. The Irradiation Geometry and Sampled X-Ray Energies

The x-ray energies were sampled from the experimental ESRF spectrum (Siegbahn et al., 2005).

The selected irradiation geometry, given in Figure 3.3, is similar to that of Dilmanian et al.'s (2008) experimental study. The dimensions of the targets are $20 \times 6.8 \times 20 \text{ mm}^3$, $20 \times 20 \times 20 \text{ mm}^3$. Targets are located at 3 cm lateral to Cz in Figure 3.2, and 6 cm superior to the interauricular line. Arrays are composed of parallel planar beams with 0.68 mm beam thickness, 20 mm beam height and 0.68 mm beam interval. 5 and 15 planar beams were sampled in the orthogonal arrays for targets of dimensions $20 \times 6.8 \times 20 \text{ mm}^3$ and $20 \times 20 \times 20 \text{ mm}^3$, respectively.

The collimators and slits were not incorporated in the model. Unidirectional photon sources were defined close to the phantom's surface.

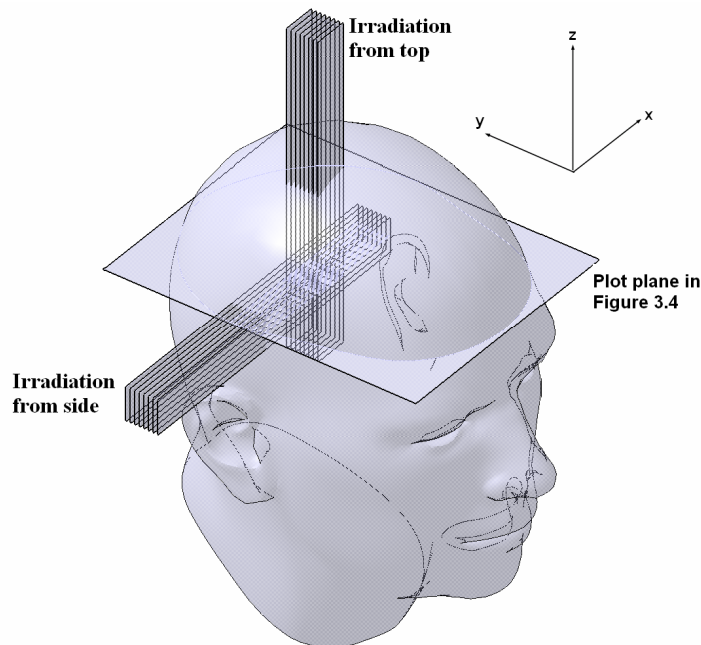


Figure 3.3. Irradiation geometry

3.3. Au Contrast Agent Deposited in Target and Surrounding Tissue

Simulations were performed to determine the effect of an Au contrast agent on the dose distribution in the phantom and dose falloff at the edge of the target region.

Hainfeld et al. (2004) observed elevated concentrations of gold to 7 mg Au/g tumour in mice bearing subcutaneous EMT-6 carcinomas, after a single intravenous injection of 1.9 nm diameter gold particles. At 5 min following the injection the tumour-to-normal muscle Au concentration ratio was given as 3.5:1.0. 7mgAu/g tumour and 2mgAu/g tissue (surrounding tissue) gold concentration values were used in the simulations, on the assumption that they would be applicable in humans (Cho, 2005).

It was assumed that gold concentration was uniform throughout the tumour and for some of the simulations performed, gold was distributed inside the surrounding tissue.

3.4. The Monte Carlo Simulations

Dose distributions in volumes with dimensions which are smaller than those of voxels of the Zubal phantom were calculated with the 'mesh tally' feature of MCNPX. For this type of tally, a grid (meshes), independent of the materials, can be defined inside the medium and used for tallying energy deposition. The voxels were used only to describe the medium in which the radiation transport was simulated, rather than for tallying purpose. Since the tally meshes are independent of the medium, the tally results are given in the unit of 'MeV cm⁻³ per initial particle'. Thus, dose distributions were obtained by dividing the tally results for each mesh by the densities of the corresponding voxels.

Simulations were performed with meshes of dimensions 200 µm × 200 µm × 0.5 cm and with 2 × 10⁸ initial photon histories to observe the two-dimensional dose distribution qualitatively and to decide about the dimensions of the meshes for calculation of in-beam (peak) and valley dose values.

Mesh tallies of dimensions 1 mm × 0.68 mm × 0.5 cm (at x, y and z dimensions; the coordinates are given in Figure 3.3) were defined in the centre of the region where microbeams pass through for depth-dose distribution calculations. At the edges of the target regions, mesh tallies of dimensions 2 cm × 10 µm × 2 cm were defined to determine the dose falloffs at the edges of the targets.

The simulations were performed for the cases in Table 3.1.

Table 3.1 The simulated cases

Case I	15-beam interlacing arrays, without an Au contrast agent, with homogenized head phantom.
Case II	15-beam interlacing arrays, without an Au contrast agent, with realistic head phantom.
Case III	5-beam interlacing arrays, without an Au contrast agent (target dimension was selected as $20 \times 6.8 \times 20 \text{ mm}^3$).
Case IV	15-beam interlacing arrays, with an Au contrast agent in target region only, with 7mg Au/g tumour concentration.
Case V	15-beam interlacing arrays, with an Au contrast agent in target with 7 mg Au/g tumour and in surrounding tissue with 2 mg Au/g tissue concentration.

For each case, simulations were performed for irradiation from the side and the top separately which is analogous to same irradiation times with same beam intensities for irradiation from the side and the top. The tally results for irradiation from the side and the top were summed to obtain dose distribution for interlaced beam arrays. Numbers of histories were selected as 1×10^8 for the simulation pairs.

The depth-in-beam dose distributions for the centre beam and depth-valley dose distributions for the valley region which is next to the centre beam were inspected for the beam array incoming from the side for all cases. Skin entrance, maximum skull bone and maximum brain in-beam doses were compared with target exit doses. Depth – PVDR distributions were calculated. However PVDR values are not relevant for the target region (between $x = -4$ and -2), since this is the unsegmented dose region. The in-beam and valley dose distribution curves represent the in-target doses at this region.

The mid-plane of the reference frame for the calculations is given in Figure 3.3.

3.5. Results

3.5.1. Two-dimensional qualitative dose distribution inside the realistic phantom

Two-dimensional dose distribution in the realistic (Zubal) head phantom is given in Figure 3.4 as a contour plot. The plot plane is indicated in Figure 3.3. Relative error at the distal side of the target is below 15% which is adequate for qualitative assessment for radiation transport in two dimensions. Parallel pattern of the beams is preserved through the phantom. It was decided to calculate the mean in-beam and mean valley doses as a conservative approach. Since the parallel pattern of the beams is preserved, meshes of the same thickness as the beams and valleys could be placed just in the beams' paths and the valley regions. Thus meshes with thickness of 0.68 mm could be used for depth-in-beam and depth-valley dose distribution calculations.

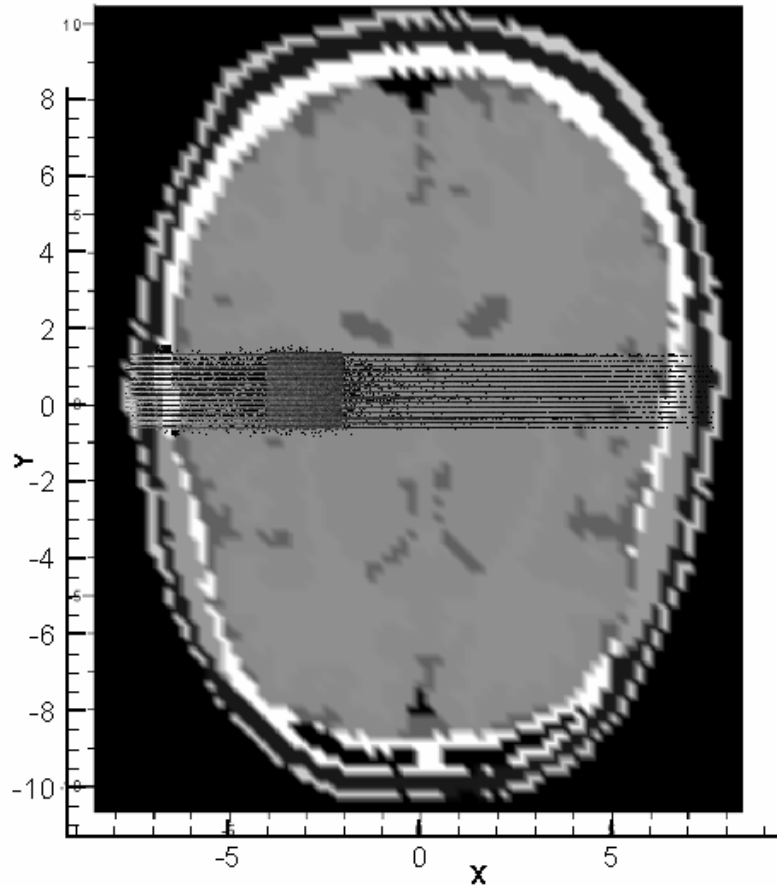


Figure 3.4. Two-dimensional qualitative dose distribution for interlaced irradiation geometry

3.5.2. Lateral dose distributions inside and around the target regions

Lateral dose distributions, averaged through the target volume for all simulated cases, are given in Figure 3.5. Relative errors are less than 0.5% for all cases. The peaks in the curves correspond to in-beam doses for irradiation from the side and the dips correspond to in-beam doses for irradiation from the top. The differences in the in-beam doses are due to different skin entrance-to-target distances for irradiation from the side and the top. To flatten the dose distribution inside the target, the doses administered due to irradiation from the top were multiplied by an adjustment constant which was derived from the ratios of peak values to dip values (analogous to adjusting the irradiation times).

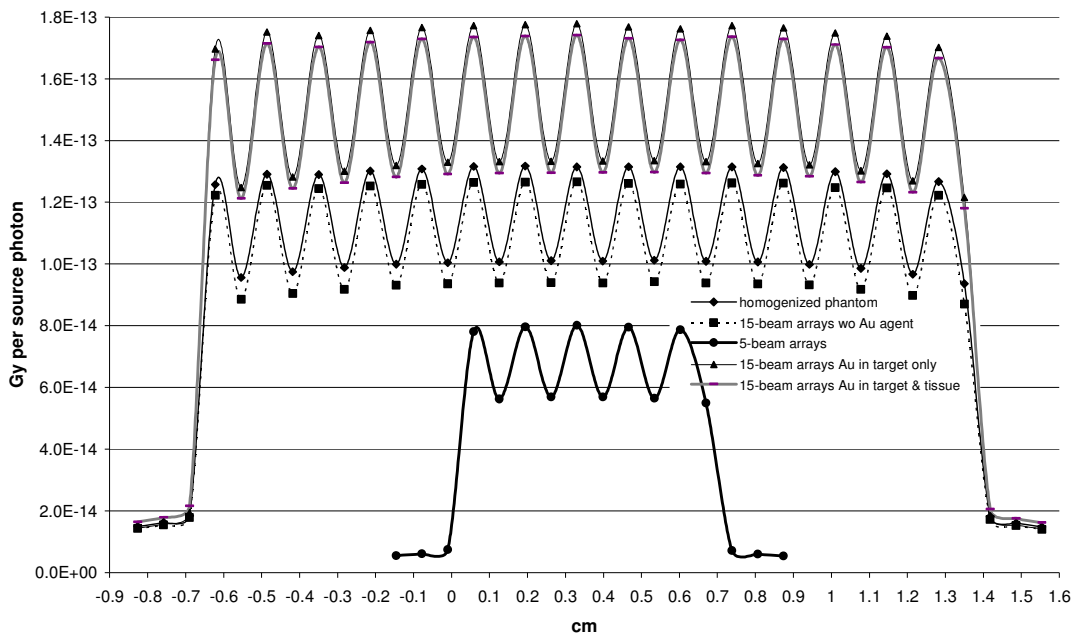


Figure 3.5. Lateral dose distributions averaged through the target region for all cases

3.5.3. Comparison of homogenized and realistic head phantoms

The depth-in-beam dose distributions for homogenized (case I) and Zubal (case II) phantoms are given in Figure 3.6. Relative errors at the distal side of the target are 1.6% for both cases.

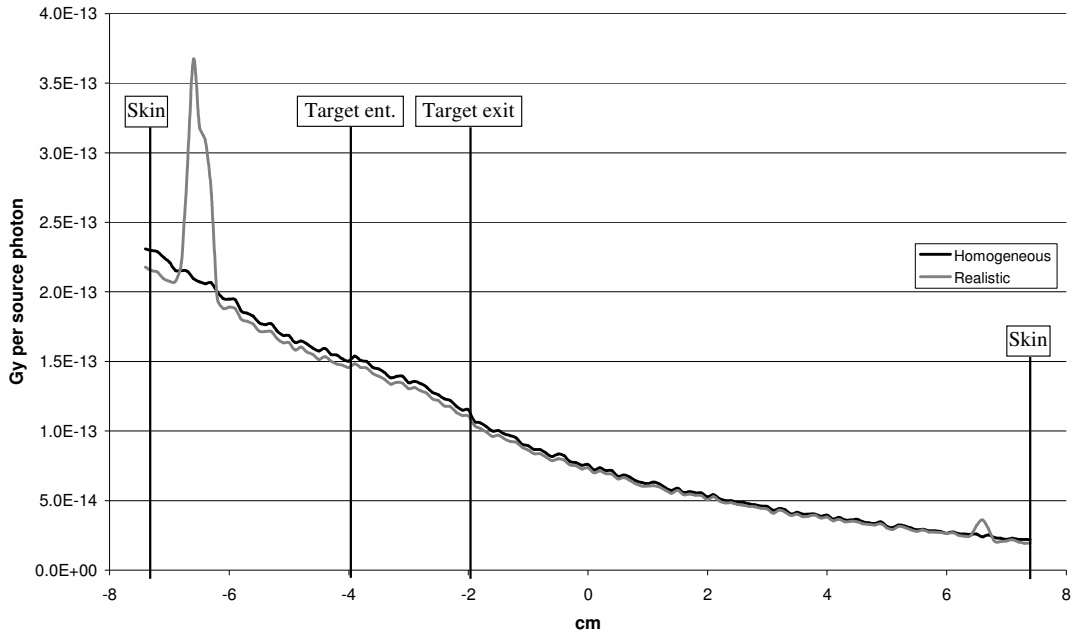


Figure 3.6. Depth-in-beam dose distributions for cases I and II

The absorbed dose in the entrance region is lower for case II than it is for case I. This is due to the adipose tissue with lower density between the skin and the skull bone in the Zubal phantom. Then there is a sudden increase in absorbed dose because of the skull bone. Furthermore, the dose curve for the Zubal phantom lies below the curve for the homogenized phantom in deeper regions, because the photon beam loses more energy in the skull bone.

The depth-valley dose distributions for cases I and II are given in Figure 3.7. Relative errors at the distal side of the target are 1.7% and 1.8% for cases I and II, respectively. A similar increment in dose is observed in the skull bone for the Zubal phantom, which is due to increased fluence of scattered secondary radiation between the beams in the bone. The curves in the target region (between $x = -2$ and $x = -4$) do not represent the valley doses but the in-beam doses for the beam array incoming from the top. The dose curve for case II lies below the curve for case I in this region, since the beams incoming from the top lose more energy in the skull bone as mentioned above.

The peaks in the curves, seen close to the far side of the head (between $x = 6$ and $x = 7$) in Figures 3.6 and 3.7 for case II, are due the skull bone at the other side of the head.

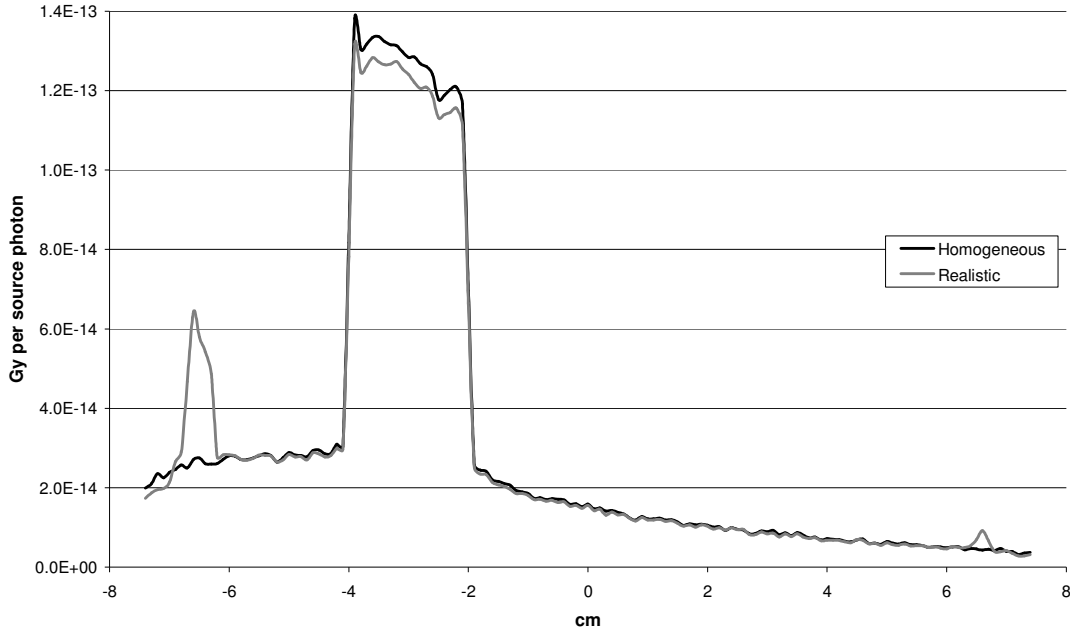


Figure 3.7. Depth – valley dose distributions for cases I and II

The ratios of skin entrance, maximum skull bone and maximum brain in-beam doses to target exit in-beam doses for cases I and II are given in Table 3.2.

Table 3.2. The ratios of skin entrance, maximum skull bone and maximum brain in-beam doses to target exit in-beam doses for case I and II

Ratios between	Case I	Case II
Skin entrance and target exit doses	2.01 ± 0.05	1.96 ± 0.05
Maximum skull bone doses and target exit doses	1.82 ± 0.05	3.30 ± 0.08
Maximum brain doses and target exit doses	1.69 ± 0.04	1.70 ± 0.05

PVDR distributions with respect to depth for cases I and II are given in Figure 3.8. Minimum PVDR values observed between the skin entrance and the target region are 5.0 ± 0.2 for cases I and II.

The PVDRs are close to 1 in the target region for both curves, since the homogenized unsegmented dose region was formed in this region.

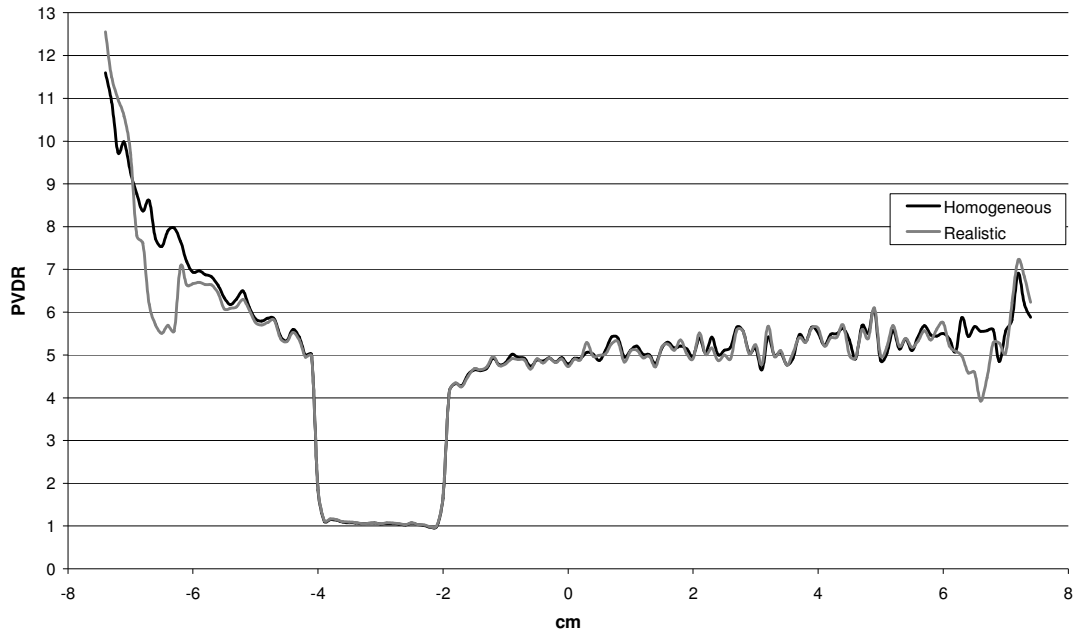


Figure 3.8. Depth – PVDR distributions for cases I and II

3.5.4. Effect of the number of microbeams: Comparison of 15- and 5-beam arrays

In-beam dose distributions with respect to depth for interlaced 15- (case II) and 5-beam arrays (case III) are given in Figure 3.9. Relative errors at the distal side of the target are 1.6% and 1.0% for cases I and II, respectively.

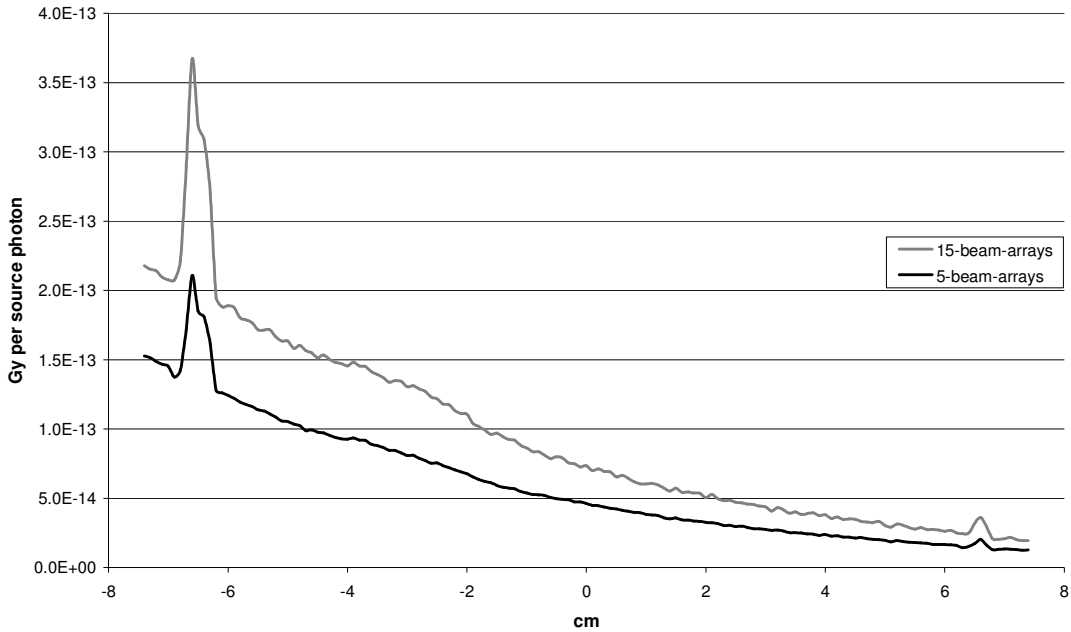


Figure 3.9. Depth – in-beam dose distributions for cases II and III

The ratios of skin entrance, maximum skull bone and maximum brain in-beam doses to target exit in-beam doses for cases II and III are given in Table 3.3.

Table 3.3. The ratios of skin entrance, maximum skull bone and maximum brain in-beam doses to target exit in-beam doses for cases II and III

Ratios between	Case II	Case III
Skin entrance and target exit doses	1.96 ± 0.05	2.21 ± 0.03
Maximum skull bone doses and target exit doses	3.30 ± 0.08	3.05 ± 0.04
Maximum brain doses and target exit doses	1.70 ± 0.05	1.80 ± 0.03

The depth–valley dose distributions for cases II and III are given in Figure 3.10. Relative errors at the distal side of the target are 1.8% and 1.0% for cases II and III, respectively.

Comparison of PVDR distributions with respect to depth for cases II and III are given in Figure 3.11. Minimum PVDR values between the skin entrance and target region for cases II and III are 5.0 ± 0.2 and 8.3 ± 0.3 , respectively.

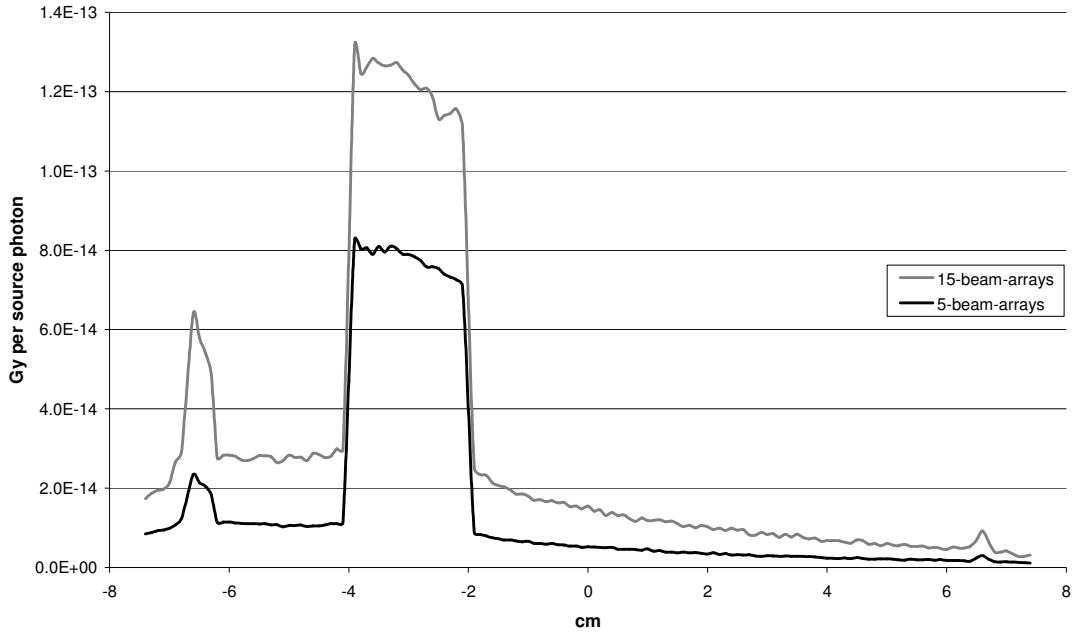


Figure 3.10. Depth – valley-dose distributions for cases II and III

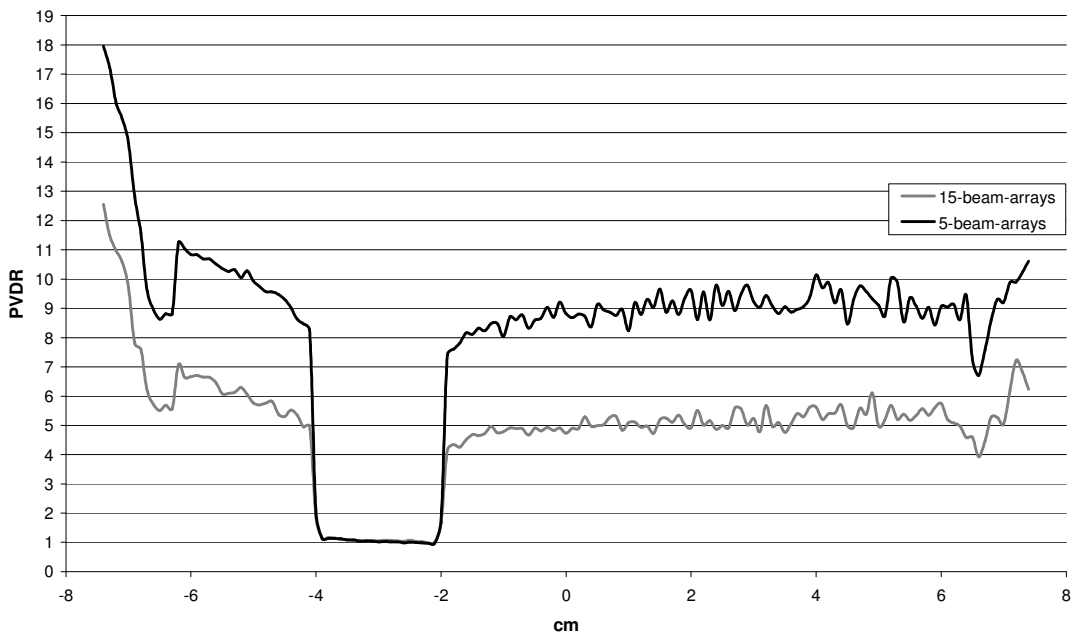


Figure 3.11. Depth – PVDR distributions for cases II and III

As seen from Figures 3.9, 3.10 and 3.11, the in-beam and valley doses increase with the number of beams; however PVDR values for 15-beam arrays are lower than the values for 5-beam arrays.

Lateral dose distributions, indicating dose falloffs at the edges of the target regions, for cases II and III are given in Figure 3.12. The values were normalized to in-beam dose value inside the target region for each case. Relative errors are less than 2.9% for cases II and III. 80–20% dose falloffs of $\sim 35\ \mu\text{m}$ and $\sim 13\ \mu\text{m}$ were obtained for cases II and III, respectively. The $35\ \mu\text{m}$ dose falloff width is consistent with that given by Dilmanian et al. (2006; 2008).

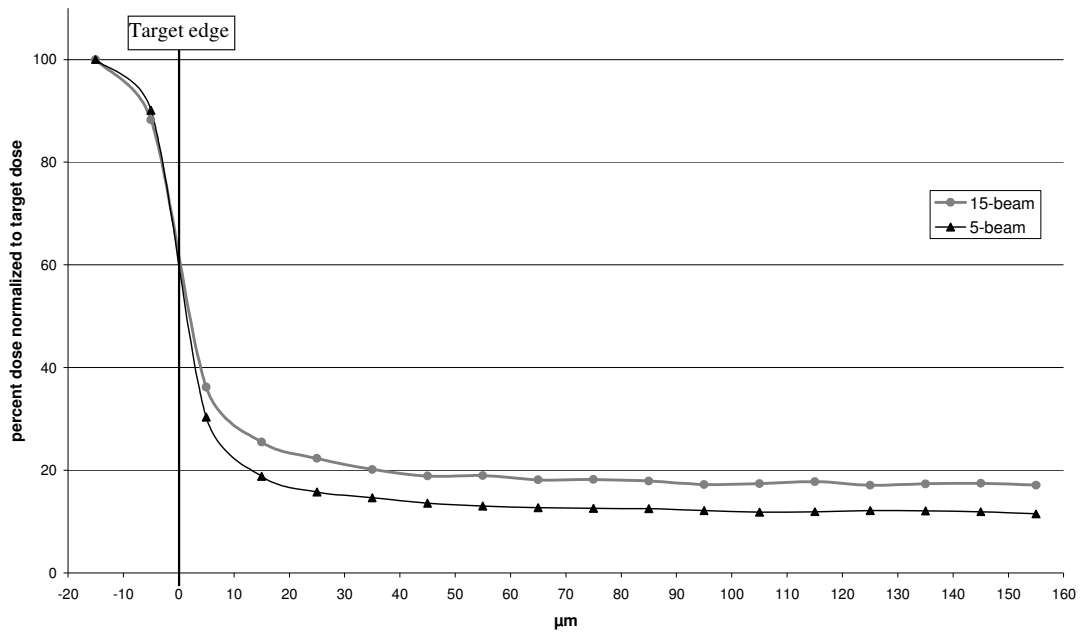


Figure 3.12. Lateral dose distribution at the edges of the targets for cases II and III

3.5.5. Effect of Au contrast agent

In-beam dose distributions with respect to depth for interlaced 15-beam arrays and for the cases without an Au contrast agent (case II), with an Au contrast agent in the target region only (case IV) and with an Au contrast agent in the target region and the surrounding tissue (case V) are given in Figure 3.13. Relative errors at the distal side of the target are 1.6% for all cases. The ratios of skin entrance, maximum skull bone and maximum brain in-beam doses to target exit in-beam doses for cases II, IV and V are given in Table 3.4.

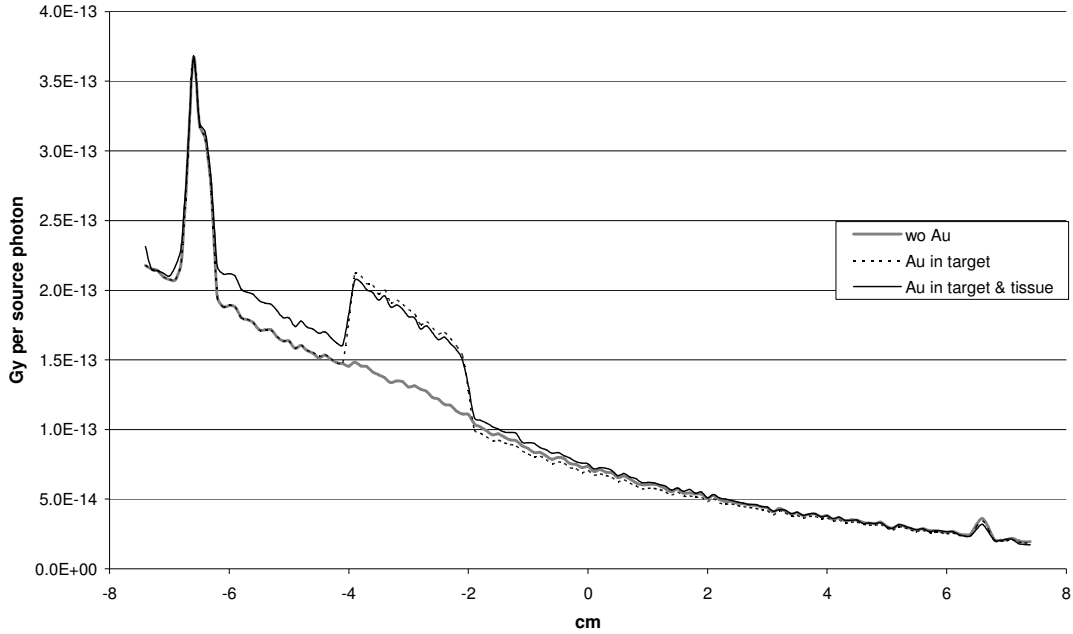


Figure 3.13. Depth-in-beam dose distributions for cases II, IV and V

Table 3.4. The ratios of skin entrance, maximum skull bone and maximum brain in-beam doses to target exit in-beam doses for cases II, IV and V

Ratios between	Case II	Case IV	Case V
Skin entrance and target exit doses	1.96 ± 0.05	1.42 ± 0.04	1.54 ± 0.04
Maximum skull bone doses and target exit doses	3.30 ± 0.08	2.40 ± 0.06	2.45 ± 0.06
Maximum brain doses and target exit doses	1.70 ± 0.05	1.24 ± 0.03	1.41 ± 0.04

Valley dose distributions with respect to depth for the cases II, IV and V are given in Figure 3.14. Relative errors at the distal side of the target are 1.8%, 1.7% and 1.8% for cases II, V and V, respectively.

PVDR distributions with respect to depth for cases II, IV and V are given in Figure 3.15. Minimum PVDR values between the skin entrance and the target region for cases II, IV and V are 5.0 ± 0.2 , 5.0 ± 0.2 and 4.6 ± 0.2 , respectively.

The dose enhancement due to administration of an Au contrast agent is clearly seen in in-target doses in Figures 3.13 and 3.14. The in-beam and valley dose values between the skin entrance and the target region are nearly the same for cases II and IV; however the dose absorbed in the same region is higher for case V. This is due to the Au concentration in the surrounding tissue.

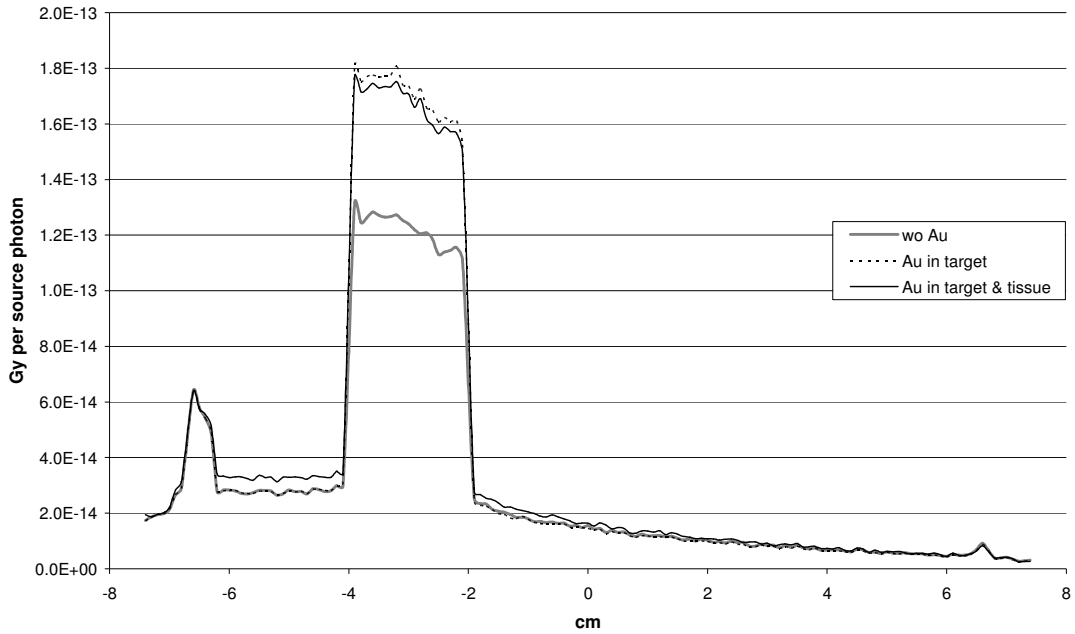


Figure 3.14. Depth–valley dose distributions for cases II, IV and V

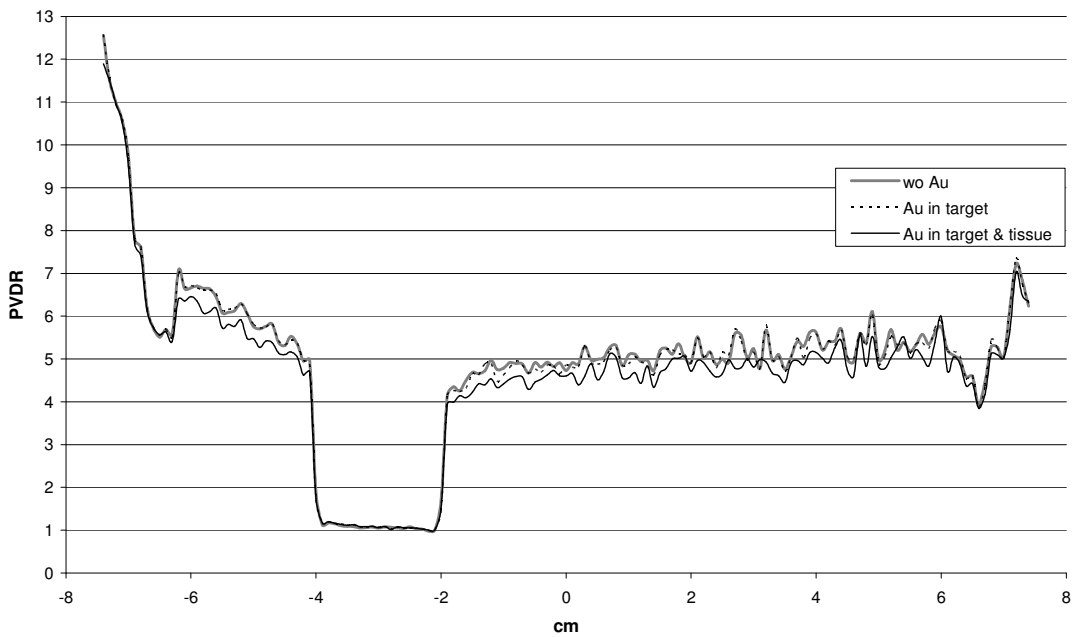


Figure 3.15. Depth–PVDR distributions for cases II, IV and V

Lateral dose distributions, indicating dose falloffs at the edges of the target regions, for cases II, IV and V are given in Figure 3.16. 80–20% dose falloffs of $\sim 35 \mu\text{m}$, $\sim 34 \mu\text{m}$ and $\sim 43 \mu\text{m}$ were observed for cases II, IV and V, respectively. Relative errors are less than 2.9 % for all cases.

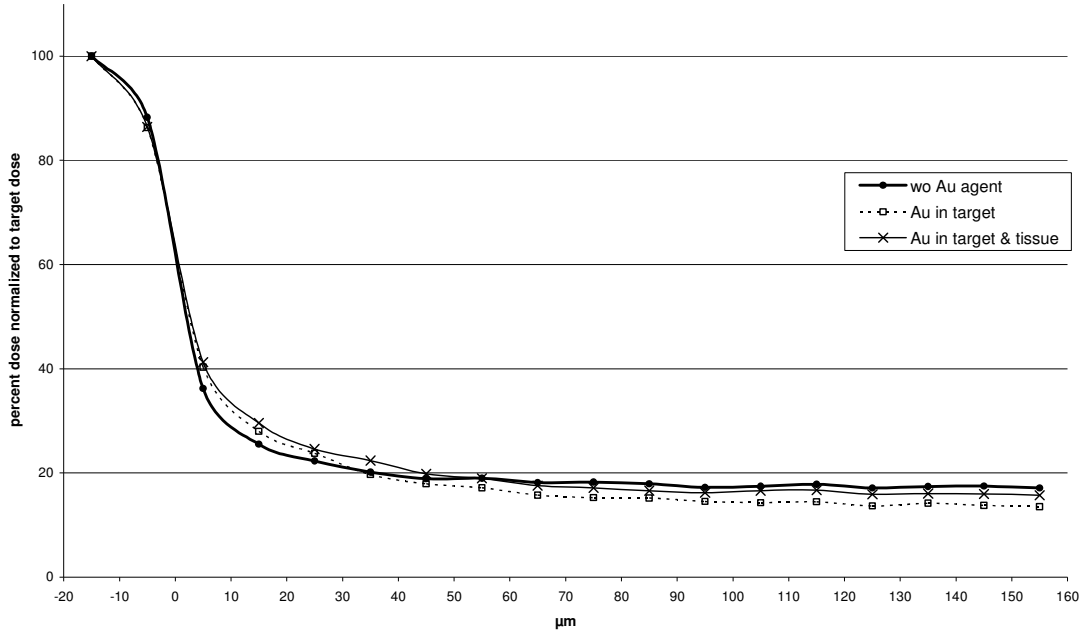


Figure 3.16. Lateral dose distribution at the edges of the targets for cases II, IV and V

3.6. Discussion

Both qualitative and quantitative information on transport of X-ray microbeams and dose distribution inside the detailed voxel-geometry head phantom were obtained in this study. It was observed that the parallel pattern of the microbeam arrays was preserved through the head phantom. This makes it possible to interlace microbeam arrays even at deep-seated targets.

The simulation results for the realistic head phantom were compared with the ones obtained with homogenized phantom. Actually the homogenized head phantom is even more realistic than water phantoms since it has the exact outer dimensions and shape of the head. The effect of the adipose tissue between the skin and the skull bone on dose distribution is discernible. A substantial increment in absorbed dose is observed in the skull bone due to higher density of the bone and potassium ($Z = 19$) and calcium ($Z = 20$) content as expected. The skull bone affects the dose distribution in deeper regions. The calculated dose distributions inside deep regions are close to each other for homogenized and realistic phantoms. However, the realistic phantom has the advantage that it can be used

to assess dose distributions in substantially inhomogeneous media like regions in close vicinity of the skull bone or cavities.

Similar dose falloff results were obtained with the mathematical models for a deep seated arget (Dilmanian et al. 2006; 2008).

In comparison of 15-beam (case II) and 5-beam-array (case III) cases, it was observed that as the dimensions of the target volume increase, the in-beam and valley doses increase. The energy deposition in the close vicinity of a beam and in the beam's path is mainly due to photoelectrons. However in distant regions energy is mainly deposited by Compton scattered photons and characteristic X-rays whose ranges are substantially longer than those of photoelectrons. This explains the decrease in PVDR in case II: the valley doses increase relatively more than the in-beam doses, since the valley doses are deposited mainly by Compton scattered photons and characteristic x-rays and the number of these photons increase with the number of beams. The increment of valley doses with the number of beams sets limits on the size and position of the target.

To study the effect of the AuNP contrast agent, 7 mg Au/g tumour and 2 mg Au/g tissue Au concentration values were used in the simulations, on the assumption that they would be applicable for humans (Cho, 2005). However, to our knowledge, there is no data available for Au nanoparticle deposition in tumours and healthy tissues in human or large animal brains in scientific literature yet.

In comparison of the case with an Au contrast agent in target region only (case IV) with the case without an Au agent (case II), minimum PVDR values between the skin entrance and the target region were found to be the same. However there is a substantial increase in the administered dose in the target region, where 7 mg Au/g tumour of Au is deposited. For the same dose value at the distal side of the tumour, the skin entrance, maximum skull bone and maximum brain doses were reduced to 0.73 ± 0.04 , 0.73 ± 0.03 and 0.73 ± 0.04 of those for case II, respectively. When there is also contrast agent deposition in surrounding tissue with 2 mg Au/g tumour composition (case V), a decrement was observed in PVDR values between the skin entrance and the target region compared to cases II and IV. For the same dose value at the distal side of the tumour, the skin entrance,

maximum skull bone and maximum brain doses were calculated as 0.79 ± 0.04 , 0.74 ± 0.03 and 0.83 ± 0.04 of those for case II, respectively.

4. EVALUATION OF THE USAGE OF A LINEAR ACCELERATOR AS THE X-RAY SOURCE FOR MICROBEAM RADIATION THERAPY

In this part the usage of a linear accelerator (linac) is evaluated as the radiation source for the stereotactic MRT technique (Dilmanian, 2009; 2010) with dosimetric Monte Carlo calculations.

The spectrum and angular distribution of the X-rays produced were calculated from the phase-space files which were formed with the Monte Carlo code BEAM-NRC (Rogers et al., 2007). The following dose distribution calculations were done with the Monte Carlo code MCNPX:

- Unidirectional single beams and beam arrays were simulated in a cylindrical water phantom to determine the optimum geometry of the beam arrays that are to be used in the stereotactic MRT.
- A pair of orthogonally interlaced beam arrays, analogous to the ones in the stereotactic MRT technique is simulated in a detailed head phantom to compare the depth – dose distributions with those calculated for the BIMRT technique (Dilmanian et al., 2008; Gokeri et al., 2010).
- Five orthogonally interlaced beam array pairs were simulated in a mathematical head phantom to analyze depth – dose distributions for the beam arrays and dose distribution in the target area.

4.1. The radiation Source and The Sampled X-ray Energies

Philips SL 25 linear accelerator was chosen as the X-ray source. The linac head and a cylindrical applicator (of length 40 cm) between the linac and a hypothetical multi-hole collimator (thickness of approximately 10 cm, made of tungsten) were modeled with the Monte Carlo code BEAM-NRC (Rogers et al., 2007). The X and Y jaws of the linac head were positioned so as to form an X-ray spot area of $10 \times 10 \text{ cm}^2$ at 100 cm distance from the source. The beam is transmitted from the linac head to the multi-hole collimator through the cylindrical lead collimator with an inner diameter of 3 cm. Angular distribution and energy spectrum of the linac-generated X-rays were calculated from the phase-space files which were formed at the applicator exit, in front of the multi-hole collimator, with the data processor

BEAMDP (Ma and Rogers, 2010). The electron contamination was not taken into account.

The calculated photon spectrum is given in Figure 4.1. The maximum and mean photon energies are 1.08 MeV and 2.07 MeV respectively. The angular distribution of the X-rays is given in Figure 4.2.

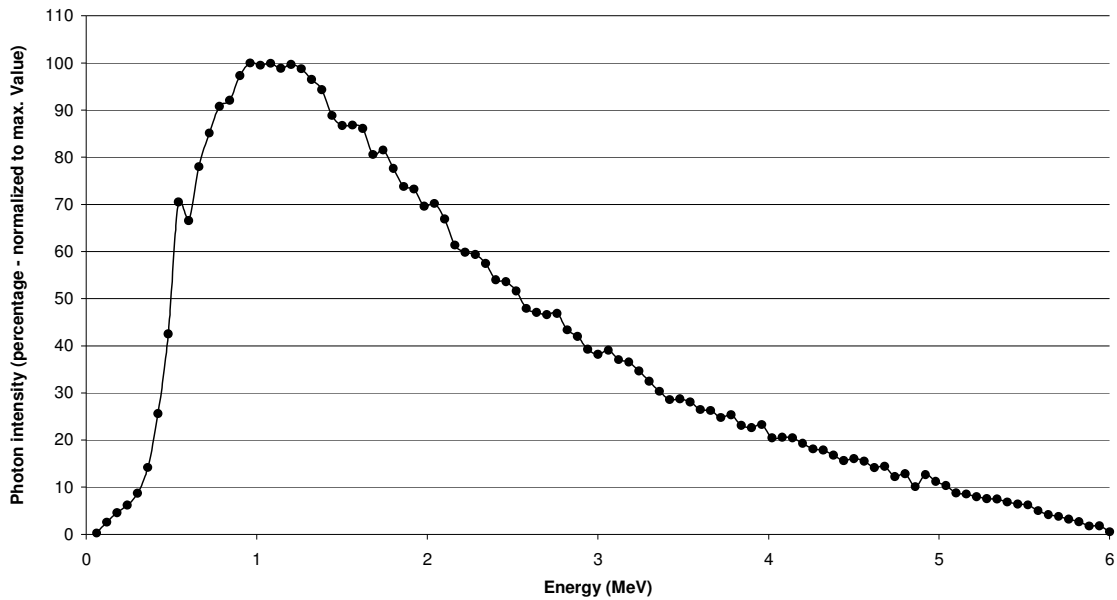


Figure 4.1. Spectrum of linac-generated X-rays

The photons in the beams were deemed to be highly mono-directional after traveling about 90cm source to multi-hole collimator distance and passing through the multi-hole collimator of about 10 cm thickness. Thus the beams were simulated mono-directionally after the multi-hole collimator from the calculated linac spectrum.

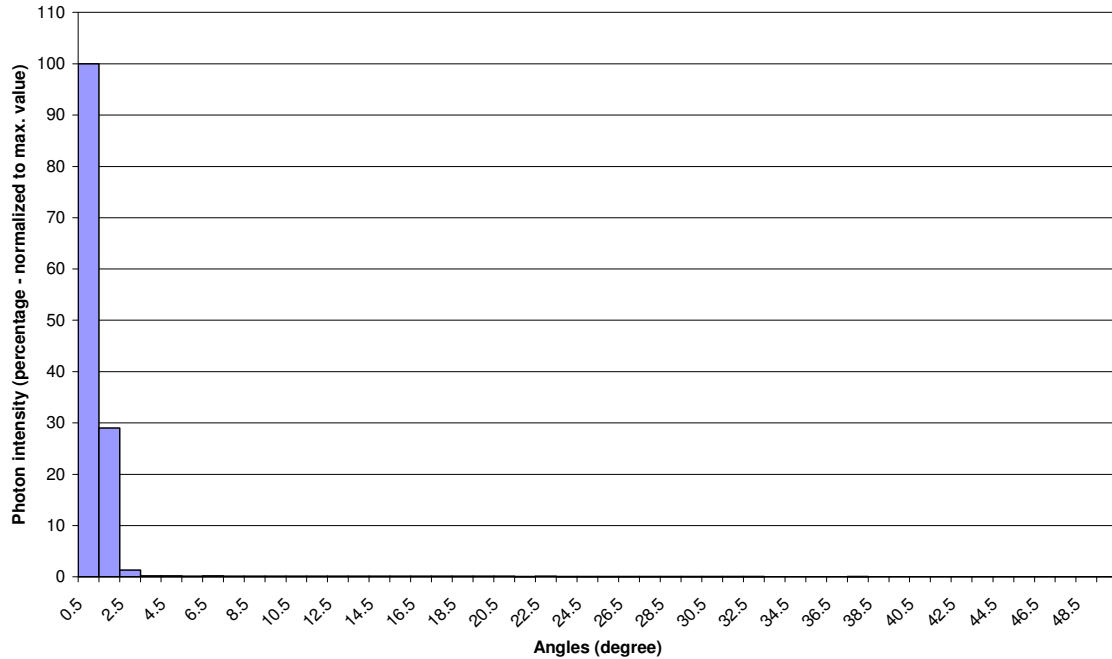


Figure 4.2. Angular distribution of linac-generated X-rays

In the simulations performed for synchrotron-generated X-rays, energies were sampled from the experimental ESRF spectrum (Siegbahn et al., 2005). The irradiation geometries are described in the following sections.

4.2. Dose Calculations for Single Unidirectional Beams in Cylindrical Water Phantom

Dose distributions for different beam energies, heights and thicknesses were calculated with MC simulations performed in a 16 x 16-cm cylindrical water phantom for single unidirectional beams to evaluate the effect of the beam energy and to decide on the geometry of beam arrays. Depth – dose profiles in beams' paths (depth – in-beam dose distribution) and dose fall-offs lateral to beams (between 3.5 and 5.5 cm depths) were calculated for the cases given in Table 4.1. Initial photon histories were selected as 1×10^7 for all simulations. Dimensions of the tallies used are given in Table 4.2.

Table 4.1. The cases for which depth – in-beam dose distributions and dose fall-offs are calculated

		Beam thickness (mm)	Beam height (mm)	Beam energy
Case I	Square pencil beam	0.5	0.5	0.5 MeV
Case II	Square pencil beam	0.5	0.5	1 MeV
Case III	Square pencil beam	0.5	0.5	Synchrotron spectrum
Case IV	Square pencil beam	0.5	0.5	linac spectrum
Case V	Planar beam	0.5	10	linac spectrum
Case VI	Planar beam	0.5	20	linac spectrum
Case VII	Planar beam	0.05	20	linac spectrum
Case VIII	Planar beam	0.1	20	linac spectrum

Table 4.2. Dimensions of the tallies used for calculating depth – in-beam dose distributions and dose fall-offs around the unidirectional beams for cases I – VIII

	Tally dimensions for in-beam doses	Tally dimensions for dose fall-offs
	Depth x width x height	Depth x width x height
Case I - IV	2 mm x 0.5 mm x 0.5 mm	2 cm x 20 μ m x 0.5 mm
Case V	2 mm x 0.5 mm x 10 mm	2 cm x 20 μ m x 10 mm
Case VI	2 mm x 0.5 mm x 20 mm	2 cm x 20 μ m x 20 mm
Case VII	2 mm x 50 μ m x 20 mm	2 cm x 20 μ m x 20 mm
Case VIII	2 mm x 0.1 mm x 20 mm	2 cm x 20 μ m x 20 mm

4.3. Dose Calculations for Unidirectional Beam Arrays inside Cylindrical Water Phantom

Beam arrays were formed to cover approximately $2 \times 2 \text{ cm}^2$ cross-sectional area of a hypothetical target, taking into account the results of the MC calculations of the eight cases mentioned above. Lateral dose distributions between 3.5 and 5.5 cm depths were analyzed for beam arrays constituted from planar (width = 0.5 mm, height = 20 mm, tallies of dimensions 2 cm x 50 μ m x 2 cm) and square pencil beams (width and height = 0.5 mm, tallies of dimensions 2 cm x 50 μ m x 0.5 mm) for the beam center-to-center (ctc) distances given in Table 4.3. Initial photon histories were selected as 1×10^7 for the simulations.

Table 4.3. The cases for which dose distributions lateral to the center beams in the arrays are analyzed

		ctc distance (mm)
Case IX	Square pencil beam array	2
Case X	Square pencil beam array	3
Case XI	Square pencil beam array	4
Case XII	Square pencil beam array	3.25
Case XIII	Planar beam array	4

4.4. Dose Calculations for Interlaced Orthogonal Beam Arrays inside Detailed Human Head Phantom

In the result of the analyses, beam arrays were decided to be formed from square pencil beams with 0.5 mm beam width and 3.25 mm center-to-center beam distance. Two orthogonally interlaced beam arrays, analogous to one of the five beam array pairs defined in Dilmanian's patents (2009; 2010), were simulated in the Zubal head phantom. The selected irradiation geometry given in Figure 4.3 is similar to those of Dilmanian et al's (2008) experimental study and the geometry used in Chapter 3. The dimensions of the target are 20 x 20 x 20 mm³. The target is located at 3 cm lateral to Cz in Figure 3.2, and 6 cm superior to the interauricular line.

Two-dimensional dose distribution in the target area was calculated with mesh tallies of dimensions 125 μm x 125 μm x 0.5 mm. Initial photon histories were selected as 3 x 10⁷ for the simulations. Instead of defining the peak doses as maximum doses in beams' paths and valley doses as minimum doses between the paths, mean in-beam and mean valley doses were calculated as a conservative approach. Depth – in-beam dose (through the path of the center beam) and depth – valley dose (beside the path of the center beam) distributions were calculated for irradiation from the side with mesh tallies of dimensions 1.1 mm x 0.5 mm x 0.5 mm and 1.1 mm x 2.75 mm x 0.5 mm respectively.

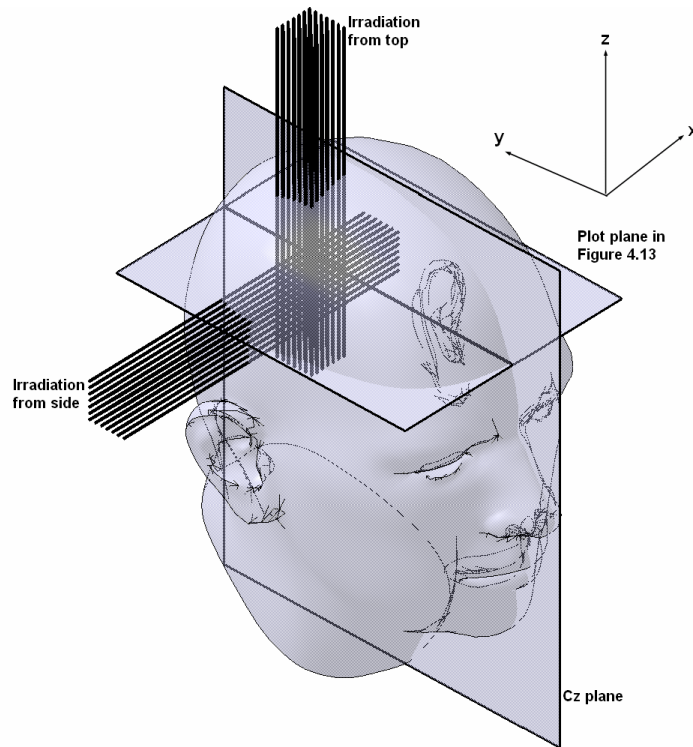


Figure 4.3. Irradiation geometry for two orthogonally interlaced beam array pairs

Simulations were performed for irradiation from the side and the top separately, which is analogous to irradiation from the side and the top with the same beam intensities and irradiation times. The tally results for irradiation from the side and the top were superimposed to obtain dose distribution for the interlaced beam arrays. Numbers of histories were selected as 1×10^7 for the simulation pairs.

The dose values calculated for irradiation from the top were multiplied with a multiplication factor to administer nearly the same amount of radiation dose in the target with both beam arrays. The multiplication factor of 1.13 ± 0.03 is the ratio of the energy deposition through the target, inside the path of the center beam in the array coming from the side to the energy deposition inside the path of the center beam in the array coming from the top. This is analogous to adjusting the irradiation times of the beam array pairs.

4.5. Dose Calculations for Five Orthogonally Interlaced Beam Array Pairs in a Mathematical Head Phantom

Nonsegmented dose region was not observed in the target region with the two orthogonally interlaced beam arrays as expected. Thus, an irradiation geometry

similar to the one proposed in Dilmanian's patents (2009; 2010) was modeled. Five orthogonally interlaced beam array pairs were simulated in a mathematical head phantom. The head phantom, which was taken from Orion et al's (2000) study, consists of an inner sphere with a diameter of 16 cm and a 0.6 mm thick skull region around the brain.

The cylindrical beam arrays aimed at the phantom's center consist of square pencil beams with the same beam thickness and beam intervals as the ones simulated in the previous part. The beam arrays cover the cylindrical cross-sectional area of the spherical target with a diameter of approximately 2 cm. The irradiation geometry is given in Figure 4.4. The cylindrical beam arrays were illustrated as rectangular prisms to show that the beam array pairs are orthogonal and aligned in the same planes to be interlaced. The positioning of the linac is given in Table 4.4. Two types of beam array patterns were simulated for the beam array pairs. The patterns for A- and B-type beam arrays are given in Figure 4.5.

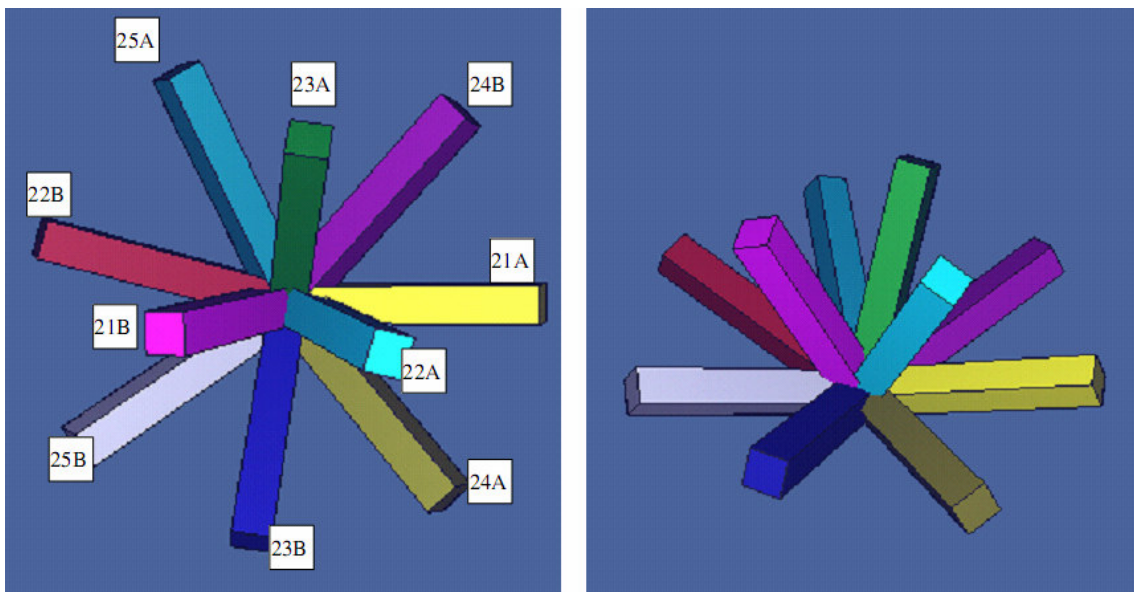


Figure 4.4. Irradiation geometry for five orthogonally interlaced beam array pairs

Table 4.4. Positioning of linac for irradiation with five orthogonally beam array pairs

Beam Arrays	Polar Angle θ (degrees)	Azimuthal Angle ϕ
21A	67.5	0.0
21B	23.8	200.4
22A	22.8	330.1
22B	68.1	167.1
23A	30.2	82.1
23B	59.8	262.8
24A	67.8	310.2
24B	70.5	48.5
25A	67.9	117.0
25B	68.1	216.4

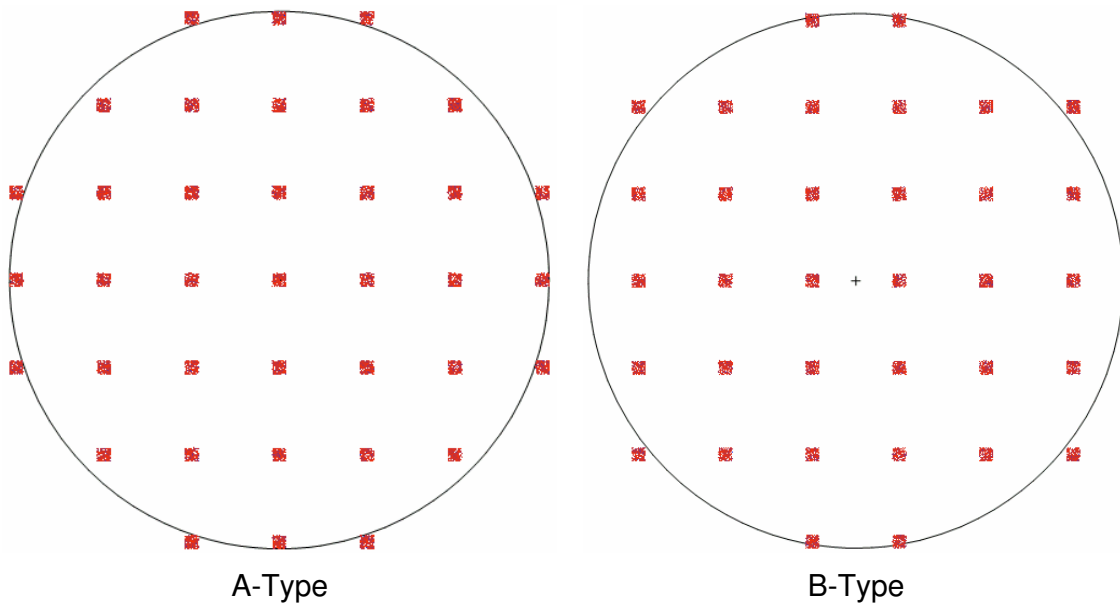


Figure 4.5. Patterns of A- and B-type beam arrays

Depth – in-beam dose (through the path of center beam) and depth – valley dose (beside the path of the center beam) distributions were calculated for the beam

arrays 21A and 22A. In-beam and valley doses were calculated with mesh tallies of dimensions 1.1 mm x 0.5 mm x 0.5 mm and 1.1 mm x 2.75 mm x 0.5 mm respectively.

Two-dimensional dose distribution in and around the target region was calculated with mesh tallies of dimensions 125 μm x 125 μm x 0.5 cm.

The ten beam arrays were simulated separately and the tally results were superimposed to calculate the dose distributions. Initial photon histories were selected as 1×10^7 for each beam array.

4.6. Results

4.6.1. Dependence of dose distributions on beam energies

The depth – in-beam dose distributions for 500 keV and 1 MeV mono-energetic beams and beams with synchrotron and linac spectrums are given in Figure 4.6.

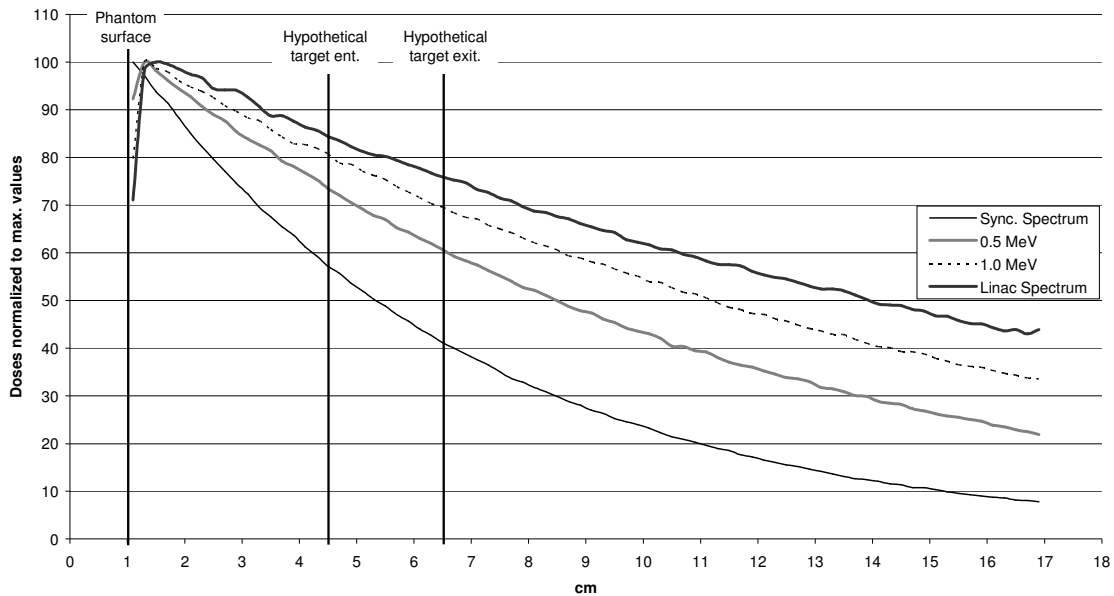


Figure 4.6. Depth – in-beam dose distributions for different beam energies (beam thickness = 0.5 mm, square pencil beam)

In all calculations beam heights and beam widths were selected as 0.5 mm (square beams). The curves were normalized to their maximum values. Relative errors at the distance of 6.5 cm (depth of 5.5 cm) which corresponds to the depth for the distal side of the hypothetical target are less than 0.43%. The most

penetrative beam is produced by linac as expected. The synchrotron-generated beam has the fastest dose decrease with depth.

The lateral dose distributions averaged over 3.5 – 5.5 cm depths for the mentioned beam energies are given in Figure 4.7. The curves were normalized to their maximum values. The relative errors are less than 5.2% at the distances which correspond to 1% of the respective maximum doses. The steep lateral dose fall-off beside a beam's path is a desired feature since it results in low valley doses when the beams are gathered together to form a beam array. The fastest dose fall-off is observed for the synchrotron-generated beam. The dose fall-off characteristics of the 1 MeV and linac-generated beams are similar.

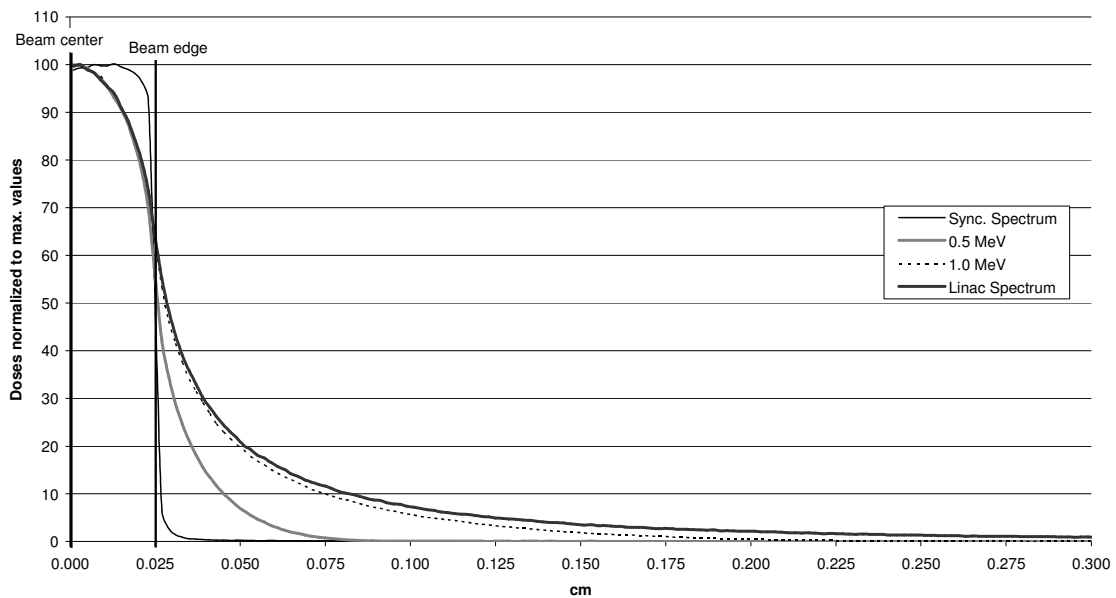


Figure 4.7. Dose distributions lateral to single beams for different beam energies (beam thickness = 0.5 mm, square pencil beam)

4.6.2. Dependence of dose distributions on beam heights

The depth – in-beam dose distributions for beam heights of 0.5, 10 and 20 mm are given in Figure 4.8. In all simulations beam widths were selected as 0.5 mm and beam energies were sampled from the linac spectrum. The curves were normalized to their maximum values. Relative errors at the distal side of the hypothetical target are less than 0.43%. The dose distributions for the 10 mm and 20 mm-high beams are similar: Dose buildup is observed in the depth of approximately 1 cm and the normalized dose values are nearly same throughout

the phantom. However, this dose buildup is not observed for the 0.5 mm-high beam and the dose values are lower in the deeper regions of the phantom.

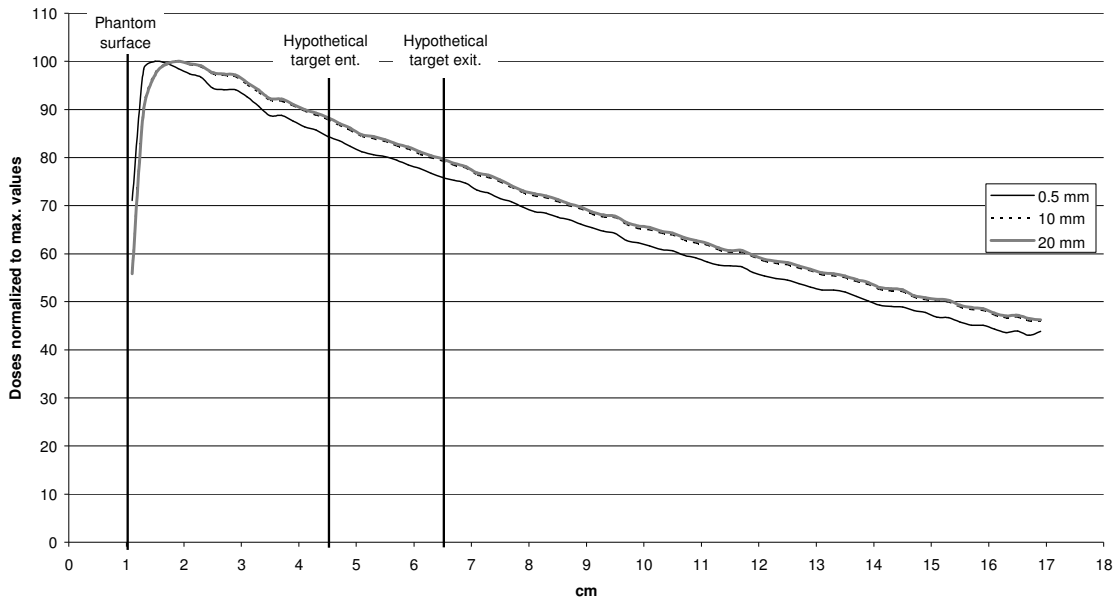


Figure 4.8. Depth – in-beam dose distributions for different beam heights (beam thickness = 0.5 mm, linac spectrum)

The lateral dose distributions averaged over 3.5 – 5.5 cm depths for the mentioned beam heights are given in Figure 4.9. The curves were normalized to their maximum values.

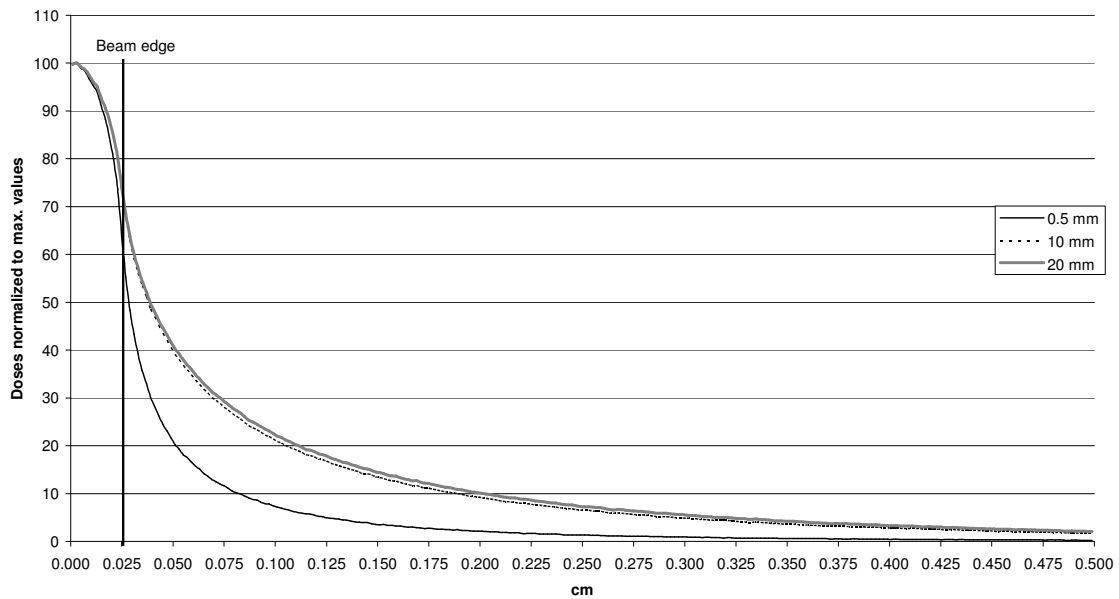


Figure 4.9. Dose distributions lateral to single beams between 3.5 – 5.5 cm depths for different beam heights (beam thickness = 0.5 mm, linac spectrum)

The relative errors are less than 3.3% at the distances which correspond to 1% of the respective doses for the beam with 0.5 mm height. The relative errors for the other beam thicknesses are less than 1.7% in the range that is taken into consideration. The dose fall-off characteristics of beams with 10 and 20 mm heights (planar beams) are similar. However 0.5 mm-high-beam results in the steepest dose fall-off curve, which is desired.

4.6.3. Dependence of dose distributions on beam thicknesses

The depth – in-beam dose distributions for beam thicknesses of 0.05, 0.1 and 0.5 mm are given in Figure 4.10. In all simulations beam heights were selected as 20 mm and beam energies were sampled from the linac spectrum. The curves were normalized to their maximum values. Relative errors at the distal side of the hypothetical target are less than 0.58%. The depth – in-beam dose distributions are similar for all beam thicknesses.

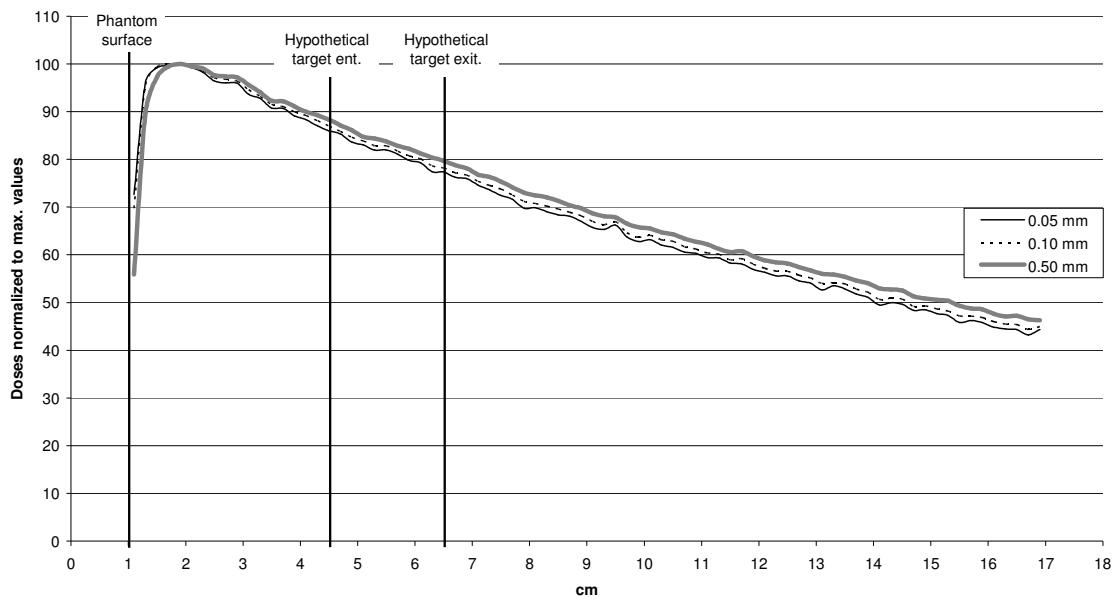


Figure 4.10. Depth – in-beam dose distributions for different beam thicknesses (beam height = 20 mm, linac spectrum)

The lateral dose distributions averaged over 3.5 – 5.5 cm depths for the mentioned beam thicknesses are given in Figure 4.11. The curves were normalized to their maximum values. The relative errors are less than 1.5% in the range that is taken into consideration. The beams with 0.05 mm and 0.1 mm thicknesses results in steeper dose fall-off curve than the beam with 0.5 mm thickness. However, the 0.5

mm-wide-beam was evaluated as being appropriate for use, since it covers more cross-sectional area in the target and is easier to be produced with a linac and a multi-hole collimator.

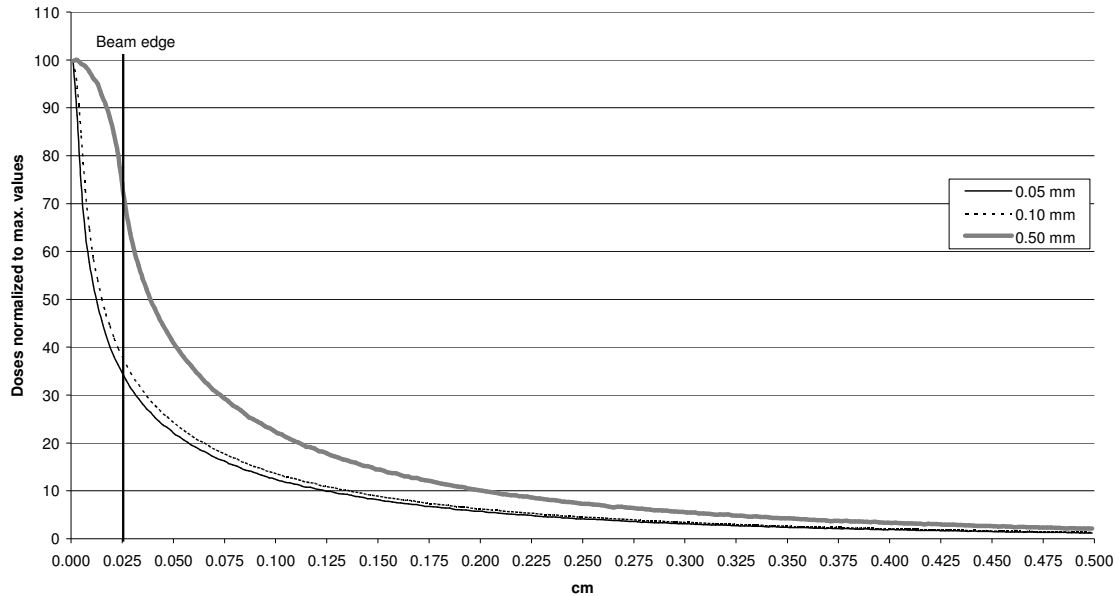


Figure 4.11. Dose distributions lateral to single beams between 3.5 – 5.5 cm depths for different beam thicknesses (beam height = 20 mm, linac spectrum)

4.6.4. Dependence of dose distributions on center-to-center distances for planar and square pencil beam arrays

Dose distributions lateral to center beams averaged over 3.5 – 5.5 cm depths for the cases given in Table 4.3 are given in Figure 4.12.

The curves were normalized to their maximum values. The relative errors are less than 4.8% for the minimum dose values in the respective curves. The valley doses administered by the planar beam array are higher than those for the square pencil beam array with the same beam interval. The valley doses increase as the beams approach each other as expected. The required beam intervals are evaluated taking into account the PVDRs. A PVDR value of approximately 5, similar to the one that had been obtained before the target region with the synchrotron-generated X-rays (Dilmanian et al., 2008; Gokeri et al., 2010), is aimed to be achieved. As many beams as possible are desired to be used in the unidirectional beam array to cover approximately the cross-sectional area of the hypothetical target ($2 \times 2 \text{ cm}^2$). Calculated PVDRs for the studied cases are given in Table 4.3.

Beam arrays were decided to be formed from square pencil beams with 0.5 mm beam width and 3.25 mm center-to-center distance.

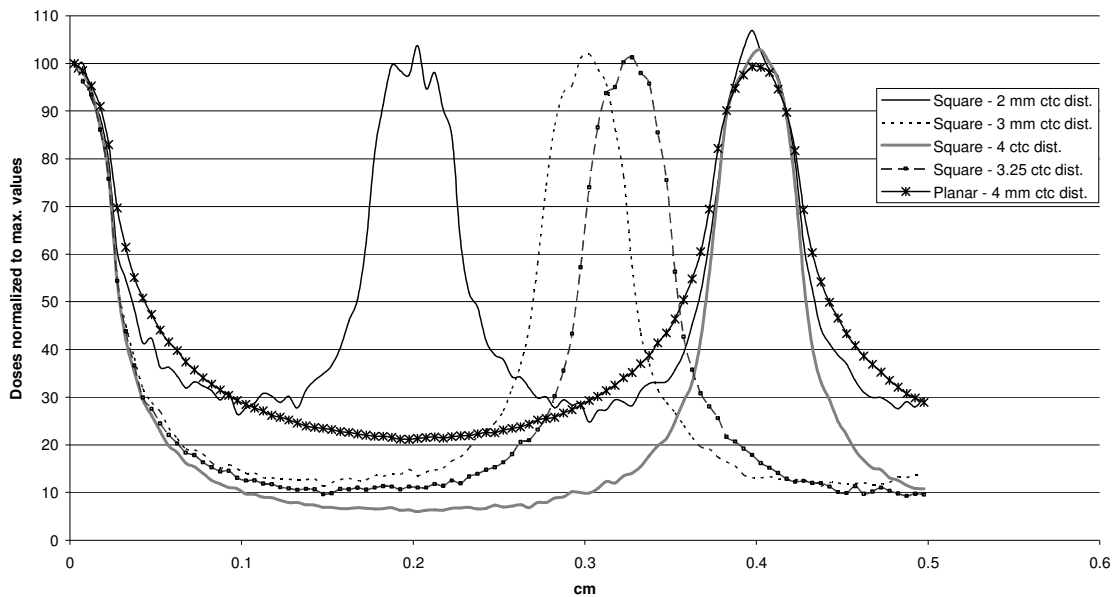


Figure 4.12. Dose distributions lateral to center beams between 3.5 – 5.5 cm depths for different beam ctc distances, planar and square beams (linac spectrum)

4.6.5. Two-dimensional dose distributions through the realistic head phantom and in the target region for orthogonally interlaced beam arrays

Two-dimensional dose distributions through the realistic (Zubal) head phantom and in the target region are given as contour plots in Figures 4.13 and 4.14 respectively. The absorbed dose values were normalized to maximum dose values. The plot plane is indicated in Figure 4.3. In Figure 4.13, relative errors at the distal side of the target are below 5% in the beams' paths and 10% between the beams' paths. These errors are adequate for assessment for radiation transport in two dimensions. Parallel pattern of the beams is preserved through the phantom. In Figure 4.14, the in-beam and valley doses for the interlaced beam arrays are clearly observed. The relative errors are lower than approximately 15% in the beams' paths. An unsegmented dose region could not be formed in the target region.

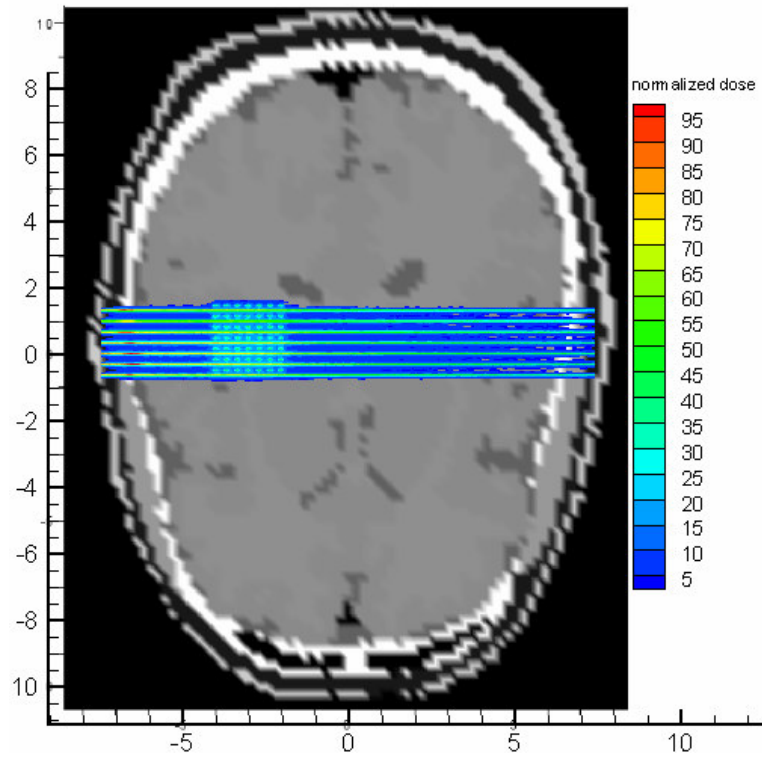


Figure 4.13. Two-dimensional dose distribution through the detailed head phantom for irradiation with two orthogonally interlaced beam arrays

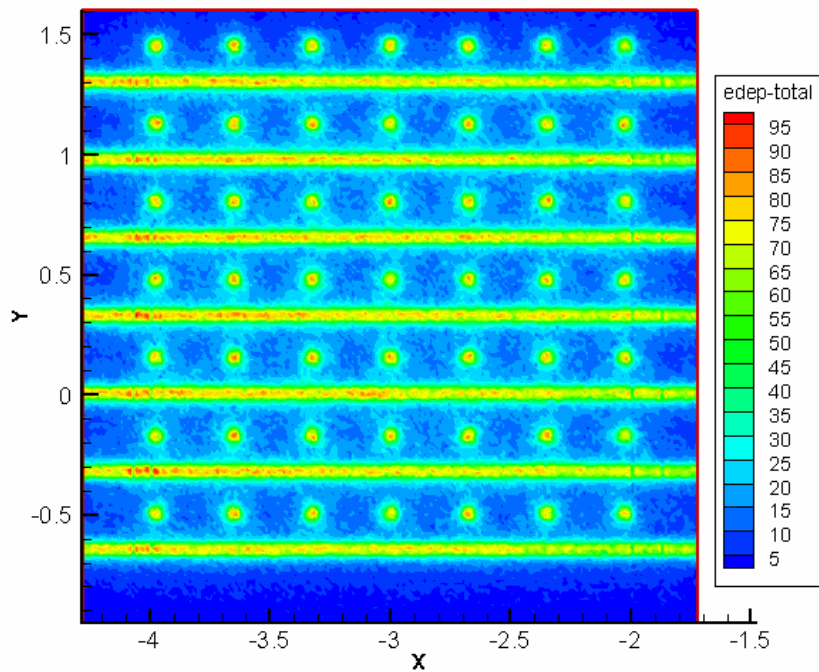


Figure 4.14. Two-dimensional dose distribution in the target area for irradiation with two orthogonally interlaced beam arrays

4.6.6. Depth – dose and depth – PVDR distributions through the realistic head phantom for orthogonally interlaced beam arrays

Depth – in-beam and depth – valley dose distributions for the center beam in the array that comes from the side, through the phantom are given in Figure 4.15 with the dose distributions which had been calculated for the BIMRT technique in the Chapter 3.

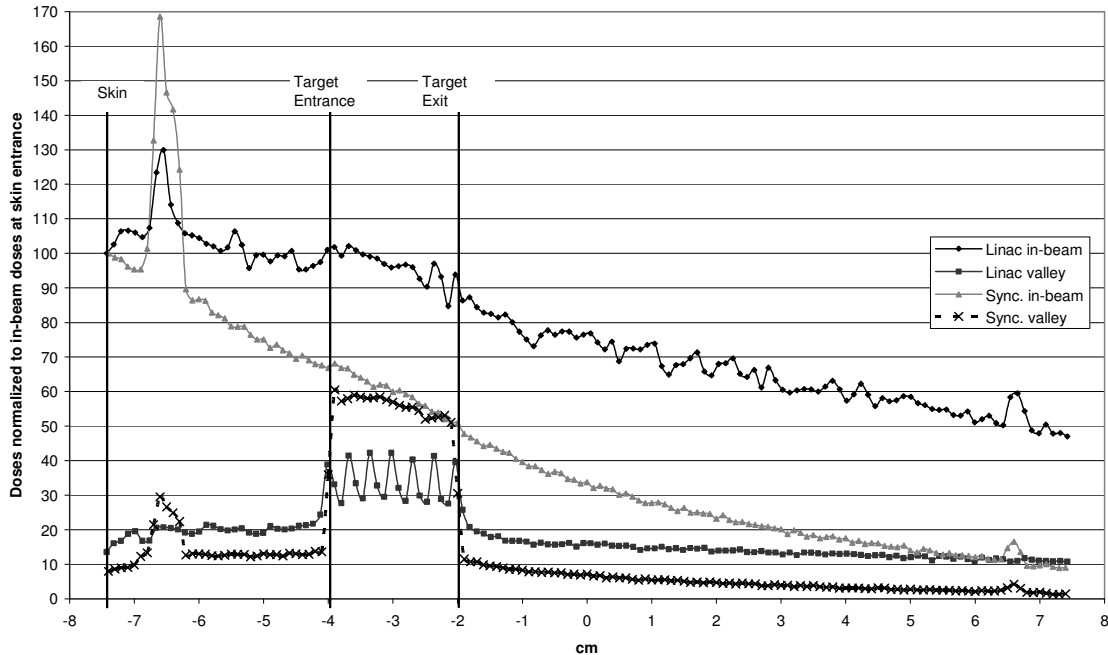


Figure 4.15. Depth – in-beam and valley dose distributions for two orthogonally interlaced linac and synchrotron-generated beam arrays

The curves in Figure 4.15 were normalized to the respective in-beam skin entrance dose values. For linac-generated beam arrays, relative errors at the distal side of the target are below 3.3% in the beams' paths and 4.1% between the beams' paths. The depth – PVDR distributions are given in Figure 4.16. Relative errors are less than 7.4% at the distal side of the target.

The linac-generated beams seem to be more penetrative than the synchrotron-generated ones as expected. Lower doses are administered in the skull bone for the linac spectrum. The valley doses are higher and the PVDRs are lower in the region between the skin entrance and the target except in the skull bone for linac-generated beams than those calculated for synchrotron-generated beams. However PVDR values around 5 were calculated for the selected beam interval. In

Figure 4.15 the curves in the target region (between $x = -2$ and $x = -4$) do not represent the valley doses because of the in-beam doses administered by the beam array coming from the top. Furthermore, the mesh sizes are not appropriate for calculating in-beam and valley doses for irradiation from the top. Thus the curves in Figures 4.15 and 4.16 shouldn't be taken into consideration for the mentioned region.

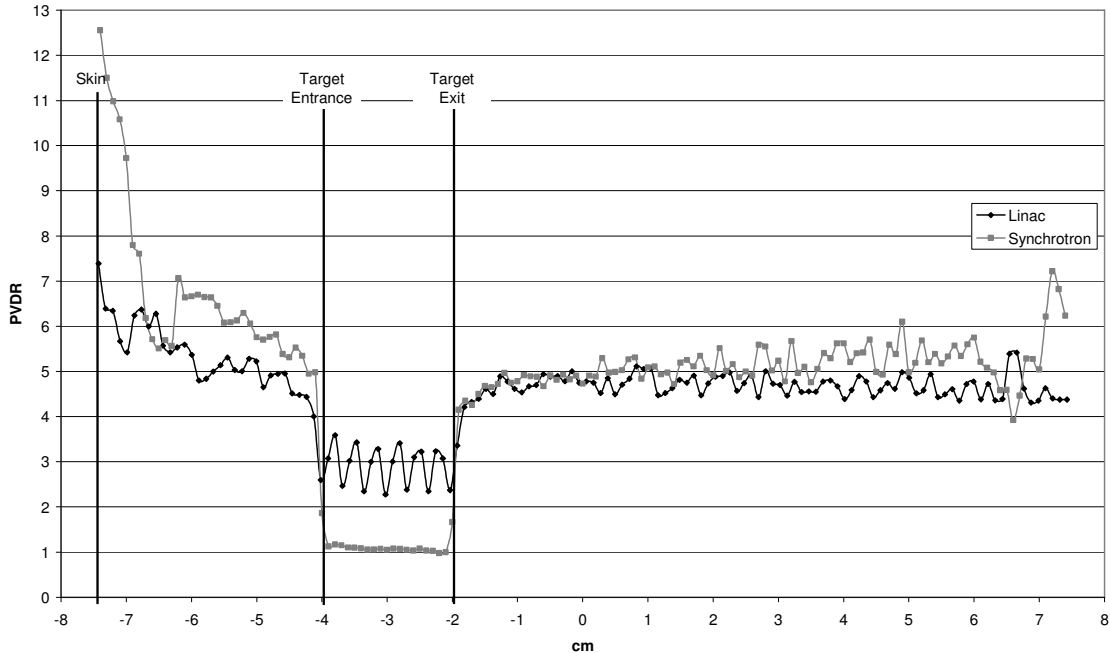


Figure 4.16. Depth – PVDR distributions for two orthogonally interlaced linac and synchrotron-generated beam arrays

The curves for the synchrotron generated X-rays are smoother than those for the linac-generated ones. The wiggles in the curves for the linac-generated pencil beam arrays are due to the fact that energy is deposited through interactions along particle tracks; the ranges of secondary electrons scattered by high-energy photons are larger than those scattered by synchrotron-generated X-rays. Furthermore, the dimensions of mesh tallies used for the pencil beams are smaller than the ones used for the planar beams. Thus, some meshes may contain few tracks while others contain many.

The ratios of skin entrance, maximum skull bone and maximum brain in-beam doses to target exit in-beam doses for linac-generated and synchrotron-generated beams are given in Table 4.5.

Table 4.5. The ratios of skin entrance, maximum skull bone and maximum brain in-beam doses to target exit in-beam doses for interlaced linac-generated and synchrotron-generated beam arrays

Ratios between	Linac-generated beams	Synchrotron-generated beams
Skin entrance and target exit doses	1.16 ± 0.06	2.01 ± 0.05
Maximum skull bone doses and target exit doses	1.50 ± 0.08	1.82 ± 0.05
Maximum brain doses and target exit doses	1.21 ± 0.07	1.69 ± 0.04

4.6.7. Two-dimensional dose distribution in and around the target region for five orthogonally interlaced beam array pairs

The two-dimensional dose distribution in and around the target region is given in Figure 4.17 as a contour plot. The values were normalized to the maximum value. The outer surface of the target region is shown with a circle (with radius of approximately 1 cm).

The relative errors are between 5.5% and 7.5% in the target region. An unsegmented dose region was formed in the target, however, the sharp dose fall-off (in the order of ten micrometers) obtained in BIMRT technique is not observed. The 80% to 20% dose fall-off distance, beside the target region, is between 5 – 8 mm.

4.6.8. Depth – dose and depth – PVDR distributions through the mathematical head phantom for five orthogonally interlaced beam array pairs

Depth – in-beam and depth – valley dose distributions for the center beams in the arrays 21A and 22A are given in Figure 4.18. Relative errors are less than 4.7% and 2.9% for in-beam and valley doses for both beam arrays.

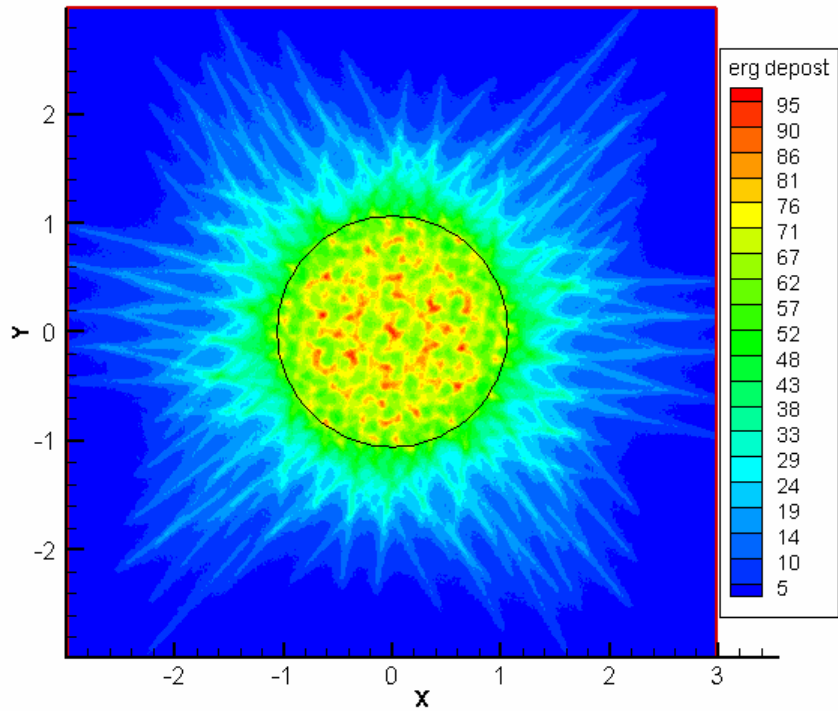


Figure 4.17. Two-dimensional dose distribution in and around the target region for irradiation with five orthogonally interlaced beam array pairs

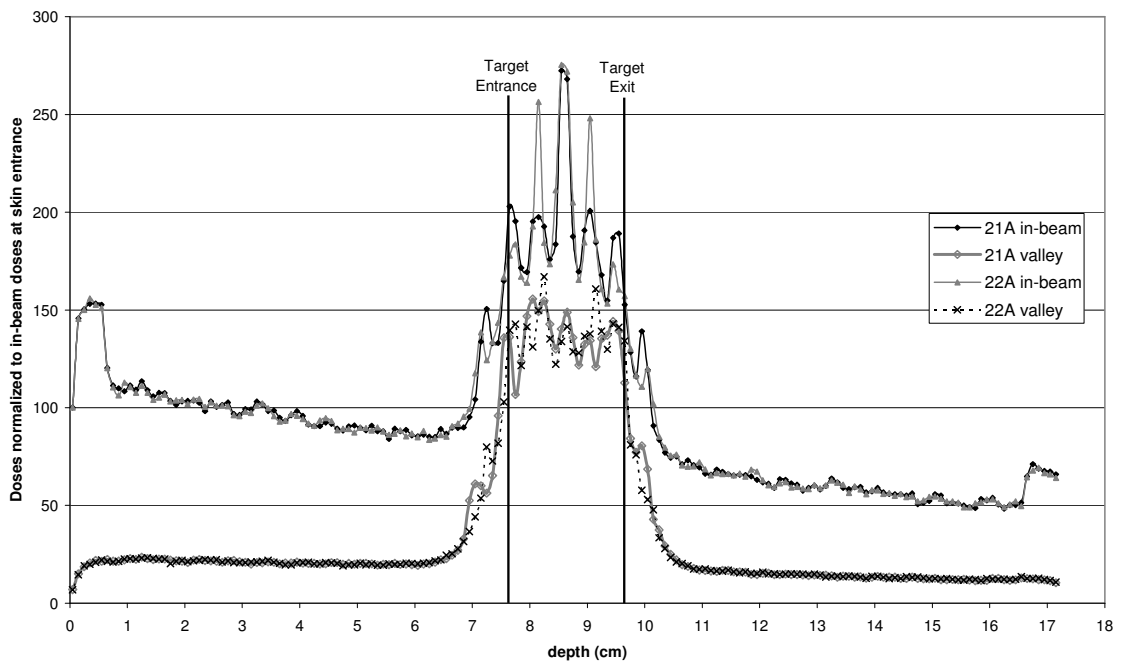


Figure 4.18. Depth – in-beam and depth – valley dose distributions in the arrays 21A and 22A for irradiation with five orthogonally interlaced beam array pairs

The depth – PVDR distributions are given in Figure 4.19. Relative errors are less than 7.5%. PVDR values of approximately 1 are observed in the target area. Thus, a homogeneous dose region is formed. Similar dose distributions are observed for both beam arrays. The in-beam and valley doses begin to increase 10 mm before reaching the target. This is in accordance with the dose fall-off distance observed in the two-dimensional dose distribution.

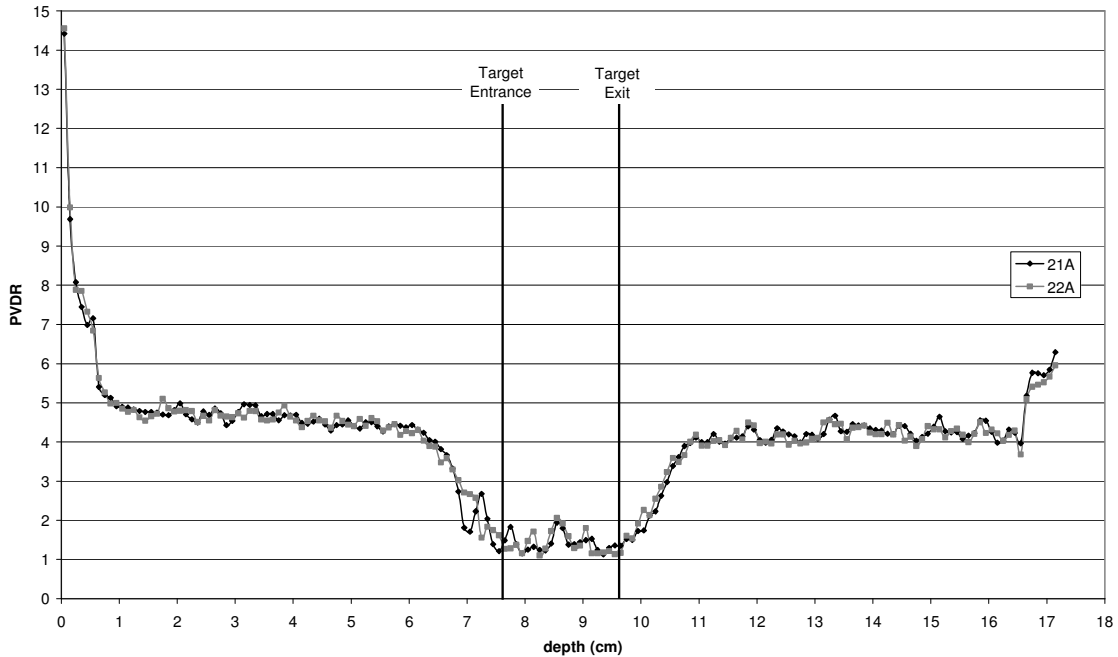


Figure 4.19. Depth – PVDR distributions in the arrays 21A and 22A for irradiation with five orthogonally interlaced beam array pairs

4.7 Discussion

The shape of the beams and geometry of the beam arrays that are to be interlaced in the realistic head phantom were decided on according to the results of calculations performed with the cylindrical water phantom. The valley doses deposited between the beams' paths were observed to be lower for arrays of square pencil beams than for arrays of planar beams. Thus arrays of pencil beams are more convenient for such X-ray energies.

For two orthogonally interlaced beam arrays, the linac-generated beams were observed to be more penetrative than the synchrotron-generated ones, which is a desired feature, since it provides substantial decrease in the skin entrance,

maximum skull bone and maximum brain doses which are administered inevitably to produce the desired target dose. This is due to the decrease in mass attenuation coefficient for the media with increasing photon energy.

The parallel pattern of the linac-generated beam arrays was preserved through the phantom and PVDR values are nearly constant in the regions deeper than the target. The calculated PVDR values are still close to 5, which was obtained in Dilmanian et al's (2008) experimental study (semi-quantitative) and in Chapter 3 (Gurdal et al., 2010). However, an unsegmented dose region was not observed in the target. The energy deposited due to secondary radiation, scattered from the beams' paths, was not enough to fill the low dose regions between the paths of the interlacing beam arrays.

An irradiation geometry which was claimed to be used to form an unsegmented dose region (Dilmanian et al., 2009; 2010) was simulated. The unsegmented dose region could be formed in the center of a mathematical head phantom. However, the dose fall-off distance beside the target area was comparable with those for conventional radiotherapy. Besides, the PVDRs in the beam array paths were lower than those calculated for the BIMRT technique. Thus sparing of the healthy tissues is not expected to be provided with linac as the X-ray source and the irradiation geometry that uses five orthogonally interlaced beam array pairs as the BIMRT technique.

5. CONCLUSION

In the first part of the study (section 2) MCNPX and the cross-section libraries used were shown to be suitable for micrometric dosimetry calculations and low X-ray energies.

In the second part (section 3) a realistic head phantom that was created from MRI images of a human head was used in dosimetric MC calculations for the X-ray microbeam therapy technique. The usability of voxel-geometry phantoms for dosimetry of BIMRT has been shown. Difference between the dose distributions for the homogenized and the realistic phantoms was observed.

Dose falloffs calculated for the case without an Au contrast agent is consistent with the values which are given in the literature. Furthermore, the in-beam and valley doses (hence PVDR) were consistent with the semi-quantitative results of Dilmanian et al.'s (2008) experimental study with an anthropomorphic head phantom.

It was observed that the usage of gold as a contrast agent provided a substantial increase in target dose and decreases the maximum skin, skull bone and brain doses, inevitable to produce the desired target dose. In cases with an Au contrast agent in the target region or with an Au contrast agent in target and surrounding tissue, the dose falloff widths were still small. The Au contrast agent deposited in surrounding tissue increases the valley doses between the skin entrance and the target. However, the PVDR values was still close to the ones observed for the BIMRT technique.

In the third part (section 4) a linear accelerator was evaluated as an X-ray source for the stereotactic MRT technique. An unsegmented dose region was formed at the center of a spherical head phantom with an irradiation geometry which was proposed in Dilmanian's patents (2009; 2010). However, the dose fall-off distance beside the target area was comparable with those for conventional radiotherapy and the PVDRs in the beam array paths were lower than those calculated for the BIMRT technique. The advantages of the MRT technique may not be preserved with the usage of linac as the X-ray source. However, current clinical data confirms

the value of spatially fractionated (GRID) therapy (Peñagaricano et al., 2009) in the management of large volume of disease with an acceptable toxicity profile.

BIBLIOGRAPHY

- Attix F H 1986 Introduction to Radiological Physics and Radiation Dosimetry, John Wiley & Sons, New York
- Anschel D J, Romanelli P, Benveniste H, Foerster B, Kalef-Ezra J, Zhong Z and Dilmanian F A 2007 Evolution of afocal brain lesion produced by interlaced microplanar x-rays *Minim. Invasive Neurosurg.* 50 43–6
- Bransden B H and Joachain C J 1983 Physics of atoms and molecules, Longman, New York.
- Cho S H 2005 Estimation of tumour dose enhancement due to gold nanoparticles during typical radiation treatments: a preliminary Monte Carlo study *Phys. Med. Biol.* 50 N163–73
- Compton A H and Allison S K 1935 X-rays in Theory and Experiment, D. Van Nostrand, New York.
- Crosbie J C et al 2010 Tumor cell response to synchrotron microbeam radiation therapy differs markedly from cells in normal tissues *Int. J. Radiation Oncology Biol. Phys.* 77 886-94
- Curtis H J 1967 The use of a deuteron microbeam for simulating the biological effects of heavy cosmic-ray particles *Radiat. Res. Suppl.* 7 250–7
- Davies H, Bethe H A and Maximon L C 1954 Theory of bremsstrahlung and pair production. II. Integral cross sections for pair production *Phys. Rev.* 93 788
- De Felici M, Felici R, Sanchez del Rio M, Ferrero C, Bacarian T and Dilmanian F A 2005 Dose distributions from x-ray microbeam arrays applied to radiation therapy: an EGS4 Monte Carlo study *Med. Phys.* 32 2455–63
- Dilmanian F A 2005 X-ray microbeams: tumor therapy and central nervous system research *Nucl. Instrum. Methods Phys. Res. A* 548 30–7
- Dilmanian F A 2007 Methods for implementing microbeam radiation therapy US Patent No. 7,194,063 B2
- Dilmanian F A 2009 Method and device for performing stereotactic microbeam radiation therapy US Patent 2009 /0093863A1
- Dilmanian F A 2010 Method and device for performing stereotactic microbeam radiation therapy Patent No. US 7643610 B2
- Dilmanian F A et al 2001 Response of avian embryonic brain to spatially segmented x-ray microbeams *Cell. Mol. Biol. (Noisy-le-grand)* 47 485–93
- Dilmanian F A et al 2002 Response of the rat intracranial 9L gliosarcoma to microbeam radiation therapy *Neuro Oncol.* 4 26–38
- Dilmanian FA, Qu Y, Feinendegen L E, Pena LA, Bacarian T, Henn FA, Kalef-Ezra J, Liu S, Zhong Z and McDonald J W 2007 Tissue-sparing effect of x-ray microplanar beams particularly in the CNS: is a bystander effect involved? *Exp. Hematol.* 35 69–77
- Dilmanian F A, Romanelli P, Zhong Z, Wang R, Wagshul M E, Kalef-Ezra J, Maryanski M J, Rosen E M and Anschel D J 2008 Microbeam radiation therapy: tissue dose

- penetration and BANG-gel dosimetry of thick-beams' array interlacing Eur. J. Radiol. 68S S129–36
- Dilmanian F A, Zhong Z, Bacarian T, Benveniste H, Romanelli P, Wang R, Welwart J, Yuasa T, Rosen E M and Ansel D J 2006 Interlaced x-ray microplanar beams: a radiosurgery approach with clinical potential PNAS 103 9709–14
- Dvorak H F 1990 Leaky tumor vessels: consequences for tumor stroma generation and for solid tumor therapy Prog. Clin. Biol. Res. 354 A 317–30
- Evans J F, Blue T E and Gupta N 2001 Absorbed dose estimates to structures of the brain and head using a high-resolution voxel-based head phantom Med. Phys. 28 780–6
- Evans R D 1955 The Atomic Nucleus, McGraw-Hill, New York
- Fermi E 1940 The ionisation loss of energy in gases and in condensed materials Phys. Rev. 57 485–93
- Gokeri G, Kocar C and Tombakoglu M 2010 Monte Carlo simulation of microbeam radiation therapy with an interlaced irradiation geometry and an Au contrast agent in a realistic head phantom Phys. Med. Biol. 55 7469–87
- Hainfeld J F, Dilmanian F A, Zhong Z, Slatkin D N, Kalef-Ezra J A and Smilowitz H M 2010 Gold nanoparticles enhance the radiation therapy of a murine squamous cell carcinoma Phys. Med. Biol. 55 3045–59
- Hainfeld J F, Slatkin D N and Smilowitz H M 2004 The use of gold nanoparticles to enhance radiotherapy in mice Phys. Med. Biol. 49 N309–15
- Hainfeld J F, Slatkin D N, Focella T M and Smilowitz H M 2006 Gold nanoparticles: a new x-ray contrast agent Br. J. Radiol. 79 248–53
- ICRU 1970 Report 16: Linear Energy Transfer, ICRU, Bethesda, MD
- ICRU 1984a Report 37: Stopping Powers for Electrons and Positrons, ICRU, Bethesda, MD
- ICRU 1984b Report 35: Radiation Dosimetry; Electron Beams with Energies Between 1 and 50 MeV, ICRU, Bethesda, MD
- James WD, Hirsch L R, West J L, O'Neal P D and Payne J D 2007 Application of INAA to the build-up and clearance of gold nanoshells in clinical studies in mice J. Radioanal. Nucl. Chem. 271 455–9
- Klein O and Nishina Y 1929 Über die Streuung von Strahlung durch freie Elektronen nach der neuen relativistischen Quantendynamik von Dirac Z. Phys. 52 853–68
- Koch H W and Motz J W 1959 Bremsstrahlung cross-section formulas and related data Rev. Mod. Phys. 31 920–55
- Laissue J A et al 1999 Microbeam radiation therapy Proc. SPIE 3770 38–45
- Laissue J A et al 2001 The weanling piglet cerebellum: a surrogate for tolerance to MRT (microbeam radiation therapy) in pediatric neuro-oncology Proc. SPIE 4508 65–73
- Laissue J A, Blattmann H, Wagner H P, Grotzer MA and Slatkin D N 2007 Prospects for microbeam radiation therapy of brain tumours in children to reduce neurological sequelae Dev. Med. Child. Neurol. 49 577–81

- Laissue JA et al 1998 Neuropathology of ablation of rat gliosarcomas and contiguous-brain tissues using a microplanar beam of synchrotron-wiggler-generated x-rays *Int. J. Cancer* 78 654–60
- Martinez-Rovira I, Sempau J, Fernandez-Varea J M, Bravin A and Prezado Y 2010 Monte Carlo dosimetry for forthcoming clinical trials in x-ray microbeam radiation therapy *Phys. Med. Biol.* 55 4375–88
- Mayles P, Nahum A and Rosenwald J C 2007 *Handbook of Radiotherapy Physics Theory and Practice*, Taylor and Francis, New York
- Mayol R and Salvat F 1997 Total and transport cross sections for elastic scattering of electrons by atoms *Atom. Data Nucl. Data Tables* 65 55–154
- Meredith W J and Massey J B 1977 *Fundamental Physics of Radiology* 3rd ed. JohnWright and Sons, Bristol
- McMahon S J, Mendhall M H, Jain S and Currell F 2008 Radiotherapy in the presence of contrast agents: a general figure of merit and its application to gold nanoparticles *Phys. Med. Biol.* 53 5635–51
- Møller C 1932 Zur Theorie des Durchgangs schneller Elektron durch Materie *Ann. Phys.* 14 531–85
- Motz J W, Olsen H A and Koch H W 1969 Pair production by photons *Rev. Mod. Phys.* 41 581–639
- Nahum A E 1985 The MDAH pencil-beam algorithm, in *The Computation of Dose Distributions in Electron Beam Radiotherapy*, Medical Physics Publishing, Madison
- Orion I, Rosenfeld A B, Dilmanian F A, Telang F, Ren B and Namito Y 2000 Monte Carlo simulation of dose distributions from a synchrotron-produced microplanar beam array using the EGS4 code system *Phys. Med. Biol.* 45 2497–508
- Pelowitz D B 2005 *MCNPX User's Manual Version 2.5.0*, Los Alamos National Laboratory Report LA-CP-05-0369
- Peñaricán J A et al. 2009 Spatially fractionated (GRID) therapy for large and bulky tumors *J Ark Med Soc* 105(11) 263–65
- Prezado Y, Fois G, Le Duc G and Bravin A 2009a Gadolinium dose enhancement studies in microbeam radiation therapy *Med. Phys.* 36 3568–74
- Prezado Y, Renier M and Bravin A 2009b A new method of creating minibeam patterns for synchrotron radiation therapy: a feasibility study *J. Synchrotron Radiat.* 16 582–6
- Prezado Y, Renier M and Bravin A 2009c X-ray energy optimization in minibeam radiation therapy *Med. Phys.* 36 4897–902
- Regnard P et al 2008a Irradiation of intracerebral 9L gliosarcoma by a single array of microplanar x-ray beams from a synchrotron: balance between curing and sparing *Phys. Med. Biol.* 53 861–78
- Regnard P, Bräuer-Krisch E, Troprès I, Keyriläinen J, Bravin A and Le Duc G 2008b Enhancement of survival of 9L gliosarcoma bearing rats following intracerebral delivery of drugs in combination with microbeam radiation therapy *Eur. J. Radiol.* 68S 151–5

- Roeske J C, Nunez L, Hoggarth M, Labay E and Weichselbaum R R 2007 Characterization of the theoretical radiation dose enhancement from nanoparticles *Technol. Cancer. Res. Treat.* 6 395–401
- Rogers D W O, Walters B and Kawrakow I 2007 BEAMnrc Users Manual, Ionizing Radiation Standards, National Research Council of Canada
- Salvat F, Fernández-Varea J M and Sempau J 2003 PENELOPE, a Code System for Monte Carlo Simulation of Electron and Photon Transport, OECD Nuclear Energy Agency, Issy Les-Moulineaux
- Sauter F 1931 Über den atomaren Photoeffekt in der K-Schale nach der relativistischen Wellenmechanik *Diracs Ann. Physik* 11 454–88
- Serduc R et al 2006 In vivo two-photon microscopy study of short-term effects of microbeam irradiation on normal mouse brain microvasculature *Int. J. Radiat. Oncol. Biol. Phys.* 64 1519–27
- Serduc R et al 2008a Characterization and quantification of cerebral edema induced by synchrotron x-ray microbeam radiation therapy *Phys. Med. Biol.* 53 1153–66
- Serduc R et al 2008b Brain tumor vessel response to synchrotron microbeam radiation therapy: a short-term in vivo study *Phys. Med. Biol.* 53 3609–22
- Siegbahn E A 2007 Dosimetry for Synchrotron X-ray Microbeam Radiation Therapy PhD Thesis, European Synchrotron Radiation Facility, France
- Siegbahn E A, Bräuer-Krisch E, Stepanek J, Blattmann H, Laissue J A and Bravin A 2005 Dosimetric studies of microbeam radiation therapy (MRT) with Monte Carlo simulations *Nucl. Instrum. Methods Phys. Res. A* 548 54–8
- Slatkin D N, Spanne P O, Dilmanian F A, Gebbers J O and Laissue J A 1995 Subacute neuropathological effects of microplanar beams of x-rays from a synchrotron wiggler *Proc. Natl. Acad. Sci. USA* 92 8783–7
- Slatkin D N, Spanne P, Dilmanian F A and Sandborg 1992 Microbeam radiation therapy *Med. Phys.* 19 1395–400
- Spiga J, Siegbahn E A, Bräuer-Krisch E, Randaccio P and Bravin A 2006 Microdosimetry for microbeam radiation therapy (MRT): theoretical calculations using the Monte Carlo toolkit, IEEE Nuclear Science Symp. Conf. Record, San Diego, CA.
- Spiga J, Siegbahn E A, Bräuer-Krisch E, Randaccio P and Bravin A 2007 Geant4 simulations for microbeam radiation therapy (MRT) dosimetry, IEEE Nuclear Science Symp. Conf. Record, Honolulu, HI.
- Stepanek J, Blattmann H, Laissue J A, Lyubimova N, DiMichiel M and Slatkin D N 2000 Physics study of microbeam radiation therapy with PSI-version of Monte Carlo code GEANT as a new computational tool *Med. Phys.* 27 1664–75
- Sternheimer R M 1961 in *Methods of Experimental Physics* Yuan L C and Wu C S Eds. Vol. 5A, Academic Press, New York.
- Straille W E and Chase H B 1963 The use of elongate microbeams of x-rays for simulating the effects of cosmic rays on tissues: a study of wound healing and hair follicle regeneration *Radiat. Res.* 18 65–75
- Tsai Y S 1974 Pair production and bremsstrahlung of charged leptons *Rev. Mod. Phys.* 46 815

- Turner J E 2007 *Atoms, Radiation, and Radiation Protection*, WILEY-VCH Verlag GmbH & Co. KGaA, Weinheim.
- Unezaki S, Maruyama K, Hosoda J-I, Nagae I, Koyanagi Y, Nakata M, Ishida O, Iwatsuru M and Tsuchiya S 1996 Direct measurement of the extravasation of polyethyleneglycol-coated liposomes into solid tumor tissue by in vivo fluorescence microscopy *Int. J. Pharm.* 144 11–7
- Zubal I G, Harrell C R, Smith E O and Smith A L 1995 Two dedicated software, voxel-based, anthropomorphic (torso and head) phantoms *Proc. Int. Workshop on Voxel Phantom Development (National Radiological Protection Board, Chilton, UK, 6–7 July 1995)*
- Zubal I G, Harrell C R, Smith E O, Rattner Z, Gindi G and Hoffer P B 1994a Computerized three-dimensional segmented human anatomy *Med. Phys.* 21 299–302
- Zubal I G, Harrell C R, Smith E O, Smith A L and Krischlunas P 1994b High resolution, MRI-based, segmented, computerized head phantom *The Zubal Phantom Data, Voxel-Based Anthropomorphic Phantoms* <http://noodle.med.yale.edu/phantom>

RESUME

Name Surname : Gürdal Gökeri

Place of Birth : İzmir, Turkey

Date of Birth : September 7, 1978

Marital Status : Married

Education and Academic Positions:

2005 – 2012 Hacettepe University Department of Nuclear Engineering (PhD)

2002 – 2005 Hacettepe University Department of Nuclear Engineering (MSc)

1996 – 2002 Hacettepe University Department of Nuclear Engineering (BS)

Language: English

Professional Experience:

2006 – Turkish Atomic Energy Authority, Ankara, Engineer.

2002 – 2006 H.U. Nuclear Engineering Dept., Ankara, Research Assistant

Publications and Presentations:

Gokeri G, Kocar C and Tombakoglu M 2010 Monte Carlo simulation of microbeam radiation therapy with an interlaced irradiation geometry and an Au contrast agent in a realistic head phantom *Phys. Med. Biol.* **55** 7469–87

Gokeri G, Kocar C and Tombakoglu M 2010 'Modeling and Simulation of Microbeam Radiation Therapy with Monte Carlo Technique Using Voxel-Geometry-Phantoms' presented at European Nuclear Conference, Spain, 30 May – 2 June

Gokeri G, Erturk E, Kocar C and Tombakoglu M 2009 'Monte Carlo Calculation of Dose Distributions for Two Kinds of Ophthalmic Plaques' presented at Medical Physics Congress, Ankara, 22 – 24 October

Gokeri G, Kocar C and Tombakoglu M 2009 'Modeling and Simulation of Microbeam Radiation Therapy' presented at X. National Nuclear Sciences and Technologies Congress, Mugla, 6 – 9 October

Area of Interest: Monte Carlo Applications, Microbeam Radiation Therapy, Radiation Protection, Atmospheric Dispersion, Emergency Preparedness and Response, Burnup Dependent Neutronic Calculations

References:

Prof. Dr. Mehmet Tombakoğlu, Hacettepe University, Dept. of Nuclear Engineering

Assoc. Prof. Cemil Kocar, Hacettepe University, Department of Nuclear Engineering

Prof. Okan Zabunoğlu, Hacettepe University, Department of Nuclear Engineering

